PEOPLE'S DEMOCRATIC REPUBLIC OF ALGERIA

MINISTRY OF HIGHER EDUCATION AND SCIENTIFIC RESEARCH

UNIVERSITY OF BLIDA 1

Faculty of Technology

Department of Process Engineering

LMD DOCTORAL THESIS

in Process Engineering

Specialty: Materials Technology

PREPARATION OF ACTIVATED CHARCOAL DERIVED FROM LUFFA AND ITS APPLICATION IN THE DEGRADATION OF ORGANIC POLLUTANTS BY PHOTOCATALYSIS

By

Miss. Souad BOUMAD

JURY MEMBERS

R. ISSADDI	Profesor, U. Blida 1	President
B. CHEKNANE	Profesor, U. Blida 1	Examiner
A. KHELIFA	Profesor, U. Blida 1	Examiner
O. CHERIFI	Profesor, USTHB	Examiner
N. BOUCHENAFA-SAIB	Profesor, U. Blida 1	Supervisor
Mª.A. LILLO-RÓDENAS	Profesor, U. Alicante	Co-Supervisor

Blida, December 2021

ملخص

الهدف من الأطروحة الحالية هو تثمين كتلة حيوية لينوسيلولوزيكية تدعى اللوف الأسطواني، وهي عبارة عن نبات وفير في الجزائر، من أجل تطوير مواد عالية المسامية للتطبيق المحتمل في تحلل الملوثات العضوية في المحاليل المائية.

تم تحضير العديد من عينات الكربون المنشط المشتق من اللوف عن طريق التنشيط الكيميائي مع حمض الفوسفوريك بنسبة 85٪ متبوعًا بالمعالجة الحرارية في الفرن الأنبوبي والغسيل. تمت دراسة متغيرات كثيرة مثل النسبة الكتلية للتنشيط حمض/كتلة اللوف (1، 3، و5)، درجة حرارة التنشيط (500، 550، و700 درجة مئوية)، وزمن التنشيط (1 و2 ساعات) لتحسين ظروف التحضير. عدة تقنيات استعملت لتحديد الخصائص الفيزيوكيميائية للفحوم الناتجة. تم تحليل البنية عن طريق المسح المجهري الالكتروني، فيما تم فحص النسيج المسامي بواسطة امتصاص غاز الازوت وثنائي أكسيد الكربون (عند -196 و0 درجة مئوية على التوالي).

أظهرت النتائج المتحصل عليها ان خصائص الكربونات المنشطة تعتمد وتتأثر بشكل كبير على ظروف وشروط التحضير. أعلى قيمة للمساحة السطحية الخاصة التي تم الحصول عليها تصل لحدود ال 1300 م2/غ عند نسبة 3/1 ودرجة تنشيط 550 درجة مئوية، لمدة ساعتين من التنشيط. أظهرت صور المسح المجهري الالكتروني تكون هياكل كربونية نشطة ذات خصائص مسامية معتبرة إثر تحلل السليلوز واللجنين بواسطة حمض الفوسفوريك.

اختير الكربون المنشط الذي أظهر أحسن الخصائص في ظل ظروف تحضير معتدلة كداعم لجزيئات ثاني أكسيد التيتان لتحضير مواد مركبة محفزة من اجل استغلالها في عملية التحليل الضوئي للأصباغ العضوية الصعبة الازالة بالتقنيات التقليدية. تم استخدام الخلط الميكانيكي للكربون المنشط المشتق من اللوف مع جزيئات التيتان وطريقة السول جال لتحضير مركبات ذات نسب مختلفة للتيتان. أظهرتحليل حيود الأشعة السينية وجود الطبقة النشطة أناتاز، بينما كشف المطياف الضوئي للأشعة السينية عن وجود المجموعات الوظيفية على سطح المواد المركبة. من ناحية أخرى، أثبت الإنعكاسالمنتشرللاشعة فوق البنفسجية انخفاضا في طاقة الفجوة الممنوعة الخاصة بهم. أظهرت المواد أيضا، بسبب دمج الكربون المنشط، تطورا مهما في مساماتها السطحية مقارنة بالتيتان النقي.

كمرحلة أخيرة، تم اختبار المواد المركبة في التحلل الضوئي لصبغين عضويين. التحلل الضوئي لصبغة ازرق الميثيلين تم تحقيقها باستعمال الاشعة فوق البنفسجية، اما فيما يخص اخضر الملاكيت فقد تم التحلل تحت اشعاع الشمس المحاكي. تم إيلاء اهتمام خاص لمساهمة ظاهرة الامتزاز في عملية التحلل كونها خاصية رئيسية يمتاز بها الداعم، بالإضافة الى دراسة الالية المحتملة لكيفية التحلل. لجميع تجارب التحلل الضوئي التي تمت دراستها، أظهرت العينات أداءً جيدا مما أدى، بالنسبة لأغلب العينات، الى القضاء التام على الصبغة بعد 30 دقيقة من التعرض لمصدرالاشعة مقارنة بأكسيد التيتان النقي. تحلل صبغة أخضرالملاكيت تحت تأثير الاشعاع الشمسي دال على ان المواد المركبة الناتجة نشطة في المنطقة المرئية من الطيف الضوئي.

الكلمات المفتاحية: اللوف الاسطواني، التنشيط الكيميائي، الكربون المنشط، أكسيد التيتان، الملوثات العضوية، التحلل الضوئي.

ABSTRACT

The objective of this current Ph-D thesis is based on the valorization of the lignocellulosic biomass luffa cylindrica, which is an abundant residue in Algeria, for the elaboration of highly porous materials for possible application in the degradation of organic pollutants in aqueous solutions.

Several Luffa-derived activated carbons (LACs) have been prepared by chemical impregnation with an 85% phosphoric acid solution (H_3PO_4) under reflux, followed by thermal treatment in a tubular furnace and washing. Different parameters such as H_3PO_4/Luffa mass impregnation ratio (1, 3, and 5 wt/wt. %), activation temperature (500, 550, and 700°C), and time (1 and 2 h) were studied to investigate the effect of the preparation conditions on the textural properties of the prepared activated carbons. Different techniques were applied to explore the physico-chemical properties of LACs as ultimate and proximate analyses. The morphology was analyzed by scanning electron microscopy, and porous texture was investigated by N_2 and CO_2 gas adsorption (at -196 °C and 0 °C, respectively).

The results have shown that the properties of the activated carbons derived from luffa are highly dependent on the preparation conditions. The highest surface areas, reaching 1300 m^2/g, were obtained with an impregnation ratio of 3/1 at 550°C treatment temperature maintained for 2 hours. SEM images have revealed the development of the porous structure of the activated carbon due to the decomposition of cellulose and lignin led by phosphoric acid.

The activated carbon showing better properties was chosen as support of titania particles for the photodegradation of organic dyes. Mechanical mixing of luffa activated carbon and TiO_2 particles, and sol-gel synthesis were used to prepare TiO_2/LAC composites with different titania loadings. The XRD analysis showed the presence of the active anatase crystalline phase, while XPS characterization revealed the presence of oxygenated functional groups on the surface of the composites. On the other hand, UV diffuse reflectance confirmed a decrease in their bandgap. The hybrids also showed an importante development in the surface area compared to bare titania related to the incorporation of the LAC.

As a final step, the composites were tested in the removal of two organic dyes. The photodegradation of methylene blue was conducted under UV irradiations, while that of malachite green under simulated solar light irradiations. Special attention was paid to the contribution of the adsorption phenomenon on the behavior of the composites since it is the main characteristic of the support material, in addition to the study of the possible photodegradation pathway. For all studied photodegradation experiments, the samples showed a good performance, leading, for most composites, to the total dye removal after 30 min of exposure to the irradiation source compared to bare titania. Photodegradation of malachite green under solar irradiation showed that the TiO_2/LAC composites could be photoactive in the visible light region.

Keyword : *Luffa cylindrica*, chemical activation, activated carbon, TiO_2, organic pollutants,photocatalysis.

RESUME

L'objectif de cette présente thèse est basé sur la valorisation de la biomasse lignocellulosique : *luffa cylindrica*, qui est un résidu abondant en Algérie, pour l'élaboration de matériaux très poreux pour une éventuelle application dans la dégradation de polluants organiques en solutions aqueuses par photocatalyse. Plusieurs charbons actifs dérivés du Luffa (LACs) ont été préparés par imprégnation chimique avec une solution d'acide phosphorique à 85 % (H_3PO_4) à reflux, suivie d'un traitement thermique dans un four tubulaire et d'un lavage. Différents paramètres tels que le rapport massique d'imprégnation H_3PO_4/Luffa (1, 3 et 5 g/g), la température d'activation (500, 550 et 700°C) et le temps de séjour (1 et 2 h) ont été étudiés pour optimiser les conditions de préparation. Les propriétés physico-chimiques des charbons actifs préparés ont été déterminé par différents techniques comme l'analyse thermogravimétrique et CHNO. La morphologie a été analysée par microscopie électronique à balayage, et la texture poreuse a été étudiée par adsorption de gaz N_2 et CO_2 (à -196 °C et 0 °C, respectivement).

Les résultats ont montré que les propriétés des charbons actifs issus de la *Luffa cylindrica* dépendent fortement des conditions de préparation. Les surfaces spécifiques les plus élevées, atteignant 1300 m^2/g, ont été obtenues avec un taux d'imprégnation de 3/1 à une température de traitement de 550°C maintenue pendant 2 heures. Les images SEM ont montré le développement de la structure poreuses des charbon actifs à cause de la décomposition de la cellulose et de la lignine sous l'effet de l'acide phosphorique.

Le charbon actif présentant les meilleures propriétés et préparé par des conditions modérées a été choisi comme support de particules d'oxyde de titane pour la photodégradation des colorants organiques. Le mélange mécanique du charbon actif de *Luffa* avec les particules de TiO_2 et la synthèse sol-gel ont été utilisés pour préparer des composites TiO_2/LAC avec différentes charges de dioxyde de titane. L'analyse de diffraction des rayon-X a montré la présence de la phase cristalline active anatase, tandis que la caractérisation XPS a révélé la présence de groupes fonctionnels oxygéné à la surface des composites. D'autre part, la diminution de l'énergie de leur bande interdite a été confirmée par la réflectance UV. Les composites ont également montré un développement important de la surface spécifique par rapport à l'oxyde de titane sous l'effet de l'incorporation du LAC.

Finalement, les composites ont été testés dans l'élimination de deux colorants organiques. La photodégradation de bleu de méthylène a été réalisée sous irradiations UV et celle du vert malachite sous irradiations solaires simulées. Une attention particulière a été portée à la contribution du phénomène d'adsorption sur le comportement des composites étant la caractéristique principale du matériau support, en plus de l'étude du mécanisme probablement impliqué. Pour toutes les expériences de photodégradation étudiées, les échantillons ont montré une bonne performance, conduisant, pour la plupart des composites, à l'élimination totale du colorant après 30 min d'exposition à la source d'irradiation par rapport à l'oxyde de titane pure. La photodégradation du vert malachite sous les irradiations solaires a montré que les composites élaborés sont actifs dans la région visible du spectre lumineux.

Mots-clés : *Luffa cylindrica*, activation chimique, charbon actif, TiO_2, polluants organiques,photocatalyse.

ACKNOWLEDGMENTS

First and foremost, praises and thanks to God, the Almighty, for His showers of blessings throughout to complete my research work successfully.

Foremost, I would like to address my sincere gratitude to my advisor and mentor Prof. ***Naima BOUCHENAFA-SAIB*** for enlightening me the first glance of research, allowing me to discover how fascinating scientific research is, and providing invaluable guidance. Her continuous support, motivation, presence when most needed, and enthusiasm have deeply inspired me. I am extremely grateful for her encouragement in my moments of doubt, the trust she placed in me allowed me to fruitfully carry out this work. My appreciation is expressed to her for sharing her scientific skills, methodology, and immense knowledge to form a better version of me. Words can't even be enough to express my gratitude toward her at any level. I'm really blessed to have such an advisor that I could never have better than her.

También quiero darles los agradecimientos a mis co-directoras de tesis, profesora ***María Ángeles Lillo Ródenas*** y profesora ***María del Carmen Román Martínez*** de la universidad de Alicante. En primer lugar, gracias por aceptarme bajo vuestra supervisión durante todos los años de investigación. Fue un gran privilegio y un honor trabajar con mujeres tan trabajadoras como vosotras. Cualquier intento en cualquier nivel no se puede completar sin su apoyo. Gracias por vuestra dedicación, consejos, orientación, y por enseñarme la metodología para realizar la investigación y presentar los trabajos de investigación con la mayor calidad y claridad posible.

Mis sinceros agradecimientos se van al profesor ***Diego Cazorla Amorós*** de la universidad de Alicante por aceptarme en sus laboratorios del grupo MCMA, y hacerme sentir una de los miembros de su equipo.

Igualmente, me gustaría agradecer especialmente al profesor ***Enrique Rodríguez Castillón*** y la doctora ***Antonia Infantes Molina*** de la universidad de Málaga por haberme recibido en su grupo NMI bajo su supervisión dentro de la beca del programa learn África. Gracias por vuestra colaboración, apoyo, observaciones y contribuciones que dieron más valor a mi trabajo. Agradezco mucho todas las oportunidades que me habéis dado y que fueron muy valiosas para potenciar mis conocimientos y desarrollar nuevas habilidades.

Me gustaría dedicarle también unas palabras a la profesora ***Elisa Moretti*** de la universidad de Venecia, Italia por dedicar su precioso tiempo en hacerme los experimentos en su laboratorio y su valiosa *ayuda*.

My sincere gratitude to prof. ***R. Issaddi*** for honoring the presidency of the jury. My respectful acknowledgments are also extended to professors ***B. Cheknane, A. Khelifa,*** and ***O. Cherifi*** for honorably accepting to examine this work.

Special thanks go to Mrs. ***Maria Tereza de la Vega*** and la Fundación Mujeres por Africa for the scholarship offer within the Learn Africa program for the year 2019. And the **ministry MESRS** of Algeria for the PNE scholarship.

I would like to express my special gratitude to professors **M.*Derbel*** and ***A.Aouabed*** for opening the doors of their laboratories for me when I needed it the most, and professor **F.Zermane** for her help, support, encouragement, and XRD analysis. My gratitude is also granted to professor **Y. *Bouchefa*** from USTHB, Doctor ***S. Tazibat*** from EMP laboratories, and professor **M.A. *Benamar*** from the USDB 1 for their valuable help.

Tuve la suerte de coincidir con unas doctoras maravillosas durante mis estancias en la universidad de Alicante, ***Laura Cano Casanova*** y ***Ana Amorós Pérez***. Por lo que es muy importante darles las gracias, por vuestra ayuda, presencia en cada momento de necesidad, por aguantar mis molestias (Laurita, te rompí el reactor), vuestra amistad y cariño y, sobre todo, para considerarme una de vosotros y regalarme tantos momentos de alegría.

Me siento muy agradecida a ***Isabel Barroso Martín***, doctoranda en la universidad de Málaga por su ayuda durante mi estancia allí, su atención, presencia y explicaciones. Me siento muy afortunada de poder conocerte, trabajar y aprender de un profesional y compañera tan trabajadora.

Por supuesto, además quisiera agradecer a todos los miembros de los grupos de investigación *MCMA* de Alicante y NMI de Málaga por su hospitalidad y amabilidad, y a todos aquellos que hicieron de mis estancias una experiencia inolvidable en especial los **"GUACHITOS"**.

A part of my acknowledgments goes to the group of technicians of the **GP** department of USDB1 for their help and technical contribution.

To my dearest friends *Dr.* ***I.Moulefera***, and ***M.Mahmoudi***, my deepest gratitude for the countless times you have been there, and for the keen interest shown to complete this thesis successfully. Thanks to ***Miss Z. Mahieddine*** *for* your time, efforts, and facilitating the paperwork of the scholarship for me. All my friends and colleagues and everyone who contributed in his own way in achieving this work.

Last, but not least, I am extremely grateful to ***my parents*** for their love, prayers, caring, and sacrifices for educating me, believing in me, and supporting me throughout this important journey. With a special thanks to my sisters, brothers, and brothers-in-law for always being there for me.

Thanks, Merci, Gracias, شكراً

To the memory of

my BELOVED FATHER…

Although late..... but....Your dream finally came true

INDEX

LIST OF ILLUSTRATIONS

CHAPTER I

CHAPTER II

CHAPTER III

LIST OF TABLES

CHAPTER II

CHAPTER III

NOMENCLATURE

a_m	: Molecular area of the adsorbate for Nitrogen 0.162 nm^2
$A_{anatse(101)}$	: Areas of the peaks anatase (101)
$A_{rutile(110)}$	: Areas of the peak's rutile (110)
$A_{CaF2(220)}$	: Areas of the 100% peak of CaF_2(220)
B	: Average crystallite size
BE	: Banding energy (eV)
BET	: Brunauer, Emmett, and Teller
BQ	: Benzoquinone
C	: Constant depending on the net molar energy of adsorption.
Ce	: Equilibrium concentration (mg/L)
C_t/C_0	: Relative concentration
C_i	: Initial concentration (mg/L)
C_t	: Concentration at time t (mg/L)
CB	: Conduction band
d_{hkl}	: Indicates the distance between the atomic layers
DR	: Dubinin-Radushkevich
DSC	: Differential scanning calorimetry
DRUV-vis	: Diffuse Reflectance Ultraviolet-visible
E_0	: Characteristic adsorption energy
E_B	: Bond electron
E_k	: kinetic energy
EM	: Electron Microscope
Eg	: Bandgap energy
FTIR	: Fourier transform infrared spectroscopy
hν	: Photon energy
HHV	: High heating value
K	: Scherrer constant (K = 0.93)
k	: Pseudo-first-order rate constant (min^{-1})
LACs	: Luffa activated carbons
LC	: Luffa cylindrica
LT	: Low temperature
MB	: Methylene blue
MeOH	: Methanol
MG	: Malachite green

MM : Mechanical mixing method

MT : Moderate temperature

N : Number of moles adsorbed

n : Integer or as called the order of reflection

n_m : Monolayer capacity in moles

N_A : Avogadro's number ($6.022\ 10^{23}\ mol^{-1}$).

P/P_0 : Relative pressure

PSD : Pore size distribution

R : Impregnation ratio (weight of H_3PO_4/weight of precursor)

R% : The percentage

S_{BET} : Specific surface area calculated by the BET method (m^2/g)

SG : Acetic acid

SS : Sol-gel synthesis

OM : Optical Microscope

SEM : Scanning electron microscopy

SEM-EDX : Scanning electron microscopy with energy-dispersive X-ray

t : Time (min)

T : Temperature (°C, K)

TGA : Thermogravimetric analysis

TOA : Advanced oxidation techniques

TP : TiO_2 P25 from Degussa

TPD : Temperature-programmed desorption

TTIP : Titanium tertaisopropoxide

TSG : TiO_2 prepared by sol-gel using acetic acid

V : Volume of solution (L)

$V_{DR}\,N_2$: Adsorbed volume under Nitrogen flow (cm^3/g)

$V_{DR}CO_2$: Narrow micropore volume obtained by DR method (cm^3/g)

V_t : Micropore volume obtained by t method (cm^3/g)

V_{meso} : Mesopore volume (cm^3/g)

W : The adsorbed volume

W_0 : The adsorbed volume

XPS : X-ray photoelectron spectroscopy

2D-NLDFT : Non-local density functional theory

α : The absorption coefficient

β : The full width at half maximum intensity

θ : The angle of maximum peak

λ’ : Specifies the wavelength of the incident X-ray beam

λ : Radiation wavelength

INTRODUCTION

INTRODUCTION

Nowadays, the environment and energy are knowing growing serious issues of degradation and exhaustion related to rapid economic evolution. Subsequently, humanity is experiencing the utmost extensive energy shortages and environmental pollution in history. To surmount so, it is imperative to raise awareness of the huge influence to adapt technologies, products, and materials that are environmentally benign and sustainable.

Although purification water technologies strongly progressed, they always run up against certain molecules hardly removed such as organic dyes which are used in great quantities in the textile industry throughout the world [1]. The textile wastes are dangerously threatening the quality of water and the environment in general. Organic dyes are used mainly in the textile industry, in the paper dyeing process, as a food coloring agent, as a medical disinfectant, and in the aquaculture industries as a fungicide [2–5]. They are environmentally recalcitrant and extremely toxic to a variety of aquatic and terrestrial mammals. They cause crucial health problems, as many of them proved to be multi-organ toxins and carcinogenic for humans [6,7]. The effect of these pollutants on ecological health requires the development of more effective processes able to remove recalcitrant pollutants from wastewater by different methods. Thus it has been an important challenge for recent society and the subject of several studies over the last few years [8–10].

In recent years, the socio-political encouraged the reduction of the consumption of non-renewable resources to a better contribution to the preservation of the environment. Therefore, growing attention is attributed to plant biomass as a raw material for chemistry [11,12]. Companies are following this trend and see a major economic interest in developing products and biosourced materials from renewable materials such as biomass. As a result, the development of biomass in porous materials as activated carbons is of great interest and is the subject of numerous studies. This strategy makes it possible to take advantage of the exceptional agriculture potential.

Activated carbon (AC) notices an increasing use in various applications worldwide. It plays a major role in the processes of a clean environment, involving water purification with adsorption [1], supported catalysis and photocatalysis [2,3] methods of chemical separation [4], gases [5], and associated industries, etc. The growing interest led to the

search for new, more efficient, economical, and with large availability sources of precursors for the production of high-quality porous material, not only to minimize its cost of production but also to decrease the environmental effect of agricultural and industrial wastes and reduce their cost of disposal and as a result, provide a potentially inexpensive alternative to the current commercial activated carbons. The chosen precursors have an important influence on the textural characterizations of the resulting activated carbons as the main factor to control developed porosity, surface area, and surface chemistry. Many plants and wastes [6-8], agricultural by-products such as wood [9], sewage sludge [10], olive and dates stones [11],…etc. have been investigated so far for the synthesis of ACs; whereas lignocellulosic materials gain most interest been rich in woody cell walls consisting of cellulose and lignin.

Lignocellulosic biomass is generally composed of three biopolymers: cellulose, hemicellulose, and lignin with different fractions depending on the type of the biomass [12]. Generally, cellulose represents the major fraction of the plant composition been responsible for forming the plant's primary cells wall structure. It is a polysaccharide made up of glucose subunits that provides rigidity and mechanical support for the cell wall maintaining the shape and the direction of cell growth. whereas lignin is a highly non-regular organic polymer of phenol sub-units responsible for cell wall thickenings of cells in the secondary wall of the vascular tissue [13].

Among a lot, *Luffa cylindrica* (LC) is one of the most abundant plants widely used in different fields. It is an annual plant, growing mostly in tropical and subtropical countries, commonly used as a bath-sponge. *Luffa cylindrica* consists mainly of Cellulose (60%), hemicellulose (30%), and lignin (10%). The high content in cellulose promotes it to be a good precursor for the preparation of activated carbon [13]. Although the massive papers dealing with the valorization of different lignocellulosic materials, only a few focused on studying luffa cylindrica fibers as an alternative precursor.

The adsorption technique is one of the most classical methods used for the removal of organic and inorganic impurities from domestic and industrial wastewater [14]. It is effective, fast, its design is simple, its operating cost is low and it avoids the production of harmful by-products [15]. Different materials from different sources have extensively been used as versatile adsorbents for their well-developed porous structure and surface area [16]. Despite the outstanding properties, once the adsorbate is saturated, an additional

regeneration step is needed for further use in addition to the fact that the pollutant is not totally eliminated [17]. To overcome so, attempts for the combination of adsorption with advanced photocatalytic oxidation processes are interesting, also trying to lead to highly efficient removal of the contaminants [18].

Heterogeneous photocatalysis is considered one of the most promising processes for wastewater treatment, given its potential for complete mineralization of pollutants to non-toxic products upon irradiating a suspension of a semiconductor in the presence of an electron donor and acceptor substrates through interfacial electron exchange [19–22]. Many photocatalysts, such as ZnO, CuO, Ga_2O_3, have succeeded to be suitable for this application, being titanium dioxide the preferred one for several reasons: high chemical stability, low cost, it is environmentally friendly and it is suitable for the oxidation of organic compounds, including the inactivation of microorganisms being, besides, a chemically and biologically compatible material [23–25]. However, there are also some drawbacks to TiO_2. In addition to a high rate of e^-/h^+ pairs recombination, its hard sedimentation and difficult separation, given its small particle size, should be highlighted [26,27].

Enhancing the photo-efficiency of TiO_2 is, for all these reasons, indeed interesting, keeping in mind the benefits of combining TiO_2 photocatalysis with adsorption and the possibility of ion doping or coating TiO_2 with different metals and adsorbents. From them, zeolites and silica have been widely studied [28,29], but especially activated carbon has gained many researchers' attention as a matrix to support TiO_2 particles. The addition of activated carbon ensures good dispersion of TiO_2 particles on its developed surface and, consequently, avoids TiO_2 agglomeration [30,31]. Furthermore, organic pollutants can easily be adsorbed on the activated carbon surface thanks to its effective physical and chemical adsorption ability, thus increasing pollutants concentration on the surface [32].

This present Ph-D work has two objectives, the first one is the valorization of biomass luffa cylindrica, which is abundant in Algeria for the production of highly porous activated carbon material. and the second one is to test its effectiveness in photocatalysis as support of titanium oxides in the degradation of organic pollutants in aqueous solutions. The targeted pollutants are organic dyes that are hard to eliminate from the environment issued mostly from the textiles industry.

This Ph-D thesis is divided into three main chapters. CHAPTER 1 is a bibliographic review that regroups relevant information about (i) activated carbons, their origin, and their different preparation methods, paying special attention to their chemical preparation with phosphoric acid, and the different types of precursors used for that, (ii) an overview about the lignocellulosic material *Luffa Cylindrica* and its properties that promote it to be used as a precursor for activated carbons, (iii) definition of the main notions of photocatalysis process (principle, semiconductors, irradiations…) and its mechanism for the mineralization of recalcitrant organic pollutants.

CHAPTER 2 details the general experimental set-ups and methodology employed in this thesis research. This chapter analyzes the preparation method of the studied materials (activated carbons and photocatalysts), and their characterization. In addition, it highlights the different equipment and systems used for the photodegradation experiments.

Last, CHAPTER 3, divided into two parts, explores in-depth (i) the physico-chemical characterization results of the prepared activated carbons, (ii) the results of photodegradation tests of the organic dyes, methylene blue and malachite green, under UV and solar irradiations. All the experimental results are roughly analyzed, discussed, and commented on. The efficiency of the Luffa cylindrica and the prospects for its future use as a precursor for water treatment applications is considered as a conclusion.

CHAPTER I

1 CHAPTER I: STATE OF THE ART

1.1 Activated carbon

The presence of carbon or charcoal in human history extends so far back in time that its origin is impossible to be accurately determined. Carbon is considered the furthermost important element in the world among all the elements with a vital role since it is used widely in living tissues [33]. Activated carbon, also called activated coal or activated charcoal, is non-graphitic, non-graphitizable carbon with isotropic structure and a highly disordered microstructure, so that was described as wrinkled paper sheets [34]. It is a form of carbon processed to be sieved to a material with a well-developed pore network and a large internal surface area. It generally ranges from 500 to 2000 m^2/g and is considered as its utmost distinctive characteristic of high adsorption capacity. The precursor is then converted or 'activated' using medium to high-temperature carbonization treatments, which eliminate the solid mass to create the porosity where the removed mass was previously located [14,35].

Almost any carbonaceous solid with high carbon content and low inorganic content can be transformed into activated carbons. Thus various natural and synthetic raw materials can be widely used as precursors such as wood, coconut shells, residues and by-products petroleum coke, date, and olive stones, lignin, sawdust, and many other sources [36–38]. Activated carbons can also be found in three different physical forms, powdered, granular, and extruded (Figure 1.1)

Figure 1.1. Different forms of activated carbons

1.1.1 Physical and chemical characterization

1.1.1.1 Physical properties

- Structure

The structure of the skeleton carbon (Figure 1.2) can be considered as a mixture of graphite-like crystallites (of few parallel plane layers of graphite) and a non-organized phase composed of complex aromatic-aliphatic forms [39]. The crystallites are randomly oriented and extensively interconnected. During the activation process, the regular array of carbon bonds on the surface of these crystallites is disrupted, resulting in relative free valences and anisotropic alignment [40].

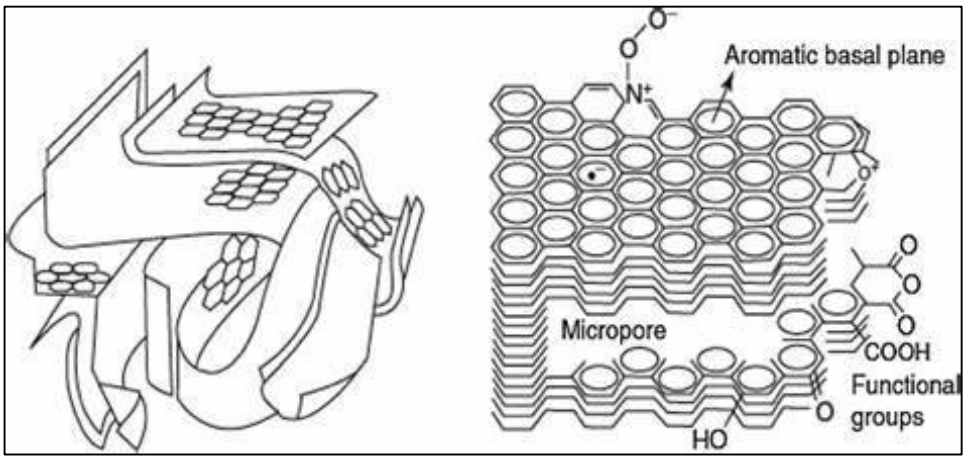

Figure 1.2. Structure of activated carbon [41]

In the light of the above considerations, the structure of an activated carbon could be visualized as a stack of poorly developed aromatic sheets. These lasts are distributed and crosslinked randomly, separated by disorganized carbonaceous and inorganic matter derived from the precursor associated with the presence of cavities [34].

- Porosity and surface area

Porosity is the main physical property that characterizes activated carbons. During the activation process, some of the carbon is removed from the crystallites and, contemporary, the spaces between them become vacant of less organized carbonaceous matter [42]. The channels that result through the graphitic areas, and the breaches amid the

crystallites of the activated carbon, all with the fissures inside and parallel to the graphitic planes, make up the porous network which generally has a large surface area [34].

The porous structure is formed by pores of different sizes (Figure 1.3) that can be classified into the following three major groups according to the International Union of Pure and Applied Chemistry (IUPAC) [43].

- Macropores with pore diameter > 50 nm;
- Mesopores with pore diameter between 2 nm< ϕ < 50 nm;
- Micropores with pore diameter <2 nm.

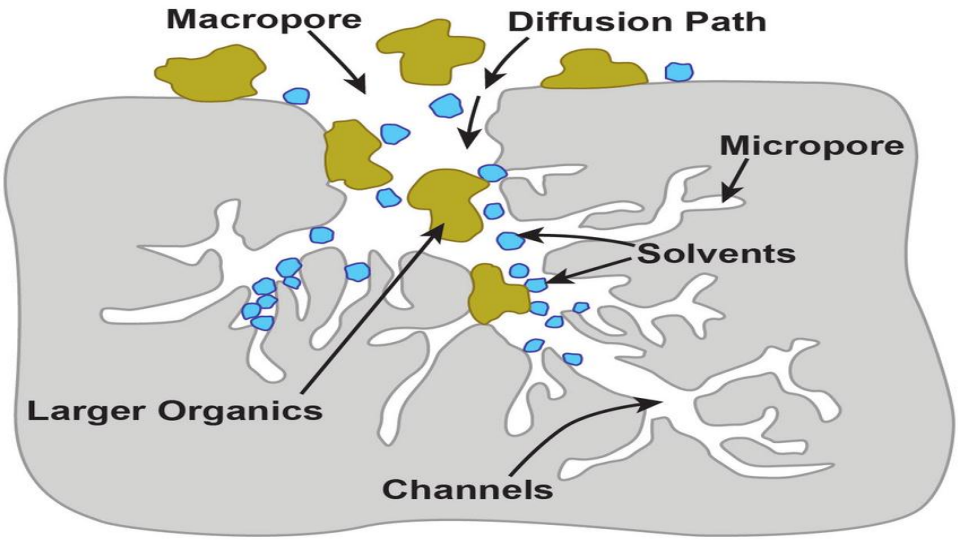

Figure 1.3. Schematic of an activated carbon particle revealing pore structure adapted from by IUPAC [44].

This porous structure is also characterized by the presence of small amounts of different heteroatoms such as oxygen and hydrogen and, in some cases, variable amounts of mineral matter (ash content) depending on the source material and activation conditions. In addition, it strongly affects, in terms of the spatial arrangement of carbon atoms, both, the bulk and the surface properties of the obtained activated carbon [34].

The relatively large specific surface area is another important property that characterizes activated carbon. It consists mainly of basal planes and the edges of the planes that form the edges of microcrystallites [45]. The specific surface area is calculated by applying the Brunauer-Emmett-Teller (BET) equation to the isotherms obtained during the adsorption process [46]. It is based upon the assumption that the monolayer is located on surface sites of uniform adsorption energy and multilayer build-up via a parallel process

to the condensation of the adsorbate. The quite high values of the activated carbons surface areas are mostly due to the contribution of the micropores in the adsorption process [47]. Nevertheless, meso- and macropores play, as well, a very important role since they serve as the channel through which the adsorbate reaches the micropores. However, the slit-shaped micropores formed by the spaces between the carbon layer planes are not accessible to molecules of a spherical geometry, which have a diameter larger than the pore width. This means that the specific surface area of carbon is not necessarily proportional to the adsorption capacity of the activated carbon. So, pore size distribution, therefore, is a factor that cannot be ignored [48].

1.1.1.2 Chemical properties

In addition to the physical properties of activated carbons, the chemical ones are very attractive to be considered. In particular applications, textural properties are not sufficient for better performance, therefore, understanding the surface chemistry regarding the nature and amount of surface functional groups present on the carbon surfaces must also be taken into account [49]. On the edges of the basal planes of activated carbon, the unsaturated carbon atoms possess unpaired electrons. These sites are usually bonded to heteroatoms giving rise to surface groups (Figure 1.4) [50].

Among these groups, nitrogen, phosphorus, and oxygen-containing surface groups are by far the most common [51,52].The most significant influence comes from edge-bonded oxygen formed through the chemical reaction of atoms formed by the dissociation of molecular oxygen with atoms of carbon [53]. Some of these surface oxygen-containing groups of activated carbons present an acid character such as lactonic, anhydride, and carboxylic groups, while others such as carbonyl, quinone, phenol, and, ether groups show a basic character [54–56]. The surface functional groups of the activated carbon determine the self-organization, chemical stability, and reactivity in adsorptive and catalytic processes, consequently, the surface chemistry can be easily modified through thermal and chemical treatments depending on the desired properties of the final activated carbon [57–59].

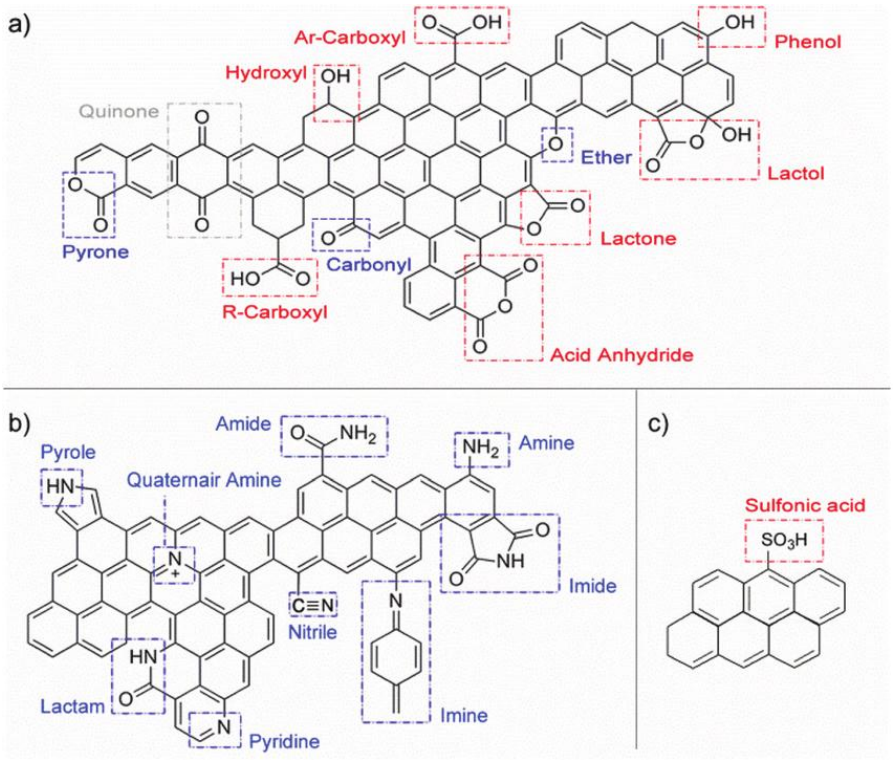

Figure 1.4. Acidic (red) and basic (blue) surface functionalities on a carbon basal plane (a) oxygen, (b) nitrogen, and (c) Sulphur[60].

1.1.2 Preparation methods of activated carbon

Generally, two substantial methods are adopted in the preparation of activated carbon from solid carbonaceous-based material. The Activation process can be divided into two well-known categories: physical and chemical activation. The use of these methods depends on the final desired features of the activated carbons and activating agent used.

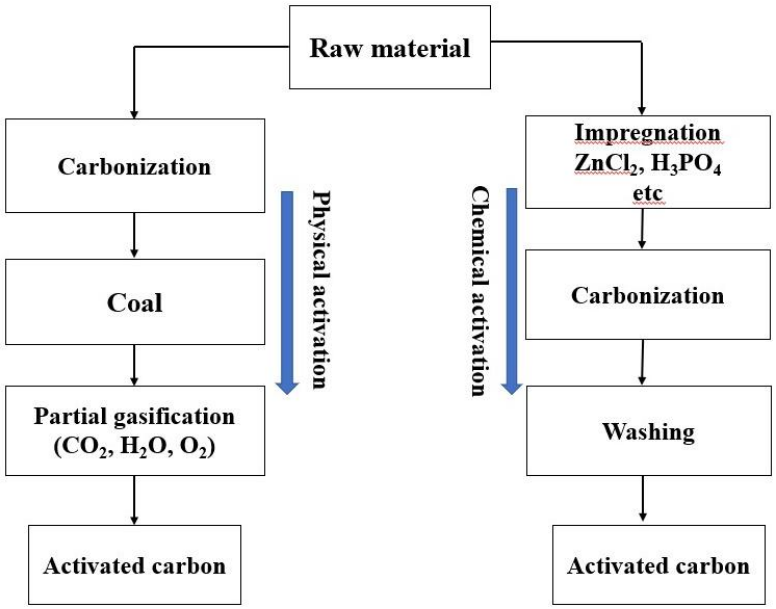

Figure 1.5. Schematic of the preparation steps of activated carbon by chemical and physical activation method.

1.1.2.1 Physical activation

Physical activation is considered as a two steps process. It is started with the carbonization of the carbonaceous raw material at medium or high temperatures, (generally, between 400 and 850ºC, and sometimes reaches 1000ºC) in a controlled inert atmosphere, where devolatilization/thermal degradation of non-carbon species leads to an enrichment of carbon[61,62]. This step is usually critical in the overall production of activated carbons since during this step, the porosity starts to form. The carbonization temperature has the most significant effect, followed by heating rate, nitrogen flow rate, and finally residence time [63]. The carbonization process is then followed by the activation process which is the key step for the development of the porous texture of activated carbon. It consists of partial and controlled gasification of the remaining char with an oxidizing agent such as steam, carbon dioxide, air, or their mixtures [64]. Unorganized carbon is removed during the first phase of the activation process. The lignocellulosic compound is then exposed to the action of activating agents leading to the development of a microporous structure [65]. In the succeeding phase of the reaction, walls between the pores are totally burnt-off resulting a widening in the formerly existing pores. During activation, the temperature is set between 800 and 1000 °C to develop the porosity and surface area of the carbon. Concerning the activating agent, steam is more effective

than CO_2 in terms of producing a relatively higher surface area since the smaller molecule size of water facilitates effective diffusion within the char's porous structure [62]. Steam activation is reported to be two or three times faster than CO_2 at the same degree of conversion [62,63]. The CO_2 is usually employed as an activation gas since it is clean, easy to handle and it enables control of the activation process due to the slow reaction rate at temperatures around 800ºC.

1.1.2.2 Chemical activation

In contrary to the physical activation, chemical activation is a single-step process as the carbonization of the precursor is in the presence of chemical agents acting as dehydrating reagents [66]. Therefore, It consists of the impregnation of the raw material with considerable amounts of a chemical agent and then submitted to a carbonization step [65]. Several chemicals are employed as activating agents like zinc chloride ($ZnCl_2$), sulfuric acid (H_2SO_4) potassium hydroxide (KOH), and potassium carbonate (K_2CO_3) or their mixtures. H_3PO_4 and alkaline hydroxide are the most commonly used compared to zinc chloride that whose use has declined due to problems of environmental contamination [36,67–69]. The products resulting from the thermal decomposition of the precursor react with the chemical agent incorporated to the interior of the precursor particle, reducing the evolution of volatile matter, inhibiting the shrinking of the particle and restricting the formation of tars. In this way, the conversion of the precursor to carbon is high, leading to the formation of a large amount of porosity [70]. At the end of the process, the product needs a washing step to eliminate any excess/residual chemical agent in the sculpture after carbonization for a further evacuation of the pores. These activating agents develop the porosity by dehydration and degradation reactions, and the thermal treatment temperature depends on which chemical agent is used. Generally, chemical activation takes place at a lower temperature than physical activation, ranging between 450 and 700 °C [66]. This improves the development of porosity in carbon structure due to the effect of chemical agents. One of the most important advantages of chemical activation over physical activation is the lower treatment temperature and shorter treatment time [69]. In addition to having a larger surface area and well controlled microporosity in smaller ranges, the carbon yield of chemical activation is effectively higher than that of physical activation [70].

- Phosphoric acid activation

Preparation of activated carbon using chemical activation with phosphoric acid has widely attracted researchers' interest considering its influence on the physico-chemical characterization of the prepared activated carbon [71–74]. Among many papers dealing with the preparation of highly porous activated carbons, Jogtoyen and Derbyshire (1998) extensively studied the reaction pathway versus temperature of activation with phosphoric acid from lignocellulosic materials [75]. It is stated that the hydrolytic conditions (acid concentration) strongly affect the degradation pattern of the biopolymers in the precursor [76]. The reaction of the lignocellulosic material with phosphoric acid starts once the components are in contact. Cellulose is found to be more resistant to acid hydrolysis, thus hemicellulose and lignin are attacked first. As a result, glycosidic linkages in polysaccharides (cellulose and hemicellulose) are hydrolyzed and aryl ether bonds in lignin are cleaved [77]. Further chemical changes and structural alteration, involving dehydration degradation, and condensation reactions, and redistribution of lignin and cellulose are subsequently promoted by phosphoric acid at low temperatures inducing the release of H_2O, CO, CO_2, and CH_4. At temperatures below 200 °C, phosphorus compounds can form ester linkages with -OH groups on cellulose, favoring the crosslinking of the polymer chains. As the temperature increases, cyclization and condensation reactions resulting an increase in aromaticity and size of the polyaromatic units through the scission of P-O-C bonds [78]. Upon carbonization at higher temperatures, above 300°C, the structural crosslinking reactions (phosphate linkages, such as phosphate and polyphosphate esters) take place, connecting and crosslinking biopolymer fragments and leading to an increase in carbon yield through retention of a relatively low molecular weight species in the solid phase. However, the activating agent is partly transformed into $H_4P_2O_7$ and continues to play its constructive role in activation progress [79]. The char is considered to be stable in the temperature range between 350 to 500 °C, however, at 430 °C and above, the size of the aromatic cluster grows extensively due to the continued cleavage of crosslinks and the structure endures significant expansion that conducts to a high surface area development. It is proposed that the acid serves to 'swell the material structure' enabling the cellulose microfibrils separation to form the pores [78]. Above 450°C, the phosphate linkage becomes thermally unstable leading to a secondary contraction and structural rearrangement that allows the growth and alignment of polyaromatic clusters that

afterward provokes a loss of the accessible porosity [75]. Figure 1.6 illustrates the formation of phosphate esters during cellulose reaction with phosphoric acid. It is then concluded that porosity development is directly related to the retention and dilation of cellular material [77].

T<450°C: Formation of phosphate on cellulose side chains and crosslinking

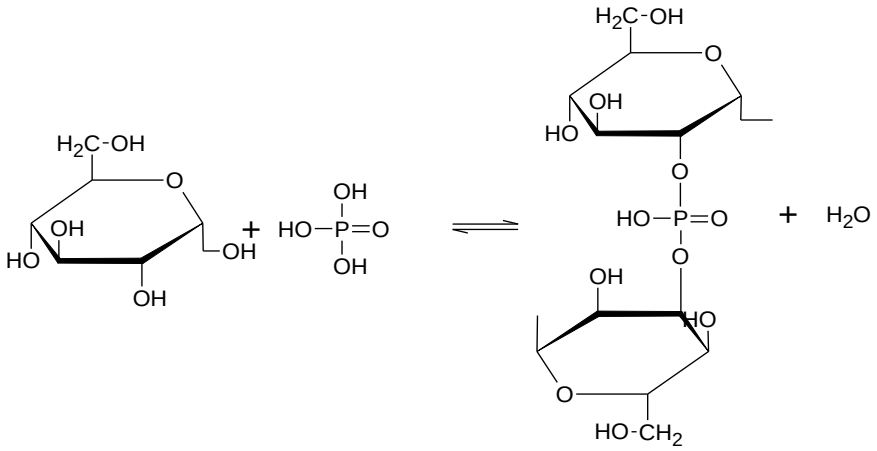

Esters can be derivatives of ortho-pyro-and meta-phosphoric acids

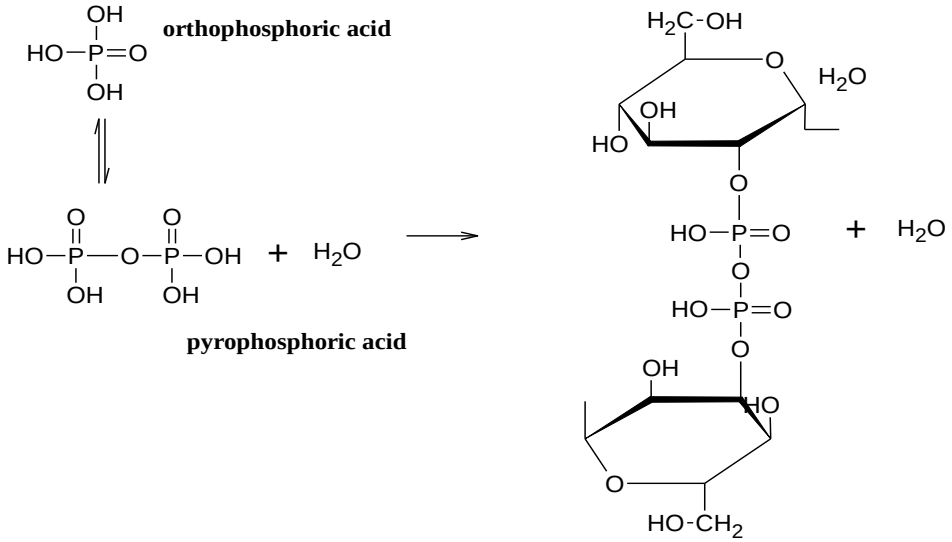

T>450 °C: Elimination of H_3PO_4

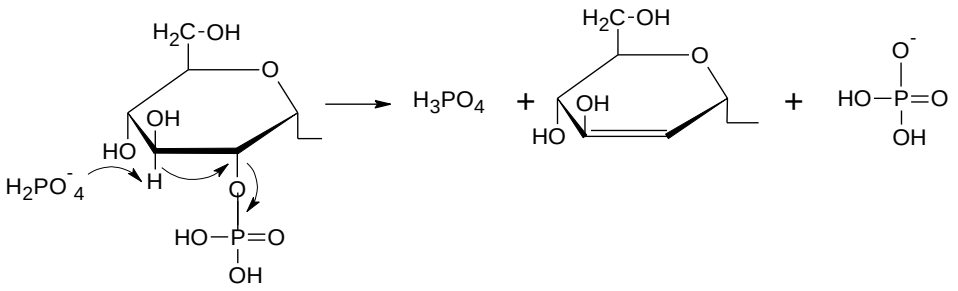

Figure 1.6. Mechanism of phosphate ester formation by phosphorylation of cellulose [75]

When concentrated H_3PO_4 is mixed with the precursor at high temperature, it seems to behave as (i) an acid catalyst to promote bond cleavage reactions and the formation of crosslinks via processes such as cyclization, and condensation, and (ii) to combine with organic species to form phosphate and polyphosphate bridges that connect and crosslink biopolymer fragments [46,80].

Furthermore, Benaddi et al. (1998) suggested that dehydration of cellulose by phosphoric acid is similar to dehydration of alcohols and at higher temperatures, the phosphorous oxides act as Lewis acids and can form C–O–P bonds [81]**.** While others studies stated that other abundant P species as –C–P– bonds are introduced in carbons by phosphoric activation [82].

It is also reported that activation of amorphous polymers produces mainly micropores, while activation of crystalline cellulose produces a heterogeneous porosity [70,83]. Unlike amorphous polymers, a greater potential for structural expansion of crystalline cellulose is required due to its higher density and chemical structure. This allows for a more extensive degree of combination with phosphoric acid, and hence "bulking" of the cell walls [84]. Increasing the heat treatment temperature and/or the ratio of phosphoric acid to precursor can alter the pore size distribution obtained from crystalline cellulose such that, eventually, the structure is dominantly mesoporous [75].

1.1.3 Raw materials for activated carbon production

In recent decades, millions of tons of activated carbons have been produced by the carbon industry, consuming tons of precursors[85]. Nowadays, the manufacture of activated carbon from waste biomass is widely encouraging since by processing organic wastes, generating products of high commercial value is possible. A wide variety of raw

materials, some are illustrated in Table 1.1, have been used as a source to produce the activated carbons, citing: plant waste and biomass [73,86], synthetic polymers (tires) [87], petroleum coke [88], coffee ground [89], lignin, residues, and many others [90]. However, there are still many types of lignocellulosic biomass from different geographical areas which have not been converted into activated carbons yet.

Table 1.1. Survey of some wastes used for the preparation of activated carbon grouped according to their raw source [17].

wood	Eucalyptus Pine Quercus agrifolia Wattle China fir Wood Acacia Olive tree Softwood bark Mahogany sawdust Sawdust flash ash Sawdust	**Nuts Shells**	Pecan Almond Macadamia Cedar Hazelnut Pistachio Walnut Cherry	**Palm**	Fiber Pit Shell Stem of date Seeds Stones
		Stones and seeds	Apricot Peach Plum Date Olive Avocado Orange Mango	**Coconut**	Fiber shell
Husks	Rice Coffee bean			**Straw**	Rice Wheat
				Coffee	Ground Residue
Plant leaves	Luffa cylindrica Stipa tenacisima			**Vine shoot**	Olive cake

These raw materials should fulfill certain demands to be considered as potential precursors. They must be materials with high carbon contents and low inorganic compound levels to obtain a high yield during the carbonization processes. This characteristic is practically valid for every lignocellulosic waste [63]. In addition, they must be effective and economic materials. It is also important to note that the considered biomass must be plentiful in the region or country, where they will be valorized to solve any specific environmental issue [17]. Generally, agricultural wastes have little or no economic value, causing disposal problems. Therefore, using these wastes to produce carbon materials would reduce the cost of waste disposal and provide a potentially inexpensive alternative to the current commercial activated carbons [82].

1.1.4 Biomass as a precursor

Actually, the trend of science and technology is aiming towards renewable resources and eco-friendly processes. Thus, materials based on natural polymers including cellulose have attracted great attention. Biomass or as also known "lignocellulose" is defined as an organic material issued from plants and animals. It has a long history as a renewable source that can produce energy in different forms such as solid (briquettes), liquid (bioethanol and biodiesel), and gas (biogas and bio-H_2) [91]. When burned, the chemical energy in biomass is released as heat for industrial and domestic use while the produced steam is employed to make electricity [68]. Another benefit extracted from the biomass is to produce bio-fuel and carbonaceous materials since this last is rich in carbon elements [92]. A diversity of biomass types is available worldwide, counting among them:

- Wood and wood processing wastes: firewood, wood pellets, wood chips, lumber and furniture mill sawdust waste, black liquor from pulp and paper mills, birch, oak, and beech.
- Agricultural crops and waste materials: corn, soybeans, sugar cane, switchgrass, woody plants, algae, crop, and food processing residues, shells of various nuts (walnut, coconut, almond), fruit pits (olives, date, sour cherry, mango, and avocado…)
- Biogenic materials in municipal solid waste (garbage): paper, cotton, wool products, food, and yard
- Animal manure and human sewage.

The biomass waste is mainly a complex matrix composed of tissues that form part of the plant's cell's structure which differs from animal cells by the presence of cell walls. These walls ensure rigidity and mechanical support to the plant cell, maintaining the shape and the direction of the cell growth [93]. The part of woody cell walls of plants is constituted essentially by polysaccharides, phenolic polymers, and proteins. The walls of the lignocellulosic biomass have a complex spatial structure composed of three main biopolymers: (i) cellulose, a carbohydrate polymer that is wrapped by the dense structure formed by (ii) hemicellulose (another carbohydrate polymer) and (iii) lignin an aromatic polymer [92]. The fraction of these main components varies among species, with age, growth season, and with the natural recourses available during the synthesis [94]. Other

minor parts comprise the extractive components which are organic substances composed mainly of resin, fats, waxes, fatty acids, alcohols, terpentines, tannins, and flavonoids. These components have low molecular weight and are soluble in neutral solvents [82].

Table1.2. Content in (%) of cellulose, hemicellulose, and lignin in common lignocellulosic biomass [95]

Lignocellulosic source	(%)Cellulose	(%)Hemicellulose	(%)Lignin
Hardwoods	40–55	24–40	18–25
Coconut shell	34	25	38
Softwood	45–50	25–35	25–30
Nutshells	25–30	25–30	30–40
Corn cobs	45	35	15
Grasses	25–40	35–50	10–30
Paper	85–99	0	0–15
Olive stones	14	15	42
Wheat straw	30	50	15
Sorted refuse	60	20	20
Leaves	15–20	80–85	0
Cottonseed hairs	80–95	5–20	0
Luffa Cylindrica	60	30	10
Stipa Tenacisima	45	25	25

1.1.4.1 Cellulose

Cellulose is one of the oldest and most common organic and polymeric compounds on earth that has been used by humans since ancient times. Itis an inexhaustible source of raw material that represents about 1.5×10^{12} tons of the total annual biomass production [96]. Cellulose has a unique structure and excellent properties such as being biodegradable, renewable, inexpensive, and low-density material. In addition, it has a highly functional homopolymer with a linear chain, characterized by hydrophobicity, chirality, and high capacity for chemical modification [97]**.**

Cellulose is a carbohydrate polymer with the basic molecular format of $(C_6H_{10}O_5)_n$. The degree of polymerization reaches approximately 20,000 units depending on cellulose origin. Its structure consists of a long-unbranched chain polymer with repeating units of the monomeric D-glucose, a simple sugar [98]. The glucose units in the cellulose chain are generally in six-carbons rings, called pyranoses. They are covalently linked by □-(1-4) glycosidic bonds through acetal functions between the C-1 carbon atom of one pyranose ring and the equatorial OH group of the C-4 carbon atom of the next ring (Figure 1.7).

Since a molecule of water is lost when an alcohol and a hemiacetal react to form an acetal, the glucose units in the cellulose polymer are referred to as anhydro-glucose units [96]. Each glucopyranose unit is rotated by 180° from its neighbor due to the constraints of b-linkage performing very long straight chains. The repeated segment with a length of 1.3 nm is frequently taken to be a dimer of glucose, known as cellobiose [82,99].

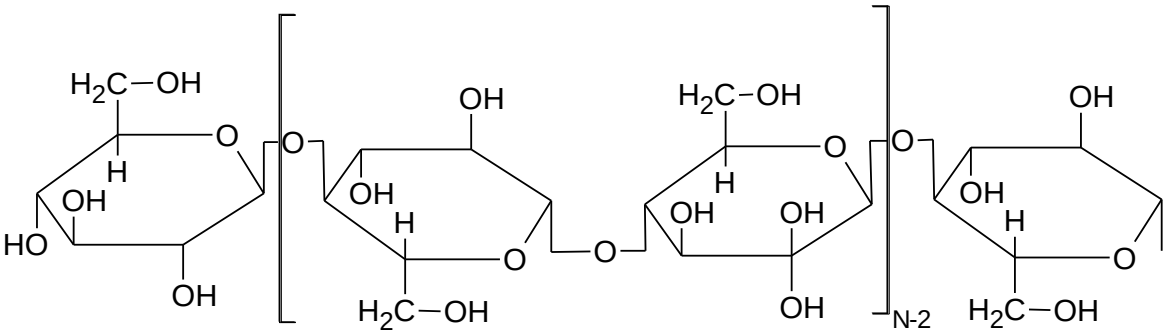

Figure 1.7. Chemical structures of cellulose

The stereochemistry of cellulose causes an extended conformation molecular chain (a semi-rigid structure), making it a good fiber-forming [95]**.** Cellulose molecules are arranged in regular bundles, forming crystalline regions, or in random geometry forming amorphous regions. Microfibrils of cellulose polymers are linked by hydrogen and van der Waals bonds and are protected by hemicellulose and lignin [92].

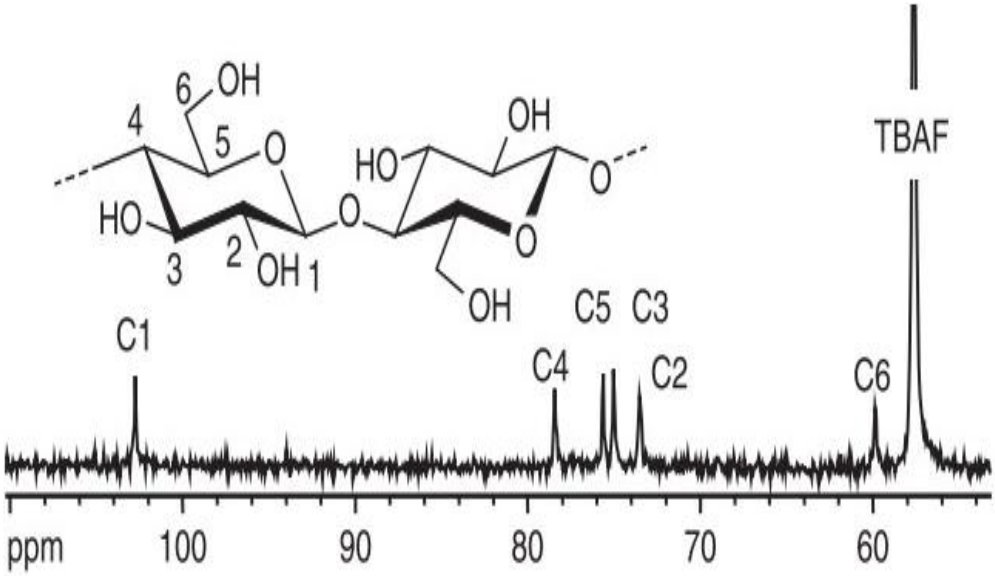

Figure 1.8.[13]C NMR spectrum of dissolved cellulose [100].

1.1.4.2 Hemicellulose

As previously stated, Hemicelluloses are one of the three main components of lignocellulosic biomass, representing ~20-40% of biomass by weight. These heteropolymers play a significant role in the structure of the plant cell wall. They constitute the matrix polysaccharides together with pectins in primary cell walls, whereas with lignin in secondary cell walls, they form the matrix polymers. Furthermore, they act as a binder between cellulose microcrystals to construct the cellulose microfibrils [101]. The hemicelluloses are a group of complex polysaccharides characterized by their solubility in alkaline solutions (e.g. KOH 1M) and their insolubility in water. The structural skeleton of hemicellulose (Figure 1.9) is composed of residues β-(1,4)-D-pyranose, where O_4 is in the equatorial position. Short side chains are attached to the skeleton [102]. In contrast to cellulose that contains only glucose units, their chemical structure contains other carbohydrates such as the hexoses D-mannose, D-galactose, D-fucose, and the pentoses D-xylose and L-arabinose [82].

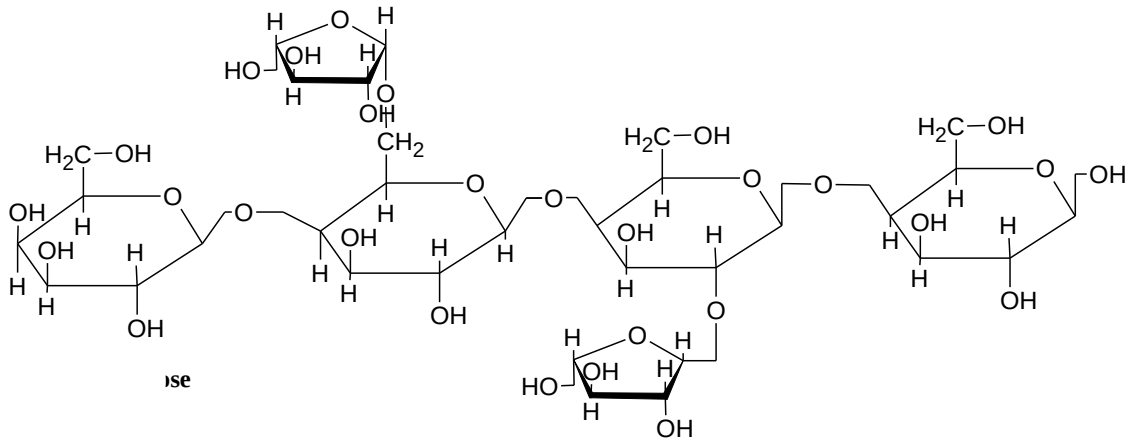

Figure 1.9. Chemical structure of hemicellulose [103].

Within the plant cell wall, hemicelluloses are a heterogeneous group of matrix-connected polymers of relatively low molecular weight which are associated with cellulose and other polymers. They bind closely to the surface of cellulose microfibrils and from one microfibril to another, by hydrogen bonds, glycine are ensuring cross-linking which contributes to strengthening the cell wall [104]. Hemicelluloses are linked with cellulose by inter- and intramolecular hydrogen bonds and with lignin by ester and ether bonds.

1.1.4.3 Lignin

Lignin (Figure 1.10) is the second largest renewable source on earth after cellulose. It is the third major component of lignocellulosic materials and an inevitable part of the plant cell wall [105]**.** It is a complex phenolic heteropolymer, mainly found localized in the intercellular structures. It provides hydrophobicity, rigidity, and strength to the plant's secondary cell walls [106]. The cross-linked phenolic polymers in its structure**,** ensures the cohesion of woody materials, increases their mechanical strength and limits their elasticity. Lignin represents about 10-30% of the weight of dry wood and 10% of the composition of Luffa [107].

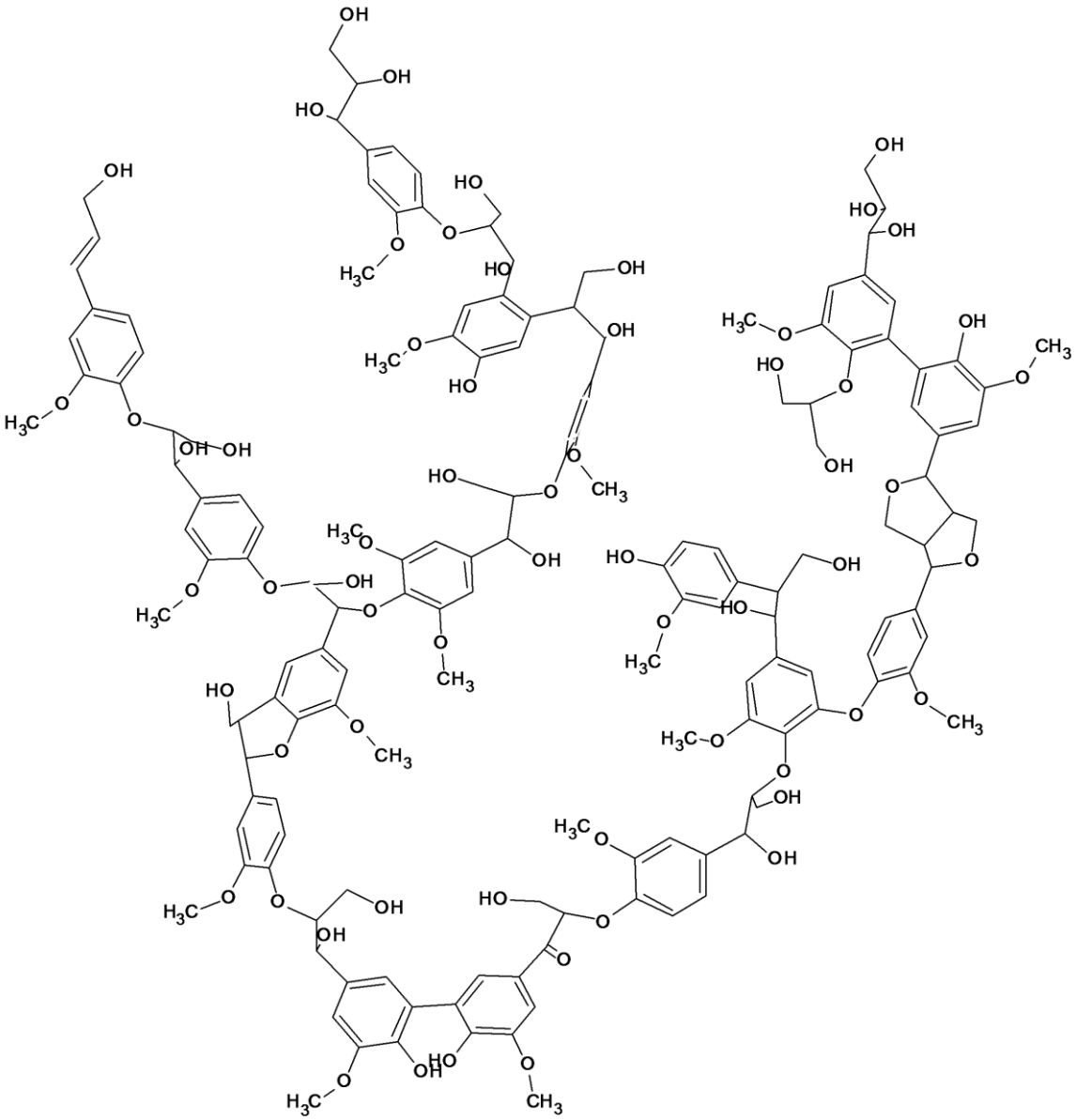

Figure 1.10. The structure of lignin as proposed by Adler [108].

Lignin is mainly an amorphous composed of branched long-chain polymer built up by the chemical linkages of alkyl-alkyl, alkyl-aryl, and aryl-aryl groups [109]. Itis connected by phenylpropane units toa three-dimensional lignin structure through various chemical bonds. The three types of monomeric precursors (Figure 1.11) forming lignin are:p-coumaryl alcohol-(H)(or as called4-propenyl phenol), coniferyl alcohol-(G) (4-propenyl-2-methoxy phenol), and sinapyl-(S) (4-propenyl-2.5-dimethoxyl phenol) [92]. These monolignols irregularly interconnect to form the polyaromatic structure of lignin.

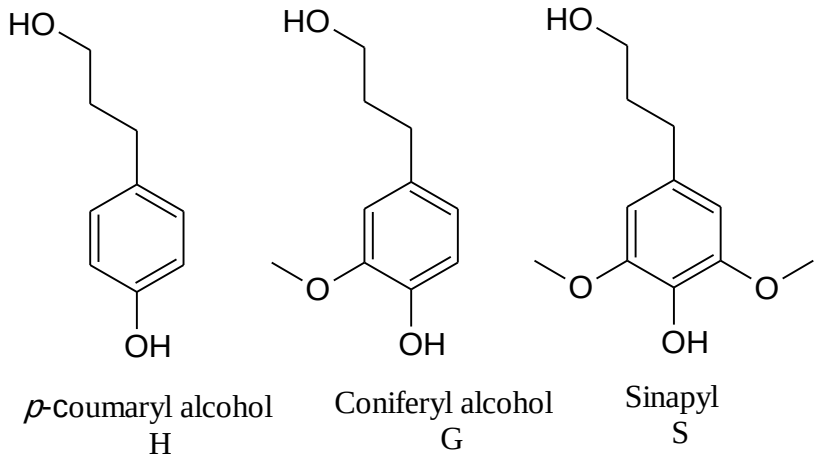

Figure 1.11. Chemical representation of the three monolignols, the building blocks of lignin [109].

1.1.5 Application of activated carbons

To date, activated carbons play a key role in different applications for several fields and areas of environmental and chemical engineering, electrochemistry, energy and fuel storage, biomedicine, heterogeneous catalysis, and adsorption. Being those two laters of great interest and the most commonly used. The majority of these applications have arisen because ofthemost distinctive features of activated carbons of high specific surface area, porous texture, and surface chemistry. The use of activated carbon in adsorption and heterogeneous catalysis is discussed in the following sections.

1.1.5.1 Activated carbon for adsorption

Adsorption is widely used in phase separation processes and the purification of wastewaters. It is a surface phenomenon between two different phases (solid and fluid) that permits the transfer of the adsorbate substrates to the solid adsorbent surface [110].

Generally, it consists of exploiting the solids' ability to specially concentrate pollutants substances from solutions onto their surfaces as illustrated in Figure 1.12. To this extent, activated carbon particles, as an adsorbent, are injected into the contaminated fluid and dispersed within for an appropriate time of contact [16]**.** Activated carbons with their tunable properties have extensively been used as versatile adsorbents for, both, vapor and liquid industrial purifications of mediums charged with numerous harmful organic and inorganic pollutants. Nevertheless, several studies are conducted in this way to ameliorate the properties and behavior of activated carbons for a better removal rate [111,112].

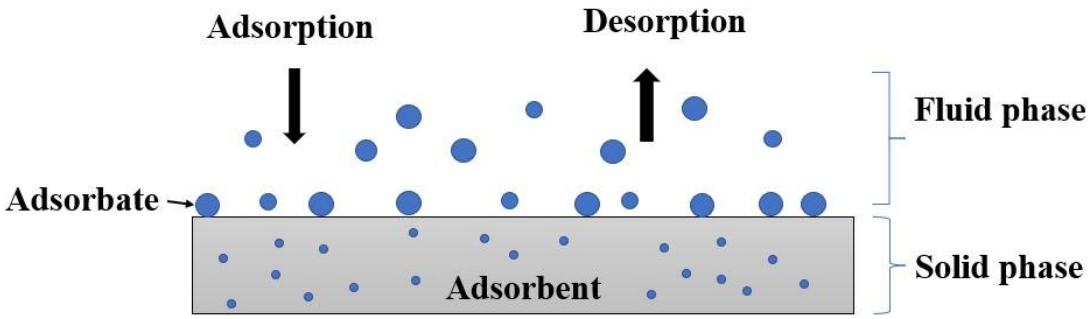

Figure 1.12. Schematic illustration of adsorption phenomenon.

As stated in several studies, the high surface area of activated carbon that can attain about 2000 m^2/g has led to an effective removal rate reaching 99%. [113]. Activated carbon adsorbents are employed principally to purify a wide range of liquid mediums, including wastewater, potable water, and industrial effluents (textiles, pharmaceuticals, chemicals…). In the textile industry, they are used to remove different organic dyes used during cloths coloration [87,114]. Since it is possible to find more than one pollutant in the discharges issued of this industry, competitive adsorption is possible by the unique texture of mixed porosity of activated carbons allowing the removal of more than one dye at once [115]. Activated carbons are also used to eliminate precious metal catalysts after the synthesis of pharmaceutical active ingredients [53,86]. Moreover, these adsorbents are used to remove organic compounds (phenol, benzene, toluene,..), undesirable taste compounds and color precursors from processed fruit juice, while color removal from natural-gas liquids is a more recent application [89,111,116].

Despite these outstanding properties and performance, once the adsorbate is saturated, an additional regeneration step is needed for further use. To overcome so, among others, this field is knowing constant attempts for better enhancement [17].

1.1.5.2 Activated carbon for heterogeneous catalysis

In addition to the predominant applications in adsorption, the use of activated carbon has extended to other fields of advanced applications as heterogeneous catalysis [117]. Over the last few decades, several studies dealt with the exploitation of carbon materials for the enhancement of the catalytic performance of different catalysts [118,119]. The use of carbons in catalysis depends mostly on understanding their surface chemistry and tunable microstructure. Hence, the developed surface area of activated carbons is the main reason for being considered to overcome the limitation of using nano-powdered catalysts. Two aspects for its use are considered, either as a catalyst or support for the catalyst's active particles, mostly for photodegradation applications [120]. The nature of carbon, quantity and, its structure are important parameters that characterize the photocatalytic properties. The combination of carbon with different semiconductors such as TiO_2, Cu, ZnO, Fe_2O_3,…etc. gave possibilities to obtain novel photocatalysts, particularly the development of visible light active photocatalysts for perspective future use [121]. Another advantage of carbons is to facilitate the recovery and recycling of metals, particularly of noble metals, as these supports can be burned off [55]. These materials bid incomparable flexibility in tailoring catalyst properties to specific needs.

- Activated carbon as catalyst

Different types of carbon materials have been used, including carbon nanotubes (CNTs), graphene, carbon blacks, granular and powdered activated carbons, and fullerene, with no particular difference in the contribution to the catalysis mechanism [122]. In addition to its textural properties, activated carbon is generally preferred because it is cheap, quite stable, and easy to manufacture. Carbon can form different structures with active catalyst particles, mainly, through doping, impregnation, and coating synthesis. The carbon is introduced in a way to form a thin porous layer on the surface of the semiconductor [123].Various studies reported that carbon, with both pores and functional groups, plays different roles once introduced in the structure of the catalyst. It was found

that, during the catalytic oxidation of sulfur dioxide, the basic functional groups present on the surface of carbons do not only provide adsorption sites but also contribute to the catalytic reaction of SO_2 oxidation to H_2SO_4 [124].

In photocatalysis by titanium dioxide, different ways in which carbon can modify TiO_2 particles, give some benefits for its photocatalytic activity. It is stated that when coating TiO_2 particles with porous carbon, a carbon atom is replaced with Ti or oxygen. This replacement forms oxygen vacancies that are responsible for extending the photocatalytic activity towards the visible range [125,126]. The same behaviors are observed for carbon-doping TiO_2 that cause the reduction of the TiO_2 phase. This decrease occurs by the introduction of oxygen vacancies into the rutile framework in an ordered manner providing relevant information about the visible light activity of the studied photocatalyst [126,127]. Furthermore, a red shift of the optical absorption edge was observed along with the formation of some impurities state in the band gap of TiO_2 leading to its decrease. Ergo, photodegradation proficiency for recalcitrant pollutants' removal could significantly be improved by preparing such photocatalysts.

- Activated carbon as catalyst support

Supporting the active particles of the catalyst is another application of carbons materials in the catalysis process. The best performance is expected by diffusion of pollutants to and from the surface through the proper pore size distribution and the interesting contribution of acid-base character when using carbon-supported catalysts [55]. A huge diversity of carbon materials with distinctive physical forms and properties can and have been utilized as catalyst supports. Utmost granular and powdered activated carbons are important with, recently, growing attention in related materials, such as activated carbon fibers, nanofiber, and nanotubes [128]. The main applications of carbon support include oxidation reactions, hydrogenation reactions, catalysis for reducing the environmental emission of gases [129]. With the high thermal stability in reducing atmospheres and their ability to simplify the preparation of well-dispersed metal particles on surfaces, carbon materials are used to support precious metals for hydrogenation reactions in the fine-chemicals industry [130].

For photocatalysis, composite materials are elaborated by loading the active phase particles on the surface of porous activated carbons, where the developed surface area and porous texture allow their good dispersion for better interaction of catalyst/pollutant [131]. The adsorptive carbon can improve the ability for pollutants adsorption to be concentrated on the active surface and through that favoring a higher degradation rate of organic compounds under UV irradiation [132]. Nevertheless, the presence or absence of surface functionalities can directly affect photocatalytic behavior as they grant the carbon surface with acid-base and hydrophilic character. Thus carbon supports can confer a relatively high amount of oxygen surface groups that could enhance the selectivity and subsequently lead to better photocatalytic performance [129].

In other words, the incorporation of activated carbon in photocatalysis permitted a profound understanding of the hybridization of adsorption with the photocatalytic activity of photocatalysts. The use of carbon as catalyst support relies largely on the relative inertness of its surface, which defines the interaction between active phases or between active phases and promoters, thus enhancing the catalytic behavior [133]. In the light of the above considerations, porous activated carbons are considered an excellent choice as catalyst support in a great number of reactions.

1.2 Luffa Cylindrica

The growing need for new, more efficient, economical, and biodegradable materials for the removal of toxic products from aqueous effluents, has been the subject of numerous studies. The use of biomass as a precursor to producing these materials has received significant credibility over recent years [107,134]. Luffa cylindrica fibers are one out of many possible sources, but still, only a few are devoted to its study [135,136].

1.2.1 Botanic properties of Luffa Cylindrica plant

Luffa cylindrica (syn Luffa Aegyptica) is commonly called sponge gourd, or loofah sponge. It is a herbaceous plant, part of the cucurbits family which includes about 130 different genera and about 800 species of medicinally important plants [137]. Luffa is generally cultivated in tropical and subtropical areas as Asia, North Africa (Algeria), central and south America. The plant is a common vine with rounded leaves and yellow flowers [138]. The color of the fruit of Luffa at the tender stage is green and yellow when ripe. The fruits are smooth and cylindrical with white flesh. The length of the fruit is from 30 to and 40 cm contains from 50 to 60 seeds (Figure 1.13) [139]. It is considered one of the most lignocellulosic materials rich in cellulose (60%), with 30% of hemicellulose, and 10% of lignin content [140].

(a) (b)

Figure 1.13. Luffa cylindrica, (a) young fruit, (b) ripe and dry fruit

Luffa cylindrica is an annual climbing plant with a height reaching up to 6 meters and a width of 8 cm. The leaves are oval, cordate, and webbed, often wider than long. The flowers, whether male or female, are bright yellow (Figure 1.14). The female flowers are solitary and the fruits are cylindrical, rounded, with a dense vascular network in the wall. The seeds are black if the fruit is mature and white if the fruit is young and 0.5 to 1 centimeter long [141].

(a) (b)

Figure 1.14. Luffa cylindrica (a), grains of Luffa cylindrica (b)

The Luffa needs a very long growing season to ripen in dry sponges. The seed should be sown after the earth is completely warm in the spring. It needs a moisture environment while growing and good exposure to the sun. It prefers a pH of about 6.0 to 6.8. Excessive water can result in weak growth and root disease. While it can be reduced in late summer to slow the growth rate and encourage fruit to harden in the distance.

1.2.2 The architecture of the sponge

The fruits of Luffa cylindrica have a fibrous vascular system. The struts of this natural sponge are characterized by a microcellular architecture with continuous micro hollow channels (macropores with a diameter of 10-20 μm) that form the vascular packets and report a multimodal hierarchical system of pore [142]. The fruit admits several distinct parts from the inside out (Figure 1.15) according to Zampieri et al. [143]:

- The central part of the fruit represents the core or the fillet;
- The inner surface and the outer surface of the sponge;

• The middle part which is consisted of a significant number of vascular bundles that link between the inner wall and the nucleus.

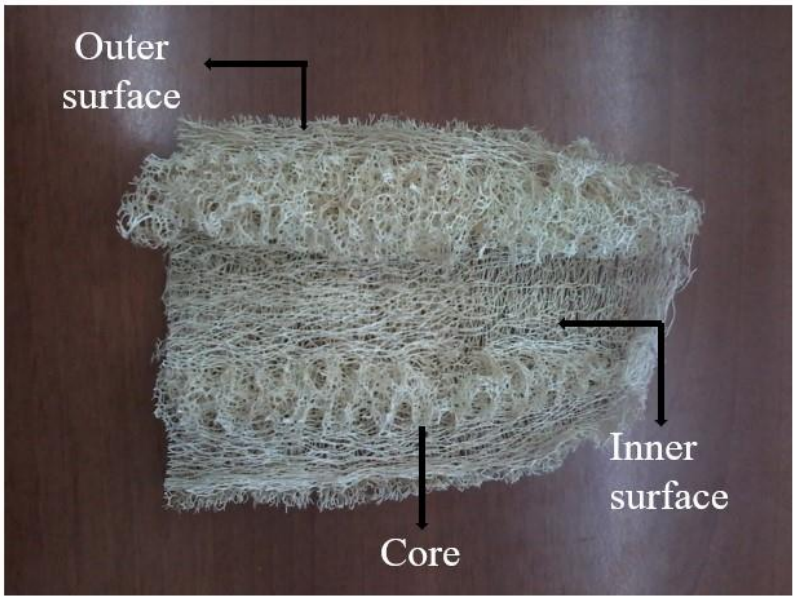

Figure 1.15. different parts representing the architecture of Luffa sponge

1.2.3 Chemical properties

- Concentrated hydrochloric and phosphoric acids destroy fibers at room temperature, and concentrated nitric acid converts cellulose into nitri-cellulose [112].
- The fibers treated with the NaOH solution purify the cellulose by removing the other constituents such as lignin present in the fibers [144].
- Oxidants (bleaching agent, hydrogen peroxide, EDTA,…) in low concentrations, destroy the dye and remove lignin from the fibers. At high concentrations, they degrade the tissues of Luffa cylindrica fibers [112].

1.2.4 Types of Luffa

The Luffa can be classified according to shape and size into several types:

- Luffa Acutangula Roxb. Ribbed Pipangaille

It is an angular gourd, cultivated since antiquity in Asia (China – India), and can also be found in Africa in savannah areas (Figure 1.16). Young fruits with longitudinal ribs are consumed and marketed under the name of Chinese okra even though their bitterness.

They contain unwinged seeds. In Asian pharmacopeia, they are used as purgative and vomitive (seed and root), diuretic (stem), and for the treatment of jaundice [145].

Figure 1.16: Fruit of Luffa Acutangula Roxb

- Luffa Cordifolia Blume

Synonym Thladiantha cordifolia, Cogniaux, Cordate-leaved Luffa, native to the temperate forests of Asia, present in India, Nepal, Burma, Thailand, Vietnam, and China.

- Luffa Operculata Cogn

Synonym Luffa purgans Mart, native to South America (Brazil) in the tropical zone. The angular stem can reach three meters in height. Its broad kidney- or heart-shaped leaves are three to five lobes long and are 10 or 12 cm long (Figure 1.17). The pale-yellow axillary flowers are monoecious and they produce a plum-sized fruit, pointed like a beak. This gray fruit resembles a squash, with longitudinal veins provided with many small prickles. The interior is luscious, with a fine network of fibers and flattened seeds of light brown color. It is generally used in traditional pharmacopeia.

Figure 1.17. Fruit of Luffa Operculata Cogn.

- Luffa Echinata Roxb

widely used in Asia. The fruits are ashy, oblong, ovoid having 2-5 cm length, and densely covered with 4-7 mm long bristles. Seeds are ovate, black 4-5 mm long, 3-5 mm broad, and 2 mm thick (Figure 1.18) [146]. The stem pieces are slender, yellowish-brown to blackish-brown in color, measuring 1.5-1.7 cm in length and 5-8 mm diameter [147]. It contains silymarin and several studies have been developed in India on its hepato protective properties [137].

Figure 1.18. Fruit of Luffa Echinata Roxb

1.2.5 Use of Luffa for different applications

The use of Luffa as an industrial plant began in Japan between 1890 and 1895, following the discovery of the suitability of the fiber, which is obtained from the fruit wall, in the manufacture of filters for steam and diesel engines [148].

- Domestic use

Young fruits, generally in Asia, are used as raw vegetables prepared like squash or eaten like cucumbers. In North Africa countries (Algeria, Morocco, Tunisia), once separated from the skin, flesh, and seeds, the fiber network after drying can be used as a bathroom sponge, pot scrubbers, and glass cleaning sponge. Since Luffa has a compact network of narrow fibers, its elasticity makes it useful for many products such as filters, packaging material, and baskets [149].

- Medical and biological

The plant is tonic, emetic, and diuretic and useful in the treatment of asthma and skin diseases. It is used internally for rheumatism, back mal, internal bleeding, and hemorrhoids. Dried fruit fibers are used as abrasive sponges in skincare, to remove dead skin from where it produces a soft glow on the skin. The circulation of blood that the sponge induces on the skin has been credited as relief for rheumatic and arthritic victims [150]. The fruits are anthelmintic, carminative, laxatives, emollient, and expectorant, also useful in fever, syphilis, tumors, and splenopathy. The vine is developed more generally for the fibrous interior of the fruits. It has purgative properties and is used for dropsy, nephritis, chronic bronchitis, and lung complaints. It is also applied to the body in putrid jaundice [151].

- Pharmaceutical

In the various traditional Brazilian pharmacopeias, fresh leaves (plastered) are used to treat boils, treat rhinitis, sinusitis, amenorrhea, and dropsy. Clinical trials were carried out in 1999, for use in homeopathy (homeopathic formula in combination with other components) in the treatment of acute sinusitis [145].

In addition to the exploitation of Luffa cylindrica in the above-cited domains, it has been the subject of different studies as a lignocellulosic material in different fields. Luffa has a good adsorbent character which allows its use for the adsorption of many pollutants such as heavy metals [115,152,153] and organic dyes [142,154]. On another hand, the good physical and mechanical characteristics made it a suitable candidate to be used as a reinforcement of different composites materials to enhance their mechanical properties [155–157].

1.2.6 Choice of Luffa cylindrica as raw material for activated carbon preparation

Even though the manufacturing process and intended application of the product are important considerations during the choice of the precursor, other factors are also important to be considered [107]. Therefore, and as previously mentioned, the choice of the precursor mainly depends on its cost, availability, environmental impact, and purity [85]. In addition to being widely cultivated and abundant in Algeria, Luffa cylindrica has other features that promote it to be considered as a potential precursor for activated carbons preparation. Luffa's chemical composition that consists mainly of cellulose (60%), hemicelluloses (30%), and lignin (10%), make it a good source of carbon regarding the polymeric structure of these constituents [135,158]

In addition, the Luffa cylindrica network shows the microsponges structure containing between 200 and 500 microcellular fibers leading to the highly accessible volume [100]. for this, and because of its unique structure, the Luffa Cylindrica was chosen as a suitable precursor for the preparation of activated carbons.

1.3 Heterogeneous photocatalysis

Photocatalysis, as well as systems or materials related to this area, are the trending studied fields of this century. It is regarded as a promising cost-effective approach for the degradation of numerous recalcitrant organic pollutants. In contrast to other conventional techniques that base on the separation or transfer of targeted pollutants to another phase, photocatalysis has the advantages of : (i) inducing effective and efficient reactions under irradiations at room temperature for (ii) total elimination or reduction of harmful organic pollutants into CO_2, H_2O, and inorganic compounds [19]. For that, it has received much attention as a green technology able to establish ideal applications such as the production of H_2 and O_2 from water by splitting, reduction of heavy metal ions, CO_2 reduction, and total mineralization of organic molecules [159]. These processes are considered essential for solving the problems of environmental pollution and the world energy crisis by creating renewable energy resources**.** There are lots of expectations from its possible applications in various fields.

Several definitions have been attributed to photocatalysis. According to IUPAC, Photocatalysis is defined as the initiation of a chemical reaction under the effect of a source of UV-visible light irradiation in the presence of a light-absorbent substance, called photocatalyst, without being involved [160]. The oxidation reaction occurs at the surface of the photocatalyst (semiconductor), which remains unchanged during and after the photocatalysis reaction [161]. The process is based on the excitation of the semiconductor under the effect of irradiations with an appropriate wavelength. As a result, and from a thermodynamical point of view, unfavorable reactions can be promoted thanks to the energy fetched by the irradiations [122]. The electronic structure of the semiconductors is characterized by a conduction band (CB) of high energy occupied with electrons, and the valence band (VB), of the low energy empty of electrons. The difference between the two bands forms an energy barrier called band gap (Eg), whose value varies from a semiconductor material to another (Figure 1.19) [162]**.** When the semiconductor is exposed to UV irradiation**,** the absorbed photon whose energy is equal to or higher than the band gap of the semiconductor creates a charge separation as an electron emigrates from the valence band (e^-_{VB}) to the conduction band leaving behind a hole (h^+) in the valence band [163]**.**

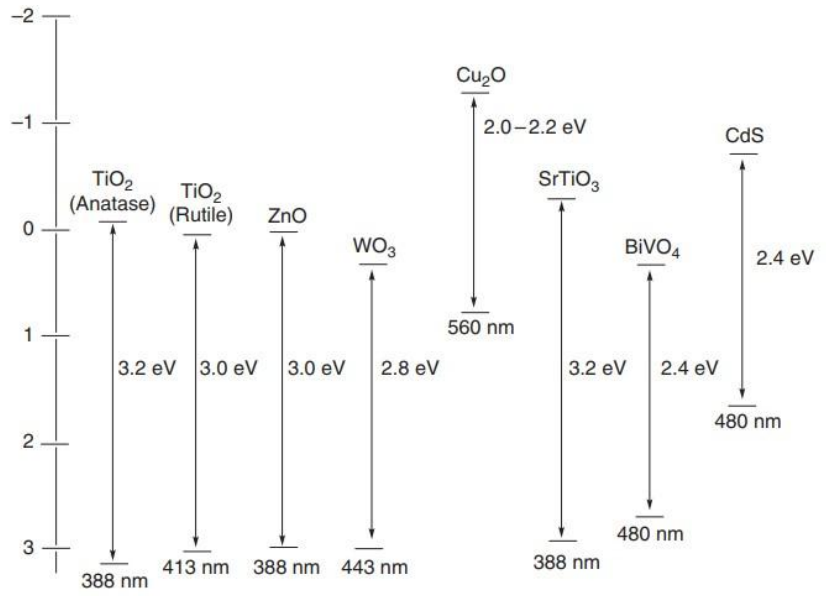

Figure 1.19. Band levels and wavelength edges of some semiconductors photocatalysts [164].

Generally, photocatalytic degradation reactions occur in three types of processes, oxidation, electron injection (Case of spectral sensitization observed in wet-type solar cell),

and reduction [165]. Commonly, oxidation is the photocatalytic decomposition process of organic compounds. It can be driven into five intermediary steps as follows: (1) transfer of the reactants from the fluid phase to the surface of the catalyst, (2) adsorption of pollutant onto the adsorbent surface, (3) oxidation reaction in the adsorbed phase, (4) desorption of the product, and finally, (5) transfer of the reaction products to the fluid phase of the interfacial region [166].

1.3.1 Mechanism of heterogeneous photocatalysis reactions

When a semiconductor (SC) absorbs photons of energy greater than the value of its bandgap (*hp>Eg*), an electron migrates from the valence band to the conduction band, creating an oxidation site (hole h^+) and a reduction site (electron e^-) (Eq. 1). After that, these charge carriers migrate from the bulk to the surface of the material. The excited electron reacts with electron acceptors such as the dissolved oxygen O_2 adsorbed on the semiconductor surface, to form superoxide radicals anions $O_2^{-\bullet}$(Eq.1.2) [167,168]. On the other hand, the generated holes form OH• and R• species through reacting with electron donors such as H_2O and OH^- anions (Eq.1.3 and 1.4 respectively). Furthermore, O_2• can form hydroperoxyl radicals, HOO•, by protonation (Eq.1.5). These oxidant radical species allow the mineralization of the pollutants (R) (Eq.1.6) [165,167]. The main produced reactions are represented in the following equations:

$$h\nu + SC \longrightarrow h^+ + e^- \quad (1.1)$$

$$(O_2)_{ads} + e^- \longrightarrow O_2^{-\bullet} \quad (1.2)$$

$$H_2O + h^+ \longrightarrow HO\bullet + H^+ \quad (1.3)$$

$$OH^- + h^+ \longrightarrow HO\bullet \quad (1.4)$$

$$O_2\bullet + H^+ \longrightarrow HOO\bullet \quad (1.5)$$

$$HO\bullet/HOO\bullet/O_2\text{-}\bullet + R \longrightarrow \text{Oxidized intermediates} \longrightarrow CO_2 + H_2O \quad (1.6)$$

It is worth noting that, in addition to the above-mentioned reactions, "scavenging" reactions can also occur (Eqs. 1.7-1.9), together with charges recombination (Eq.1.10). This last reduces the efficiency of the photocatalyst [122]

$$HO\bullet + H^+ + e^- \longrightarrow H_2O \quad (1.7)$$

$$HOO\bullet + HOO\bullet \longrightarrow H_2O_2 + O_2 \quad (1.8)$$

$$HOO\bullet + H^+ + e^- \longrightarrow H_2O_2 \quad (1.9)$$

$$e^- + h^+ \longrightarrow h\nu(\text{heat}) \quad (1.10)$$

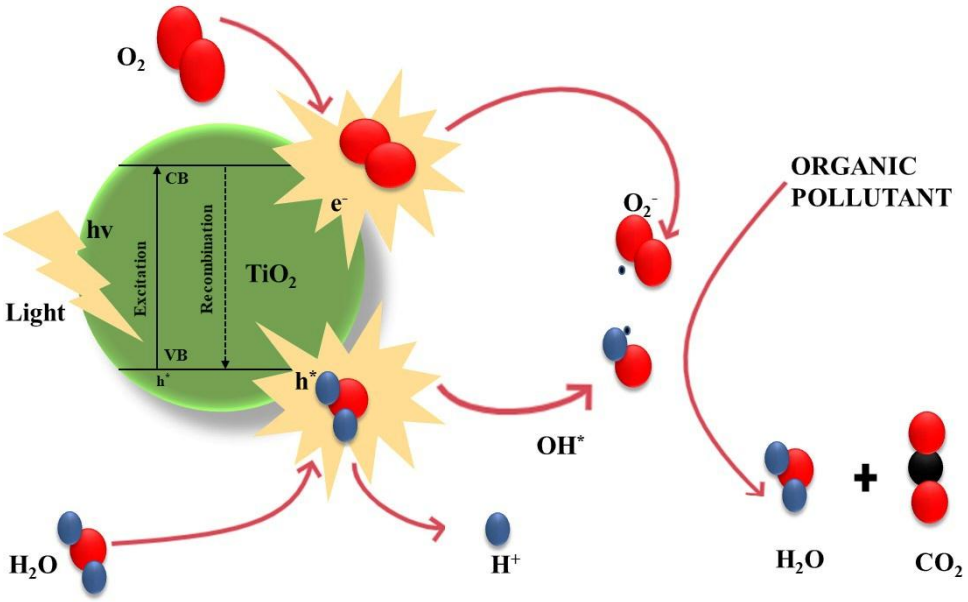

Figure 1.20. illustrates a schematic presentation of the photocatalytic mechanism of an organic pollutant on the TiO_2 photocatalyst surface, highlighting the major reactions and involved speciesafter semiconductor excitation.

1.3.2 Role of the reactive species (Oxidizing agents)

1.3.2.1 Hydroxyl radicals

Hydroxyl radicals are the most powerful oxidants if compared to other oxidizing species exploited in advanced oxidation application with an oxidation potential (E^0) of +2.80 V [169]. These radicals are non-selective and can promote a fast reaction by diffusing far in the reaction environment to reach the target compound for total oxidation regardless of their very short life time. It instantly turns any molecule, existing in its path, into a free radical by eliminating its electrons [170]. They are generated via the oxidation of both water and hydroxyl groups by the positive holes (h^+) of the valence band, and molecular oxygen by the electrons of the conduction band, and having a redox potential of 2.8 V.

The oxidation of organic pollutants by hydroxyl radical can be resumed in four possible ways: (1) The adsorbed HO• oxidize pollutant molecules close by the surface of the photocatalysts, (2) free HO• can oxidize adsorbed organic molecules inversely. (3) Oxidation can occur while both the HO• and the pollutant are in the adsorbed phase and

finally, (4) free hydroxyl radicals may react with pollutant molecules in solution although it rarely occurs [171].

1.3.2.2 Positive electron holes

The positive electron-holes (h^+) are created when a VB electron migrates to the CB. They have a strong redox potential ranging from +1.0 to +3.5 V [171]. The oxidation with these holes could occur in two ways, either direct or indirect. Indirect oxidation via reaction with hydroxyl radical (•OH) trapped on the surface with h^+, whereas direct oxidation via h^+ bounded to the metal surface before being trapped within the particle or at its surface [172].

One drawback related to the presence of these holes is that together with the photogenerated electrons can easily recombine within 10 nano seconds dissipating the energy as heat. This recombination is unfavorable since it results in low quantum yields and decreases the photonic efficiency of the photocatalyst [172]. The addition of appropriate scavengers or incorporation of trap sites on the surface (producing defects, surface adsorbents…), can significantly reduce or/and avoid this process as a result of separating the holes and electrons.

1.3.2.3 Superoxide radicals

It is highly believed that superoxide radicals (O_2^-• and HOO•) contribute a major part in the photo-oxidation of certain contaminants, particularly under visible-light irradiation. Their generation is considered a very important process that can control the photocatalytic reaction rate. Furthermore, the recombination rate is reduced through their efficient formation as they are formed via the reduction of oxygen molecules by electrons of the conduction band [171].

1.3.2.4 Dissolved oxygen.

In an aqueous medium, the photodegradation reaction is also affected by dissolved oxygen. It can be enhanced or inhibited depending on the pathway of the reaction. Conversely, it does not affect the adsorption of pollutants on the photocatalyst surface [159]. Oxygen also improves the generation of oxidant radicals as it usually functions as an electron acceptor by interacting with the photogenerated electrons on the conduction band. It is also an important reactant engaged in consecutive reactions of ring-opening in

the degradation of by-products [122]. Nevertheless, it is stated that dissolved oxygen could act as a "scavenger" or "inner filter" that decreases the light intensity in the reactor [173].

1.3.3 Irradiation sources

The name "photocatalysis" is composed of two parts, in which the first one refers to the "light". Consequently, irradiations are a vital condition for a photocatalysis process to be possible. Since the incident light is responsible for the excitation of the semiconductor photocatalyst, the photoabsorption of the light results in the generation of the charge carriers (h^+_{VB} and e^-_{BC}) responsible for different photochemical reactions on the semiconductor surface [174]. There are two sources widely used for irradiation during the photocatalysis reaction, artificial and natural light sources [164].

1.3.3.1 Artificial light source

In heterogeneous photocatalysis, artificial irradiations have been preferred over natural light as the fraction present in the artificial lamp employed is higher than that in sunlight (only 5-8% of the solar spectrum) [175]. Artificial light sources can be found in the form of UV lamps, lasers, or light-emitting diodes (LEDs). These devices typically emit either longwave (315-400 nm) or shortwave (200-315 nm) UV radiation [176]. Unlike solar irradiation, UV lamps have a narrower, but very broad compared to UV lasers and LEDs, emission spectrum which falls within the UV and visible region. The UV region can be divided into UV-A covers 320-380 nm, UV-B ranges from 280 and 320 nm and UV-C refers to light with a wavelength below 280 nm [171]. Whereas, the visible region comprised several sub-regions of variant wavelength ranges.

Visible light continuum sources include Halogen and Tungsten lamps which emit radiations within 320–2,400 nm [171]. The ultraviolet continuum includes several sources, citing: Xenon arc lamp which emits radiation of wavelength 200-1,000 nm; Hydrogen (H_2) and Deuterium (D_2) lamps that emit 160-380 nm; High-pressure mercury vapor lamps with a maximum emission spectrum of 365.5 nm, Incandescent and fluorescent lamps [177].

1.3.3.2 Natural solar light

Solar radiation reaching the earth is composed principally of infrared radiation (40%), visible radiation (50%), and UV radiation that accounts for <10%. For a photocatalytic application, the activation of a photocatalyst by solar irradiation involves the adsorption of photons from sunlight having suitable photon energies to generate e^-_{cb} and h^+_{vb} [176]. Compared to expensive UV lamps, solar radiation in heterogeneous photocatalysis provides a low-cost and renewable alternative. However, solar photocatalysis systems require other complex designs and components that are expensive which limit their use [178]. On one hand, some semiconductors are not photoactive under sunlight irradiation because of their high band gap energy, thus further modification such as creating oxygen vacancies and combination with transition metals and nonmetal inorganics are required to enhance the activity of the photocatalysts under visible light [164]. On the other hand, CdS whose bandgap energy is equal to 2.4 eV, is responsive to visible light; however, it is not effective because, under illumination, CdS is photo-corrosive [161]. As a cost-effective natural source of UV irradiation, it is constantly a field of vigorous research.

1.3.4 Semiconducting materials

Semiconductors photocatalysis is the given term for a photocatalytic reaction when using semiconductors. They act then as catalysts without being consumed in the overall reaction. Various semiconductors have proved to be effective as photocatalysts for the degradation of many obstinate contaminants. Binary semiconductors as titanium dioxide (TiO_2), zinc oxide(ZnO), iron oxide (Fe_2O_3), cadmium sulfide (CdS), zinc sulfide (ZnS), tungsten trioxide (WO_3),gallium phosphide (GaP), and so forth, with TiO_2 showing the best performance [169]. They are mainly the most preferable for the favorable combination of their electronic structure, light absorption characteristic, charge transport properties, and excited-state lifetime. Furthermore, some ternary semiconductors have also been a subject of investigation including $SrZrO_3$, $PbCrO_4$, $CuInS_2$, Cu_2SnS_3, and so [179]. On the other hand, only a few studies have been carried out regarding the use of quaternary oxides and sulfides in comparison to binary and ternary ones. Some are summarized in Table (1.3).

The choice of the semiconductor to be used in the photocatalytic reaction is based on some important criteria. The most desired features are to be photoactive and photostable(chemical stability and to photo-corrosion), able to be excited in the presence of UV and/or visible light (suitable band gap energy); biologically and chemically inert; in addition being environmentally friendly and low-cost material [122].

Table 1.3. Band gaps of different binary, tertiary, and quaternary semiconductors[178]

Photocatalysts	Band Gap (eV)	Photocatalysts	Band Gap (eV)
WSe_2	1.40	WO_3	2.50–2.80
CdTe	1.49	ZnSe	2.70
CdSe	1.74	In_2O_3	2.90
Cu_2O	1.90	TiO_2	3.02–3.20
CuO	1.9	ZnO	3.20
ZnTe	2.25	GaN	3.44
GaP	2.26	SnO_2	3.50
CdS	2.40	ZnS	3.70
V_2O_5	2.70	MnO	3.60
$CuInSe_2$	1.00	$BiVO_4$	2.40
Cu_2SnS_3	1.16	$CuGaS_2$	2.53
$CuInS_2$	1.55	$InTaO_4$	2.60
$ZnFe_2O_4$	1.90	Bi_2WO_6	2.70
La_2CuO_4	2.00	BaTiO	3 3.00
$PbCrO_4$	2.30	$SrTiO_3$	3.40
$Cu_2ZnSnSe_4$	1.00	Bi_2AlVO_7	2.06
$Cu_{1.0}Ga_xIn_{2-x}S_{3.5}$	1.43–2.42	Bi_2InTaO_7	2.81
Cu_2ZnSnS_4	1.50	$FeZn_2Cu_3O_{6.5}$	2.70
$Li_2CuMo_2O_8$	1.54–1.65		

1.3.5 Titanium dioxide photocatalyst TiO_2

Among all existing semiconducting materials, titanium dioxide is by far the most widely exploited in heterogeneous photocatalysis applications [180,181]. It presents many advantages, among all, high chemical stability (under acidic and basic conditions) being a good compromise between efficiency and stability, non-toxic, cost-effective, and high oxidizing properties. This photocatalyst exists mainly in four distinctive polymorphs, namely anatase, rutile, brookite, and monoclinic TiO_2. Out of these crystalline phases, the

anatase phase exhibits the highest photoactivity [182,183], whereas the rutile is the most thermodynamically stable [184]. Figure 1.21 shows the structure of the main three crystalline phases of TiO_2.

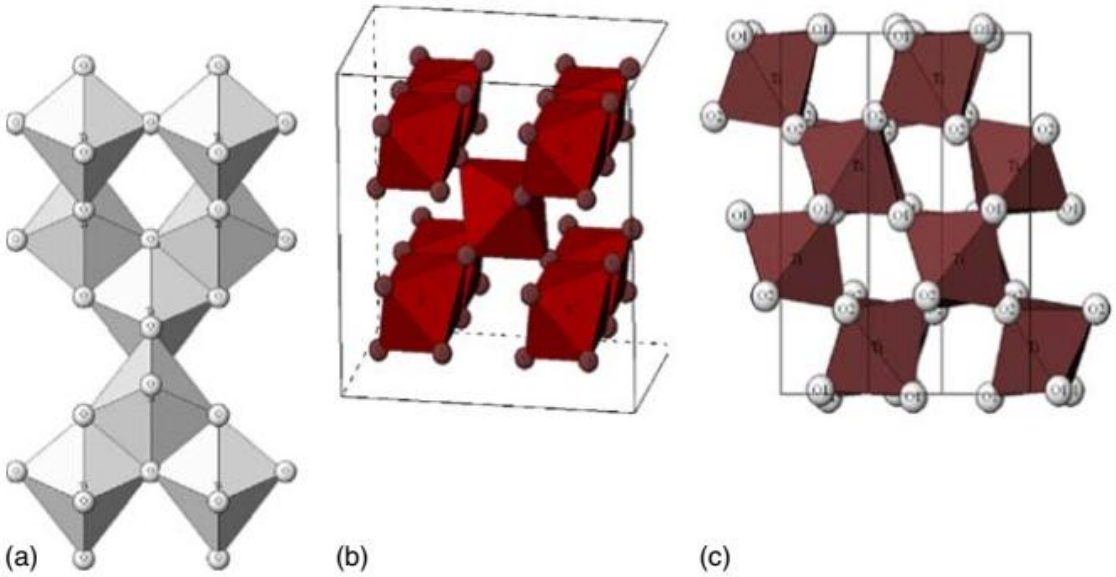

Figure 1.21. Illustration of the TiO_2 crystalline phases (a) anatase, (b) Rutile, and (c) brookite [185]

TiO_2 bears a high oxidizing potential once exposed to light, resulting in the decomposition of organic and inorganic substances even at low concentrations. The irradiation with a suitable wavelength promotes the generation of charge carriers (e^-_{CB}/h^+_{VB}) needed for carrying out the redox reactions, thereby, mineralization of the targeted contaminants [170]. Nevertheless, impurities or defects are found in the crystal lattice of TiO_2 as the oxygen vacancies due to the presence of Ti^{3+} ions. They are responsible for additional electronic levels (donor or acceptor) located inside the forbidden gap of the semiconductor, thus, explaining the large band gap value (3.2 eV), which is a disadvantage regarding its use in photocatalysis [179]. However, several attempts are made to enhance TiO_2 efficiency.

1.3.5.1 TiO_2 degradation mechanism

Under irradiation, TiO_2 generates electrons in the conduction band (e^-_{CB}) and holes in the valence band (h^+_{VB}) [177]. The photogenerated electron/hole pairs (e^-/h^+) exhibit fast recombination (within 10 ns) in the same time of formation, however, a while after forming (found to be 250 ns), the remaining e^-/h^+ pairs are trapped at the balk surface

prepared for the oxidation reaction [169]. The electrons reduce dissolved oxygen (or oxygen present in the air) to superoxide ions ($O_2^{\bullet -}$), that on further reduction gives rise to hydrogen peroxide H_2O_2. The recombination of the electron-hole pairs is prevented as the electron is consumed by O_2. The following equations highlight the main reactions that could occur during the photodegradation activity of TiO_2 [122,164].

$$TiO_2 \xrightarrow{h\nu} h_{VB}^{+} + e_{CB}^{-} \quad (1.11)$$

$$O_2 + TiO_2(e_{CB}^{-}) \longrightarrow O_2^{\bullet -} + TiO_2 \quad (1.12)$$

$$O_2 + TiO_2(e_{CB}^{-}) + H^{+} \longrightarrow H_2O_2 \quad (1.13)$$

The photodegradation rate may increase when H_2O_2 reacts with superoxide ions. Hydroxyl ions, hydroxyl radicals, and oxygen are formed as the product (Eq. 1.14). Another possibility is that H_2O_2 would be reduced (Eq.1.15) into hydroxyl ions and radicals by the (e^-_{CB}).

$$O_2^{\bullet -} + H_2O_2 \longrightarrow HO\bullet + HO^{-} + O_2 \quad (1.14)$$

$$TiO_2(e_{CB}) + H_2O_2 \longrightarrow TiO_2 + HO\bullet + HO^{-} \quad (1.15)$$

Hydroxyl ions reaction with the valance band positive holes and oxidative decomposition of water generate •OH radicals. Under aerobic conditions, the recombination of these •OH radicals leads to the production of H_2O_2.

$$TiO_2(h_{VB}^{+}) + HO^{-} \longrightarrow HO\bullet \quad (1.16)$$

$$TiO_2(h_{VB}^{+}) + H_2O \longrightarrow HO\bullet + H^{+} \quad (1.17)$$

$$2\ HO\bullet \longrightarrow H_2O_2 \quad (1.18)$$

1.3.5.2 Water interactions with TiO_2 photocatalyst

As most of the photocatalytic reactions are carried out in aqueous solutions, the oxidation mechanism of TiO_2 photocatalysts on water has been roughly investigated. It is stated that the interactions between the photocatalysts and water affect extensively pollutants resulting in two possible degradation mechanisms involved in the formation of surface-bound peroxide species [186]. On the surface, triply coordinated oxygen traps photogenerated holes. Few of these holes diffuse to the bridging O at step, kink, or terrace sites. Water oxidation is considered to initiate from a nucleophilic attack by a water molecule (Lewis base) to a surface trapped hole (Lewis acid) at the bridging O, followed by a Ti-O bond breaking to form Ti-O•HO-Ti [187]. This mechanism is called a

nucleophilic attack. The second one is called the redox photooxidation mechanism. It is proposed that water oxidation is initiated by interfacial transfer of photogenerated holes to adsorbed H_2O, to form adsorbed OH radicals [169].

1.3.5.3 Sol-gel method for TiO_2photocatalysts preparation

Several techniques have been used to synthesis TiO_2 photocatalysts with different properties depending on the desired chemical and physical properties for its application. The Sol-gel approach is a simple low-cost technique, principally used in the production of metal oxides. It can accurately control the chemical composition ofthe resulting product since it consists of using, as starting materials, chemical solutions containing the corresponding metal ions under low temperature [27]. The precursors represent the key role in determining the morphology of the deposited photocatalyst particles. They may produce an extensively integrated (gel-like) network of discrete particles or polymers [188]. The sol-gel approach ensures uniform dispersing in the final product. During the synthesis, the metal oxides undergo several hydrolysis and condensation reactions to produce inter-linked connections of metal centers (M) that are connected by oxo (MO-M) or hydroxy (M-OH-M) linkages [188]. Removal of the excess solvent by the drying process drives a volume shrinkage and densification of the photocatalyst. The drying step is tailed by thermal treatment for further poly-condensation and enhancement in the mechanical properties and structural stability of the final photocatalyst [126].

CHAPTER II

2 CHAPTER II: EXPERIMENTAL METHODS

2.1 Materials

All the reagents used to accomplish the present work are grouped in Table 2.1 indicating their Molecular formula, purity or concentration, physical state, and the provider company/group.

Table 2.1. Different materials used during the experiments.

Product	Molecular formula	Purity / concentration	Physical state	provider
Phosphoric acid	H_3PO_4	85%	Liquid	Panreac
Nitrogen	N_2	100ppmv	Gas	
Titania dioxide (P25 Airoxide)	TiO_2	99.5%	solid	Evonic
Titanium (TTIP) tetraisopropoxide	$C_{12}H_{28}O_4Ti$	97%	Liquid	Sigma-Aldrich
Acetic Acid	$C_2H_4O_2$	≥99.5%	Liquid	Panreac
Absolute Ethanol	C_2H_6O	≥99.8%	Liquid	Sigma-Aldrich
Malachite green Oxalate (N, N, N', N'-Tetramethyl-4,4'-diaminotriphenylcarbenium oxalate)	$C_{52}H_{54}N_4O_{12}$	≥90%	Solid	Sigma-Aldrich
Methylene Blue (3,7 bis(Dimethylamino) phenazathionium chloride)	$C_{16}H_{18}ClN_3S \cdot xH_2O$	>97%	Solido	Sigma-Aldrich
2-propanol	C_3H_8O	≥99.5%	Liquid	Sigma-Aldrich
Benzoquinone	$C_6H_4O_2$	99%	Solid	Sigma-Aldrich
Methanol	CH_3OH	99.8%	Liquid	Sigma-Aldrich

2.2 Preparation methods of the materials

2.2.1 Preparation of Luffa activated carbons (LACs)

The Luffa cylindrica sponge used in this study in order to prepare the activated carbon precursor was collected from the region of Metidja in northern Algeria between November and December 2017.

- Pre-treatment of Luffa cylindrica sponge

After removing the dried skin, *Luffa Cylidrica* fruits were washed several times with boiled water to remove dust and seeds. An additional washing step with distilled water is performed to remove organic impurities. The sponges were then oven-dried at 105 °C for 24 hours. After that, the dried fibers were cut into pieces and melded using a blunder before being sifted to the desired fraction of 800 µm.

Figure 2.1. Pretreatment of Luffa Cylindrica fibers

- Chemical activation

Luffa activated carbons (LACs) have been prepared by a chemical activation method as proposed elsewhere [130], using 85% phosphoric acid (H_3PO_4) as an impregnation agent. The dried Luffa fibers were put in contact at reflux with phosphoric acid for 3 hours at 80°C. The H_3PO_4 to Luffa mass ratios (weight of H_3PO_4/weight of Luffa) used were 1, 3, and 5 $g.g^{-1}$. The resulting mixture was pyrolyzed and activated afterward using a conventional tubular furnace at three different temperatures of 500, 550, and 700°C with a

heating rate of 5°C/min, and under a continuous nitrogen flow fixed at 60 mL/min for two different residence times of 1and 2 hours. Once the activation time was over, the samples were kept inside the furnace for cooling.

- Washing and drying

A washing step was strongly needed to extract any residual molecules of the activating agent obstructing the obtained carbon's pores, and thus liberate the porous structure of the activated carbons. For that, the prepared carbonaceous solids were washed several times with distilled water using a Soxhlet extractor until a constant neutral pH is reached. The samples were oven-dried at 105°C for 24h.

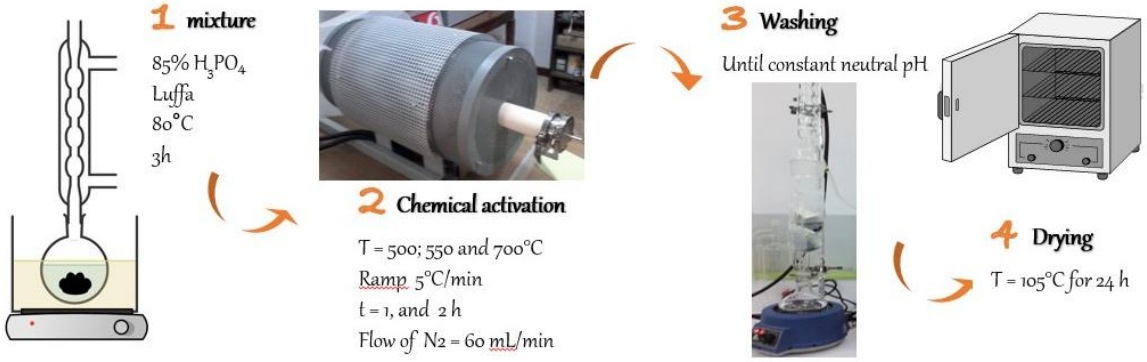

Figure 2.2. Process of Luffa activated carbons preparation

- Sample's nomenclature

The different activated carbons (LACs) were named as follows: LAC-R-T°-t, the material name (LAC), followed by the impregnation ratio, then the thermal treatment temperature in Nitrogen, and finally, by the activation time. As an example, sample LAC3-500-1 has been prepared with an impregnation ratio of 3g of H_3PO_4 per 1g of the precursor, with a thermal treatment at 500°C for 1 hour.

2.2.2 Synthesis of Titania TiO_2 based photocatalyst

Different hybrid photocatalysts containing TiO_2 and LAC have been prepared using two methods, the mechanical mixing method, and the sol-gel method. Commercial P25 TiO_2supplied by Degussa (named TP), and Titanium tertaisopropoxide (TTIP) were used

as titania's particles sources for the preparation of the photocatalysts. The optimal LAC developing an interesting surface area and prepared with moderate conditions has been chosen as a support for the preparation of the composites. The detailed processes are as follows:

2.2.2.1 Mechanical mixing method (MM)

Titania P25 and LAC3-500-1were mechanically mixed, in which 0.3 g and 0.1 g of LAC with 0.7 g and 0.9 g of P25 were respectively blended in an agate mortar, in a way to get 70% and 90% Titania loading.

2.2.2.2 Sol-gel synthesis (SS)

- In presence of acetic acid (SG)

The first series of photocatalysts supported on LAC3-500-1 were prepared by a sol-gel method as described by Amorós et al. [189] as follows: At 0°C, 9.3 ml of Titanium isopropoxide were stirred and mixed with 17.3 ml of acetic acid. All reactants have been used without further purification. Then, a mixture of a convenable mass of LAC3-500-1needed to have 70 and 90 wt. % titania contents in the final product and 197.5 ml of distilled water was added to the previous mixture of dropwise under continuous stirring for 1 hour. The solution stirring continued for 5 hours and, after 30 min ultra-sonication, a homogenous suspension of TiO_2/LAC was formed. The suspension was dried at 100°C for 24 hours and the solid material obtained was crushed into a fine powder. The synthesis was also performed in the same conditions without the addition of LAC to obtain corresponding bare TiO_2 samples.

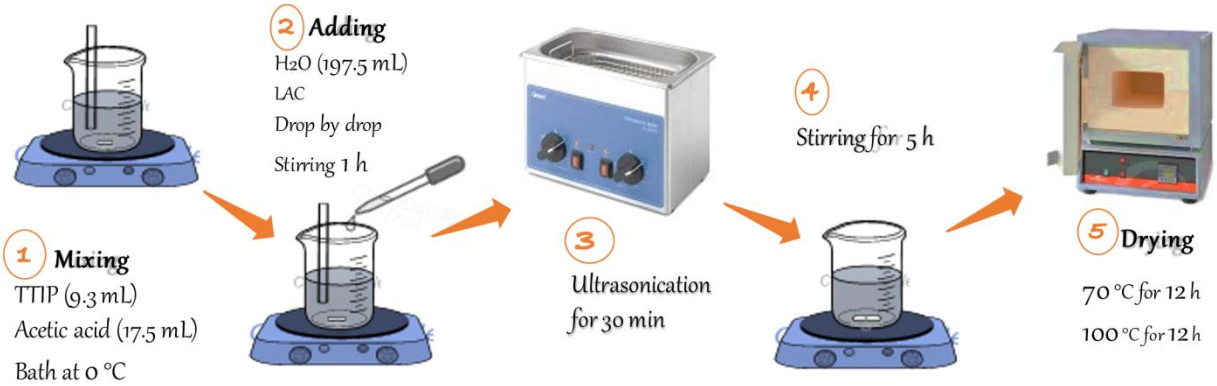

Figure 2.3. TiLAC preparation with Sol-Gel process in presence of acetic acid.

- Acid-free sol-gel (SG0)

For the prepared samples with an acid-free sol-gel, a mixture with 4 mL titanium tetraisopropoxide, 20 mL absolute ethanol (C_2H_6O, 99.8%, supplied by Panreac, Barcelona, Spain), and 0.4285 g of LAC (to have70 wt. % titania contents in the final product) was magnetically stirred at room temperature for 1 h, and then for 30 min in an ultrasonic bath. After that, a solution containing 4 mL of H_2O and 10 mL of absolute ethanol was added dropwise to the previous solution under continuous stirring for 1 h. The obtained product was dried at 100 °C for 12 h. Bare TiO_2 has also been prepared using the same method and conditions without the addition of LAC.

Figure 2.4. Acid-free Sol-Gel process for TiLAC preparation

The nomenclature of the photocatalysts prepared by the above-mentioned procedures is compiled in Table 2.2.

Table 2.2. Nomenclature and composition of all the photocatalysts samples used in the present study.

Nomenclature	**Description**	**Nomenclature**	**Description**
LAC	Luffa derived activated carbon	**LAC_TP-x/y**	x% LAC and y% TiO_2 P25, MM preparation method
TP	TiO_2 P25 from Degussa	**LAC_TSG-x/y**	x% LAC and y% TSG SS preparation method
TSG	TiO_2 prepared by sol-gel using acetic acid	**LAC_TSG0**	x% LAC and y% TSG0 SS preparation method
TSG0	TiO_2 prepared by acid-free sol-gel	**LAC_TSG0-350**	x% LAC and y% TSG0-350 SS preparation method
TSG0-350	Sample TSG0 calcined at 350 °C		

2.3 Physico-chemical characterization of the materials

To investigate the properties and quality of the different prepared materials, various techniques have been employed to characterize the produced luffa-activated carbons and TiO_2 based-composites. Most of the equipments used for this work were at the *Servicios Centrales de Apoyo a la Investigación (SCAI)* at the *University of Málaga*, and also in the laboratories of the investigation group *Materiales Carbonosos y Medio Ambiante* (*MCMA)* at the department of Química Inorganica e Instituto de Materiales at *University of Alicante*. Some others were performed at *the Center for Development of Advanced Technologies (CDTA)* in Algeriaand the laboratory *of Physical Chemistry of Interfaces of Materials Applied to the Environment* at *Blida 1 University*.

2.3.1 Activated carbon characterization

2.3.1.1 Ultimate analysis

Ultimate analysis commonly called, elemental Analysis, is used to quantitatively determine the elemental composition of carbon C, hydrogen H, nitrogen N, and sulfur S content, in samples of a very varied nature, organic and inorganic, solid, liquid and viscous, homogeneous, or easily homogenized. The analysis process is fully automated and is based on the complete combustion of the sample, between 950°C and 1300°C under an atmosphere of pure oxygen [33]. The percentage content of each item in the sample is processed taking into consideration the weight loss of the sample. Oxygen is obtained by subtracting the determined percentages of all other constituents from 100 [69]. This technique gives information about heteroatom contents and can provide approximate information on chemical structure, graphene size, and pore structure [190].

Table 2.3. Information about the chemistry of carbon obtained from organic elemental [190].

Element	Low content	High content
Carbon	- Low higher heating value (HHV) - Low graphitization grade	- High higher heating value (HHV) - High graphitization grade - Low amount of functional groups - Probably non-polar surface (with low content of O and N)basic surface (with low content of O)

Table 2.3. Continuation

Element	Low content	High content
Hydrogen	- High graphitization grade	- Low graphitization grade
Oxygen	- Low amount of oxygenated functional groups	- High amount of functional groups - Polar surface - Acidic surface
Nitrogen	---	- Polar surface - Basic surface

The ultimate analysis of our prepared Luffa activated carbons samples was carried out in a Carlo ERBA CHNO analyzer with autosampling and Oxygen content was estimated by difference [100-(C%+H%+N%+S%)].

2.3.1.2 Proximate analysis

Proximate analysis is a thermal analysis technique used in all types of applications. It is usually used for evaluating, with a temperature-programmed variation, the physico-chemical properties of a sample like thermal stability, oxidative stability, effects of different atmospheres, and sometimes the composition of multi-component systems [191]. In the case of activated carbon, the physical property measured is the weight in which an approach to estimate the content of moisture, volatile matter, fixed carbon, and ash on a dry basis is provided (see Table 2.4). The analysis is generally performed in an automated thermogravimetric system (TGA). It consists of measuring the absolute amount and rate of change in weight of a sample as either a function of time or temperature as the sample specimen is subjected to a controlled environment of temperature and atmosphere. The sample's pyrolysis is carried out in a gravimetric thermobalance system which automatically measures the sample's weight, as it is heated or cooled, usually under an inert atmosphere,in a furnace [192]. Furthermore, carrying out the analysis under nitrogen flow gives information about sample moisture near 100 °C and volatile matter in a temperature range of 100 and 950 °C. Whereas under oxidant atmosphere such as air, the burned material at 950 °C in a third step is fixed carbon made of more stable organic structures, and the non-combustible residue is the ash [190].

Table2.4. Information about the chemistry of carbon extracted from the proximate analysis [190].

Element	Low content	High content
Moisture	- High higher heating value - Low graphitization grade	- Low higher heating value
Volatilematter	- High graphitization grade - Low amount of functional groups	- High graphitization grade - High higher heating value - High amount of functional groups
Fixed carbon	- Low graphitization grade - High amount of functional groups	- High graphitization grade - Low amount of functional groups
Ash	---	- Low higher heating value

The proximate analysis for our prepared LACs was conducted in a METTLER TOLEDO model TGA/DSC 1 thermal analyzer. The tests have been carried out in 70 µl alumina crucibles in the temperature range of 30-950-30ºC with a nitrogen flow of 60 ml/min followed by a heating section in the air (60mL/min) up to 950ºC, with a heating-cooling rate of 10ºC/min and 2-2.5 mg of sample. The results were evaluated using the software STARe program version 15.01 of the METTLER TOLEDO STARe system.

2.3.1.3 Surface Morphology

Scanning electron spectroscopy (SEM) is an efficient magnifying imaging tool with a very high resolution developed to overcome human eye sight limitations.The German scientist and inventor, Manfred Von Ardenne, was the first one to introduce SEM to the scientific world in 1938, while the first marketed instrument came out in 1965 [193]. SEM is an instrument that generates magnified images that reveal numerous qualitative information of the specimen on a microscopic scale including its morphology (shape and size), topography (indicates the surface features, its texture, smoothness or roughness), composition (elements and compounds), and many physical and chemical properties of a material surface [194]. Surface investigation of the materials can beachieved through Electron Microscope (EM) and Optical Microscope (OM). However, usingfocused accelerated electrons beam in electron microscopy creates images, of the material surface, of much higher magnification (up to 300,000 times) with a better spatial resolution of 1 nm

data than optical microscopy which its resolution is very limited by diffraction properties due to the use of visible light photons that have a longer wavelength and thus are less energetic [195].

Morphology and microstructure of the prepared activated carbons were studied using scanning electron microscopy in a QUANTA, series 650 instrument. A carbon disc was used as a support for the finely powdered samples.

2.3.1.4 Textural properties

Physisorption of gas is one of the most important tools for the characterization of porous solids and powder materials' texture. It is a phenomenon of inert gas molecules (adsorbate), mostly nitrogen at -196 °C, adhering into a surface layer (adsorbent) of solid materialat a pressure less than the vapor pressure [196]. Although being nitrogen the most frequently preferred, other inert gases as argon and krypton could be also used for this type of analysis at a constant temperature of a liquid nitrogen cryostat for mesopores and micropores materials with low BET surface area like oxides. In those cases, only a part of the isotherm can be measured, but this still provides a BET surface area with high accuracy. Furthermore, the use of argon adsorption at -186 °Cor carbon dioxide adsorption at 0 °C is often preferred over nitrogen adsorption to accurately probe the small micropores. At a given temperature the amount of gas adsorbed on the porous and non-porous solid surface as a function of gas relative pressure is expressed by curves called adsorption isotherms [17,48]. The analysis of these isotherms provides large information about the specific surface area and pore distribution (micro-mesoporosity) of the studied material. The International Union of Pure and Applied Chemistry (IUPAC) recommends a classification based on six types of isotherms. When the adsorption and desorption curves in the isotherm do not coincide, adsorption hysteresis arises depending on particular features of the pore structure and underlying adsorption mechanism. A classification based on shape for those hysteresis loops is also recommended by IUPAC (Figure 2.5) [43].

- Adsorption isotherms

➢ **Type I:** This type of isotherms is characteristic of microporous solids having relatively small external surfaces area. The sharp uptake at relatively low P/P0

suggests the existence of a strong interaction between adsorbent and adsorbate, indicating the presence of micropores of a width less than 2nm. It is commonly found for activated carbons and molecular sieves zeolites. Type I(a) and I(b) isotherms are usually found for nitrogen and argon adsorption at -196 °C and -186 °C for materials having narrow micropores (width<∼1 nm) and materials having wider micropores and possibly narrow mesopores (<∼ 2.5 nm) respectively [43].

- **Type II**: characteristic of nonporous or microporous adsorbents representing monolayer-multilayer adsorption up to high P/P_0. This type could also be given by activated carbon having a wide pore distribution (micropores and mesopores of different widths) [43].
- **Type III**: is given by nonporous or macroporous solid. the adsorbent-adsorbate interactions are relatively weak in this case and the adsorbed molecules are groupedaround the most favorable sites on the surface with an infinite adsorption amountat the saturation pressure $P/P_0=1$ [43].
- **Type IV**: Type IV isotherm with a typical feature of final saturation plateau, describesthe adsorption behavior in mesopores determined by the adsorbentadsorptive interactions and also by the interactions between the molecules in the condensed state. In the case of type IVa isotherm, a hysteresis occurs for pores wider than 4 nm depending on the adsorption system and temperature, while with solids having mesopores of smaller width,reversible type IVb isotherms are detected [43,48].
- **Type V**: Type V isotherms are observed for water adsorption on hydrophobic microporous and mesoporous adsorbents. The shape of this type of isotherms is very similar to that of Type III at a low P/P_0 range which could be ascribed to relatively weak adsorbent–adsorbate interactions whereas at higher P/P_0 molecular clustering is followed by a pore-filling [43,197].
- **Type VI:** represents layer-by-layer adsorption on a highly uniform nonporous surface, generally obtained with argon or krypton at low temperature on graphitized carbon blacks [43].

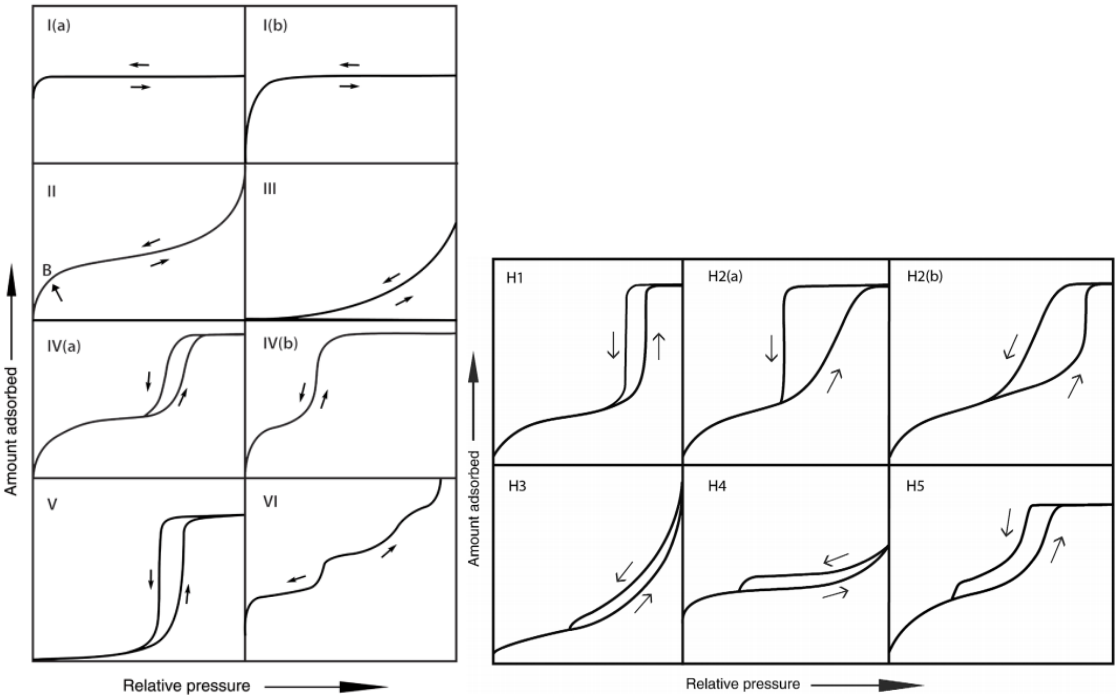

Figure. 2.5. IUPAC classification of physisorption isotherms and hysteresis loops [43]

The most important set of information that could be extracted from analyzing the adsorption isotherms are subsequently:

- Specific surface area

The specific surface area (S_{BET}) of porous materials is evaluated using the Brunauer-Emmett-Teller theory (BET) [16,48]. The BET equation Eq.(2.1) is applicable for type II and IV isotherms obtained by N_2 physisorption at -196 °C with a recommended relative pressure P/P_0 range between 0.05 and 0.35 [190].

$$\frac{\frac{P}{P_0}}{v\left(1-\frac{P}{P_0}\right)} = \frac{1}{vm\,C} + \frac{C-1}{vm\,C}\left(\frac{P}{P_0}\right) \quad (2.1)$$

where v is the volume of adsorbed gas, P is the gas pressure, P_0 is the relative vapor pressure, v_m is the monolayer capacity in moles, and C is a constant depending on the net molar energy of adsorption.

The plot of $[P/P_0]/v_m(1-(P/P_0))$ versus P/P_0 yields a straight line. The corresponding slope and intercept in the origin determine the characteristic parameters of the BET equation, v_m, and C respectively. The surface area S is then calculated according to equation 2.2[53].

$$S_{BET} = \nu_m . a_m . N_A . V_M \qquad (2.2)$$

Where S_{BET} is the apparent surface area of the porous solid expressed in m^2/g, a_m is the molecular area of the adsorbate (for nitrogen is 0.162 nm^2), N_A is Avogadro's number ($6.022\ 10^{23}\ mol^{-1}$), and V_M: molecular volume of gas under normal conditions of pressure and temperature.

- Total micropore volume (Φ< 2nm)

Using the data extracted from N_2 physisorption, the Dubbinin-Radushkevich (DR) method is well-known for the calculation of micropore volume in porous solids [198]. The equation is based on Polanyi's adsorption potential theory "the total micropore volume V_{micro} is a function of the adsorption potential E [199]. The total volume could be deduced through the plot of ln(w) versus ln (P/P_0). The DR equation is given as follows:

$$\frac{W}{W_0} = EXP[\frac{-1}{(\beta E_0)^2} . (RTln(\frac{P}{P_0})^2)] \qquad (2.3)$$

W and W_0 are the adsorbed volume at a pressure P, and total micropore volume respectively. P_0 is the saturation pressure. β is the affinity coefficient constant, E_0 is the characteristic adsorption energy dependent on the temperature and the nature of the porosity of the porous solid (e.g. activated carbon).

- Total porous volume

By assuming that the pores are filled with the adsorbate in the bulk liquid state with an isotherm type IV, the pore volume is then derived from the amount of vapor adsorbed at a relative pressure $P/P_0 = 0.95$ [43].

- Mesopores volume (2 < Φ < 50nm)

Mesopores are pores with width ranged between 2 < Φ < 50nm. The mesopores volume is assessed by the difference of the pore volume adsorbed at a relative pressure $P/P_0 = 0.99$ and $P/P_0 = 0.2$ [200].

Textural properties of the prepared LACs were characterized by physical absorption-desorption of N_2 at -196°C and CO_2 at 0°C in a Quantachrome Autosorb-6B

apparatus. The samples were previously degassed at 250°C for 4 hours. The apparent specific surface area (S_{BET}) was assessed using the Brunauer-Emmett-Tiller equation and the total porous volume ($V_{DR}(N_2)$), for pores with a diameter size< 2 nm, was determined using Dubinin-Radushkevich equations [196]. The CO_2 adsorption data provided the narrow micropore volume ($V_{DR}(CO_2)$) and surface area ($S_{BET}(CO_2)$) calculations using the Dubinin–Radushkevich equation [201]. Pore size distributions were obtained applying the 2D Non-local density functional theory (2D-NLDFT) heterogeneous surface model from the N_2 adsorption isotherm [202].

2.3.2 Hybrids' characterizations

2.3.2.1 Textural properties

Textural properties for the prepared hybrids were also characterized by physical absorption-desorption of N_2 at -196°C and CO_2 at 0°C in a Quantachrome Autosorb-6B apparatus. The same previous method and conditions used for LACs samples were adopted to assess the BET surface area, total micropores volume, mesopores volume, and total pores volume.

2.3.2.2 X-ray diffraction analysis

X-ray diffraction (XRD) is an indispensable technique in the materials characterization field to obtain information on an atomic scale from both crystalline and amorphous materials. The X-raywas accidentally discovered by the German scientist W. Röntgen in 1895, but not until 1912 that the phenomenon of X-ray diffraction of crystal powder was fully understood [203].

The analysis can provide information on phase identification and quantitative phase analysis crystal structure, phase transition, crystalline quality, orientation, and internal stress, etc. [204]**.** X-rays diffraction is a scattering phenomenon and a consequence of the interaction between electromagnetic radiations (of the same nature as light but very much shorter wavelengths) and periodically arranged atoms of the crystal solid**.** The relationship between an incident X-ray light and its reflection off from a crystal surface is explained by

Bragg's low that determines the diffraction parameters, wavelengths λ, and the lattice spacings *d* of the crystals. (equation2.4) [205].

$$n\lambda = 2d_{hkl} \sin\theta \qquad (2.4)$$

Where d_{hkl} indicates the distance between the atomic layers (*hkl* is Miller's index), λ specifies the wavelength of the incident X-ray beam, θ is the angle of maximum peak and *n* is an integer or as called the order of reflection.

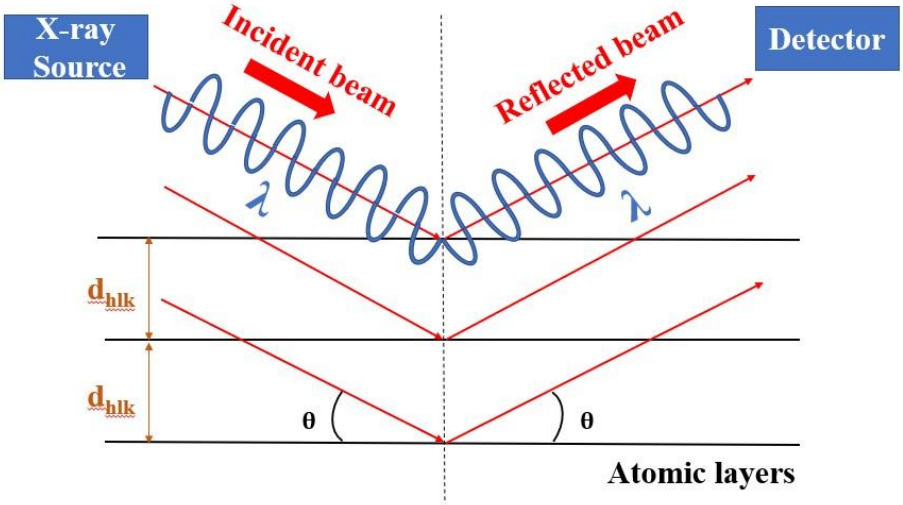

Figure 2.6. Schematic representation on the working principles of X-ray Diffraction

The percentage of crystalline TiO_2, phase composition, and crystallite size were determined by X-ray diffraction using the analysis method described by Cano-Casanova et al. [27]. For, both, TiO_2 samples and for TiLACs samples, XRD patterns were recorded with CaF2 (50%, w/w) using the equipment Miniflex II Rigaku (30 kV/15 mA) with Cu Kα radiation at a scanning rate of 2◦/min, in the 2θ range 6–80◦.

The Scherrer Equation (Eq.2.5) was used to calculate the average crystallite size (crystal size) as follows [206]:

$$B = \frac{K\lambda}{\beta\cos\theta} \qquad (2.5)$$

where B is the average crystallite size (nm); λ is the radiation wavelength (0.1540 nm for Cu Kα), K is the Scherrer constant (K = 0.93), β is the full width at half maximum intensity (FWHM) and θ is the angle associated to the main peak of the studied phase (2θ

values of 25.3, 27.5 and 30.8◦ for anatase (A), rutile (R) and brookite (B), respectively). The percentages of the anatase (A%) and rutile (R%) crystalline phases are determined according to the procedure reported by Jensen et al. using the succeeding equations [206],

$$A(\%) = \frac{\frac{A_{anatse(101)}}{Ac_aF_2(220)} \times 100}{1.25} \quad (2.6)$$

$$R(\%) = \frac{\frac{A_{rutile(110)}}{Ac_aF_2(220)} \times 100}{0.9} (2.7)$$

$A_{anatse(101)}$, $A_{rutile(110)}$, and $A_{CaF2(220)}$ are the areas of the peaks anatase (101), rutile (110), and the 100% peak of CaF_2(220) respectively. The constants 1.25 and 0.9 are the theoretical ratios between the area of the 100% anatase peak or the 100% rutile peak and the area of the CaF_2 peak in a 50% weight ratio.

2.3.2.3 Diffuse Reflectance UV-vis (DRUV-vis)

When light hits a surface, it can be reflected, transmitted, or absorbed. Reflection is the scattering of light back in the direction of the incident light. Transmission occurs when the light passes through a medium. Absorption occurs when some of the energy of the light is retained by the sample. Diffuse reflection occurs when a surface is not smooth. If the surface roughness is similar to or larger than the light's wavelength, the rays will scatter in a multitude of directions. In diffuse reflection, the law of reflection is still valid, but the angle of the surface is changing such that incoming parallel beams hit the different angles of the surface. The measurements are taken in UV-vis spectrophotometers coupled to an accessory integrating sphere of a diameter of approximately 50–250 mm and capable of collecting the reflected light flux while all the radiation reaches the detector in the integrating sphere after repeating reflections [207,208].

DRUV-vis spectra were collected with an Agilent Cary 7000 UV-Vis-NIR spectrophotometer equipped with an integrating sphere accessory, in the wavelength range from 200 to 800 nm. The absorption coefficient (α) was calculated as $\alpha = \ln(1/T)/d$, where T is the measured transmittance and d is the optical path length. Bandgap energy, Eg, was determined through the α value (m^{-1}) from a plot of $(\alpha h\nu)^{1/2}$ versus photon energy ($h\nu$), where h is Planck's constant and ν is the frequency (s^{-1}). The intercept of the tangent to the absorption curves was used to estimate the bandgap (Eg) value.

2.3.2.4 Surface Chemistry

- X-ray Photoelectron Spectroscopy

X-ray photoelectron spectroscopy (XPS) is a surface technique that provides an estimation of the chemical composition of materials surface up to few nanometers depths, the oxidation state of each element, the functional groups in (e.g. activated carbons and semiconductors), and measures the energy of internal atomic orbitals (binding energy)[209]. XPS is based on using monochromatic X-ray photons to excite an inner-shell electron. This core electron can be extracted out of the atom by absorption of a photon whose energy $h\nu$ exceeds the binding energy of the bond electron E_B, whereby the kinetic energy ($E_k = h\nu - E_B$)can be measured (Figure 2.7). The electronic states are characterized according to quantum numbers as core level C 1s, and O 1s [210].

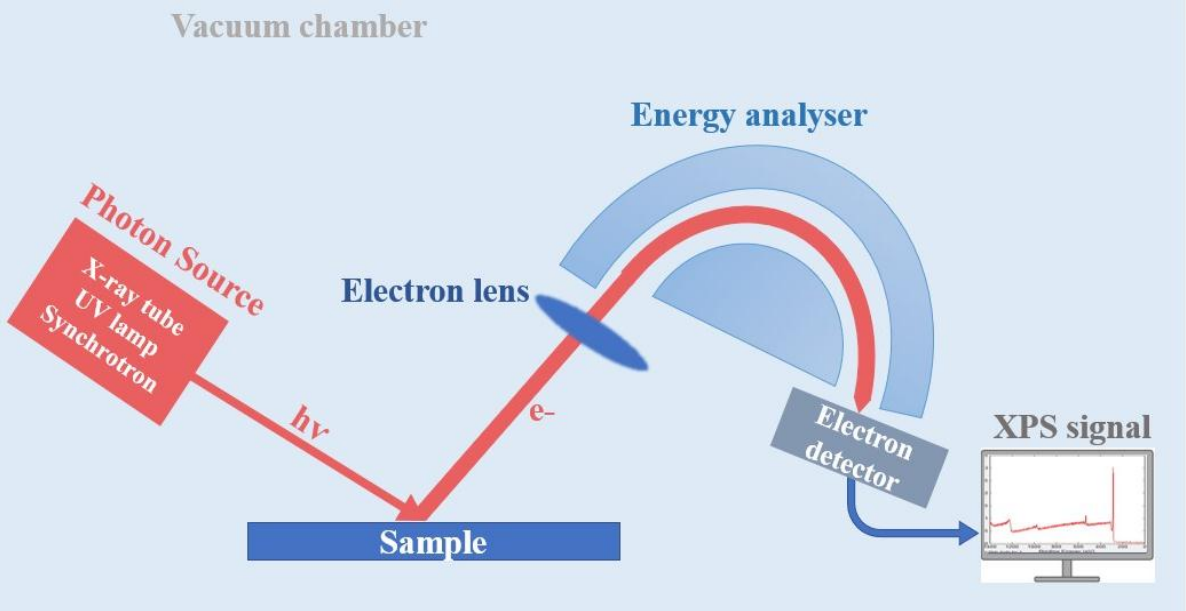

Figure 2.7. Schematic representation on the working principles of X-ray Photoelectron spectroscopy

The XPS characterization for the composite samples was performed using the Physical Electronics PHI 5700 spectrometer with non-monochromatic Mg Kα radiation (300 W, 15 kV, 12536 eV). and with a multichannel detector. Binding energy (BE) values were referenced to the C 1*s* peak (284.8 eV) from the adventitious contamination layer. The PHI ACCESS ESCA-V6.0 F software package and Multipack v8.2b were used for acquisition and data analysis, respectively. A Shirley-type background was subtracted from

the signals. Recorded spectra were fitted using Gauss-Lorentz curves to determine the binding energy of the different element core levels more accurately. The error in BE was estimated to be ca. 0.1 Ev.

- Fourier Transform Infra-Red

Fourier-Transform Infrared Spectroscopy (FTIR) is mainly a qualitative technique used for structural analyses of organic compounds through the collection of high spectral resolution data over a wide spectral range. The infrared radiation is absorbed selectively by the various bonds within a compound allowing the detection of specific bonds in the material, and thus, identification of the functionalities that exist on the surface. The width of the bands is due to the existence of several similar bands with a maximum at different frequencies because they are affected by vicinal functionalities. Fourier transform (FT) when coupled with infrared (IR), tolerates an improvement over signal/noise rate, energy throughout, accuracy, and fast scans. The assignment of the IR bands to different functional groups is made by comparison with adsorption/transmission bands of the organic compounds [211].

FT-IR spectra of our solid samples were registered in the mid-infrared and the close range (Bruker Vertex70, with a Golden Gate Single Reflection Diamond ATR System accessory). The spectral range was 4000-500 cm^{-1} with a 4 cm^{-1} resolution and 64 accumulations for spectrum acquisition.

2.4 Organic dyes removal from aqueous solution

The feasibility of using the prepared composites in the purification of water contaminated by textile dyes was investigated. Experimental set-ups were implemented for the removal of two organic cationic dyes, methylene blue (MB) and malachite green (MG), from an aqueous solution using a photocatalytic process with three different sources of irradiation. UV irradiations have been used for MB photodegradation, while simulated solar light has been employed for MG photodecomposition.

2.4.1 Methylene blue removal

The photodegradation activity of the synthesized composite materials under UV irradiation of the model compound, methylene blue dye, from an aqueous solution was performed following ISO procedure for photocatalytic characterization [212]. The initial MB concentration was 6.0×10^{-5} M, the photocatalyst dosage was 1.25 $g \cdot L^{-1,}$ and the temperature was fixed at 20 °C. The following two types of experiments were carried out: a) the mixture MB solution and photocatalyst was maintained under stirring in the dark for 30 min to achieve the adsorption equilibrium before starting the irradiation, and b) irradiation was started just after preparing the mixture that was kept under stirring. In both cases, a 100 mL Pyrex photochemical reactor with a 125 W high-pressure mercury lamp, operating between 180 and 420 nm with a peak at 366 nm, was used. The photon flux was measured by using a Delta OHM radiometer HD2302.0 leaned against the external wall of the photoreactor containing only pure water. After switching on the lamp, 2 mL aliquots of the aqueous suspension were collected from the reactor and filtered through a 0.45 μm PTFE Millipore disc to remove the catalyst powder.

A Shimadzu UV-2450 UV/V spectrometer was used to determine the dye concentration after calibration, by measuring the absorbance at 660 nm. Since the degradation pathway for the selected dye is known with high reliability [213], the eventual formation of byproducts was checked, monitoring the overall UV-vis spectrum of the solutions recovered at different times during the degradation experiments.

The rate constant *k* was calculated according to the following Equation (2.8):

$$ln\frac{C}{C_0} = -kt \qquad (2.8)$$

where *C* is concentration after time *t*, C_0 represents the initial concentration and *k* is the pseudo-first-order rate constant (min^{-1}), calculated from the slope (-*k*/2.303) of the MB concentration and time curve (log-linear scale) as follows (2.9):

$$k = 2.303 \times \text{slope} \qquad (2.9)$$

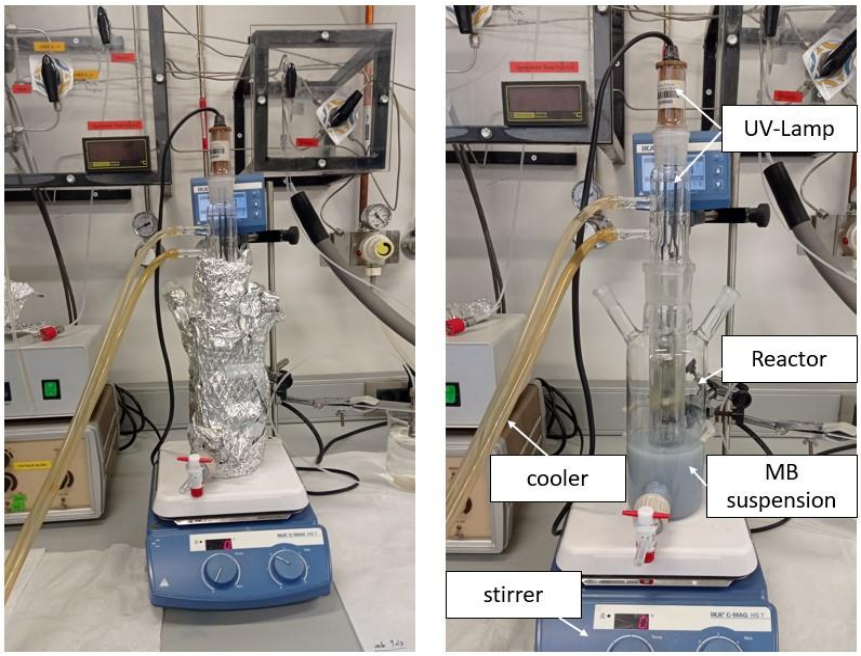

Figure 2.8. Photography of the experimental set up for methylene blue removal under UV irradiations

2.4.2 Malachite green removal

The removal of MG by adsorption or photocatalytic degradation was studied at two different temperature ranges. The first range, between 25 < T °C< 60, corresponds to experiments for which temperature inside the solar chamber increases due to radiation over time, and will be referred to as MT (from moderate temperature). The second set of experiments, in the temperature range 2< T °C< 25, were conducted using an ice bath to limit the temperature increase, and are referred to as LT (low temperature). All the tests were performed twice to double-check reproducibility.

2.4.2.1 Photodegradation test

Photodegradation of malachite green was performed using a 250 ml Pyrex glass vessel, containing a MGs olution of an initial concentration of 10 mg/Land 0.125 g of the photocatalyst under continuous stirring. The experimentswere conducted using an ATLAS SUNTEST CPS+ instrument with a xenon arc lamp (NXE 1500B) for simulated natural solar radiation as a source of UV-rays. Before irradiation, the suspension was sonicated for 2 min to well disperse the photocatalysts and, then, maintained in dark for 1 h to establish adsorption-desorption equilibrium. At specified time intervals, 4 ml of the solution were taken, filtered, and analyzed by UV-vis spectrophotometry (Shimadzu PC1201). Maximum

absorbance at 618 nm was used to follow MG degradation. Prior to the photodegradation experiments, a photolysis test was carried out to evaluate any auto-degradation of the MG solution without photocatalyst.

The rate constant *k* was calculated according to the following Equation (2.10):

$$ln\frac{C}{C_0} = -kt \qquad (2.10)$$

where *C* is concentration after time *t*, C_0 represents the initial concentration and *k* is the pseudo-first-order rate constant (min^{-1}), calculated from the slope (-*k*/2.303) of the MG concentration and time curve (log-linear scale) as follows:

$$k = 2.303 \times \text{slope} \qquad (2.11)$$

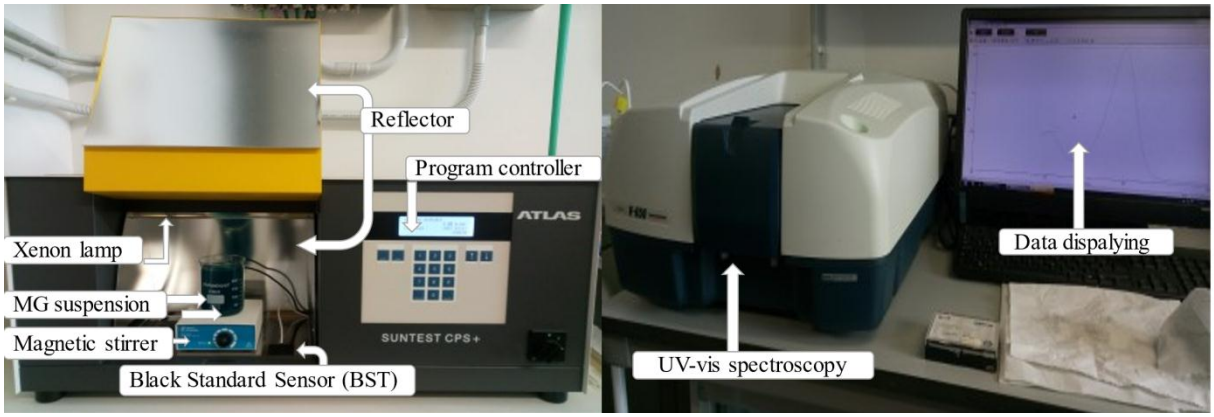

Figure 2.10. Photography of the experimental system for malachite green removal under simulated solar light irradiations (ATLAS SUNTEST CPS+ instrument)

2.4.2.2 Adsorption test

Adsorption tests were studied under dark, for which, in a Pyrex glass vessel, 250 ml of a malachite green solution with an initial concentration of 10 mg/l and 0.125 g of adsorbent were continuously stirred. At set time intervals, a filtrate of the solution is recovered and MG concentration was analyzed by UV-vis spectrophotometry (Shimadzu PC1201) Maximum absorbance at 618 nm was used to follow MG degradation.

The concentration of malachite green was assessed using a fit-linear calibration curve measured by UV-vis analysis (supplementary info. 1). It is expressed by the absorbance (A) versus concentration (C) of the MG solution, using the following model equation (2.12)

$$A = slope \times C + intercept \qquad (2.12)$$

From equation 10, and as the obtained plot is linear (intercept =0), the concentration of MG can be deduced as follows:

$$C = \frac{A}{slope} \qquad (2.13)$$

where C is MG concentration at each time interval expressed in (mg/L), A is the absorbance, and slope and intercept are extracted from the linear plot.

2.4.2.3 Malachite green photodegradation pathway

Various reactive species, such as $OH^{\bullet}$ radicals, positive holes (h^{+}), and superoxide anion radicals ($O_2^{\bullet}$) could participate in the degradation of organic compounds. To evaluate the contribution of the main reactive species and elucidate the photocatalytic mechanism involved in the MG degradation, the photodegradation behavior in the presence of different electron and hole scavengers was studied. Methanol, Benzoquinone, 2-propanol were used as a photogenerated positive hole (h^{+}), superoxide radicals (O^{-2}) and hydroxyl radicals ($OH^{\bullet}$) inhibitors respectively. 2 ml of the scavengers (0.2 mol/L) were added to 250 mL of malachite green solution (10 mg/L) during the photodegradation process under moderate temperature.

CHAPTER III

3 CHAPTER III: RESULTS AND DISCUSSIONS

3.1 ACTIVATED CARBONS AND THEIR CHARACTERIZATIONS

3.1.1 Ultimate analysis

The elemental composition (carbon, hydrogen, oxygen, nitrogen, and sulfur) of the Luffa Cylindrica fibers precursor and its derived activated carbons prepared at different activation temperatures and impregnation ratios are summarized in table 3.1. The results show a high amount of carbon content, and a moderate amount of oxygen, indicating that most of their surface functionality is attributed to oxygen groups whereas no sulphur has been detected[214]**.** Carbon content increases with the increase of the activation temperature up to 550 °C due to an increase in the degree of aromaticity[215], while further raising up to 700 °C results in a decrease due to the volatility of some carbonaceous compounds at high temperature as CO and CO_2. The nitrogen content is negligibly affected by the activation temperature and depends mostly on biomass feedstock. Nevertheless, the hydrogen and oxygen content decreases resulting in a diminution of the H/C and O/C atomic ratios. Fraction H/C is typically used to describe the degree of carbonization since H is mainly associated with the organic matter of the biomass, Whereas the O/C fraction describes the progression of the deoxygenation process. Since the activated carbons are naturally known as adsorbent materials, carbon content is commonly responsible for the adsorption properties of the activated carbons and higher O and H containing groups, mainly located at the external surface, provide binding sites to target substances [216].

The hydrophilicity of the LACs' surface could be inferred from O content that can reveal the possible presence of polar groups. Thus, due to the carbonization and the loss of polar functional groups at elevated temperatures, the surface of the activated carbon is more aromatic and less hydrophilic indicated by the decrease in the O/C fraction[216]. The analysis of the H/C ratio and fixed carbon content data showed that fixed carbon has a very low H content and also that volatile matter released during the activation step consisted of compounds with higher H/C ratios. These findings can promote Luffa cylindrica fibers to be a good precursor for producing activated carbon.

Table 3.1. Ultimate analysis of the produced Luffa activated carbons at different activation temperatures and impregnation ratios (wt.%)

Sample	Ultimate analysis						
	%N	%C	%H	%S	%O*	O/C×10^2	H/C×10^2
Raw Luffa	0.09	55.32	05.57	0	39.02	70.54	10.07
LAC1-500-1	0.12	61.62	01.57	0	28.18	40.42	2.25
LAC1-500-2	0.15	61.83	03.68	0	29.41	45.73	2.55
LAC1-550-1	0.13	64.62	03.47	0	27.04	47.57	5.95
LAC1-550-2	0.16	62.56	03.88	0	28.57	41.84	5.95
LAC1-700-1	0.17	61.20	03.35	0	26.17	42.76	5.47
LAC1-700-2	0.19	58.72	03.37	0	31.91	54.34	5.74
LAC3-500-1	0.31	79.29	02.15	0	18.25	23.02	2.71
LAC3-500-2	0.12	71.06	02.61	0	16.95	23.85	3.67
LAC3-550-1	0.07	85.93	01.68	0	12.32	14.34	1.96
LAC3-550-2	0.09	72.48	02.88	0	19.42	26.79	3.97
LAC3-700-1	0.15	69.35	01.82	0	20.78	29.96	2.62
LAC3-700-2	0.22	66.22	02.46	0	23.91	36.11	3.71
LAC5-500-1	0.09	53.30	04.46	0	42.15	79.08	8.37
LAC5-500-2	0.09	61.28	02.36	0	23.88	38.97	3.85
LAC5-550-1	0.09	66.81	02.58	0	21.82	32.66	3.86
LAC5-550-2	0.11	67.78	01.95	0	20.38	30.07	2.88
LAC5-700-1	0.15	61.54	02.90	0	27.43	44.57	4.71
LAC5-700-2	0.17	65.51	01.75	0	22.15	33.81	2.67

(*) by difference

3.1.2 Proximate analysis

The Proximate analysis results of the LACs prepared with different impregnation ratios and temperatures are presented in Table 3.2. The fixed carbon content in the activated carbons is higher as compared to raw luffa fibers. At the same time, the moisture, ash, and volatile matters are presented in lower contents, which is due to the effective

carbonization of the raw materials. Ash content represents the total amount of minerals remaining after the removal of water and the organic matter by heating. As shown in Table 3.2, the ash content of the obtained activated carbons increased with increasing activation temperatures as a result of the growing concentration of minerals and destructive volatilization of the lignocellulosic structure [217]. Furthermore, the high volatile matter and low ash content of the precursor, luffa cylindrica fibers can be a good starting material for the preparation of activated carbon [37]. Under the preparation conditions of 500 °C and for a 1 hour residence time, activated carbons prepared with H_3PO_4 to luffa mass ratios of 3 wt/wt.% has the highest fixed carbon content (80 %) followed by activated carbon obtained with H_3PO_4 to luffa mass ratios of 5 wt/wt.% (67 %) and with H_3PO_4 to luffa mass ratios of 1 wt/wt.% (59 %). The moisture, ash, and volatile content of the activated carbons (ratio 3 wt/wt.%) are lesser as compared to activated carbon (ratio 5 wt/wt.%) and activated carbon (ratio 1 wt/wt.%). For the same H_3PO_4 to luffa mass ratio and residence time of 1 hour, the carbon content increases with an increase in activation temperature. The same tendency is observed for all the adopted temperatures and impregnation ratios for 2 hours residence time, being the content slightly lower than that of residence time of 1 hour.

Table 3.2. Proximate analysis of the produced Luffa activated carbons at different activation temperatures and impregnation ratios (wt.%)

Samples	Proximate analysis %			
	Moisture	**Ash**	**Volatile content**	**Fixed carbon**
LAC1-500-1	3	6	12	59
LAC1-550-1	4	7	24	57
LAC1-700-1	6	8	27	45
LAC3-500-1	2	4	10	80
LAC3-550-1	3	5	23	79
LAC3-700-1	5	6	25	71
LAC5-500-1	4	7	24	67
LAC5-550-1	4	7	20	64
LAC5-700-1	6	8	25	61
LAC1-500-2	7	5	13	42
LAC1-550-2	7	6	26	46
LAC1-700-2	9	7	28	36
LAC3-500-2	6	6	26	56
LAC3-550-2	8	5	29	52
LAC3-700-2	9	8	27	46
LAC5-500-2	5	7	33	42
LAC5-550-2	8	6	30	46
LAC5-700-2	8	6	34	40

From heating the material from 25 to 150 °C, the first weight loss corresponds to the moisture elimination, while the second loss between 150-450 °Cis mainly due to volatile matters. To this extent, O and H were initially lost in the form of water and, further in the form of light hydrocarbons, carbon monoxide, and carbon dioxide corresponding to the decomposition of hemicelluloses (180-270 °C) and celluloses (270-400 °C)[216]. In the range 400-550 °C, the decomposition of a more stabilized structure takes place. Being the decomposition of lignin more difficult, it occurs slowly from 200 up to 900 °C. These results can also be confirmed from the DTG curves. Above 550, a change in the slope of the weight-loss curve (see Figure3.1 and, supplementary information2.a-2.h) can be also observed, possibly associated to volatilization of carbon-oxygen complexes engendered by the activation process, and to a lesser extent, to the decomposition of phosphorous-compounds (as P_2O_5), produced by the reaction of phosphoric acid with the carbon matrix indicating that the basic structure of the activated carbon has been formed [218–220].

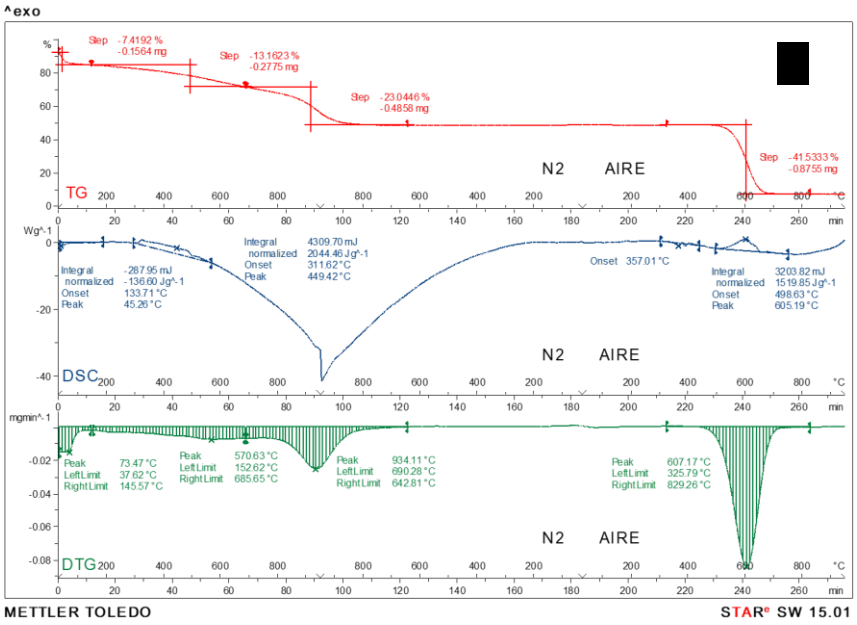
^exo
Step -7.4192 %
-0.1564 mg
Step -13.1623 %
-0.2775 mg
Step -23.0446 %
-0.4858 mg
Step -41.5333 %
-0.8755 mg
N2 AIRE
TG
Wg^-1
Integral -287.95 mJ
normalized -136.60 Jg^-1
Onset 133.71 °C
Peak 45.26 °C
Integral 4309.70 mJ
normalized 2044.46 Jg^-1
Onset 311.62 °C
Peak 449.42 °C
Onset 357.01 °C
Integral 3203.82 mJ
normalized 1519.85 Jg^-1
Onset 498.63 °C
Peak 605.19 °C
N2 AIRE
DSC
mgmin^-1
Peak 73.47 °C
LeftLimit 37.62 °C
RightLimit 145.57 °C
Peak 570.63 °C
LeftLimit 152.62 °C
RightLimit 685.65 °C
Peak 934.11 °C
LeftLimit 690.28 °C
RightLimit 642.81 °C
Peak 607.17 °C
LeftLimit 325.79 °C
RightLimit 829.26 °C
N2 AIRE
DTG
METTLER TOLEDO
STAR° SW 15.01

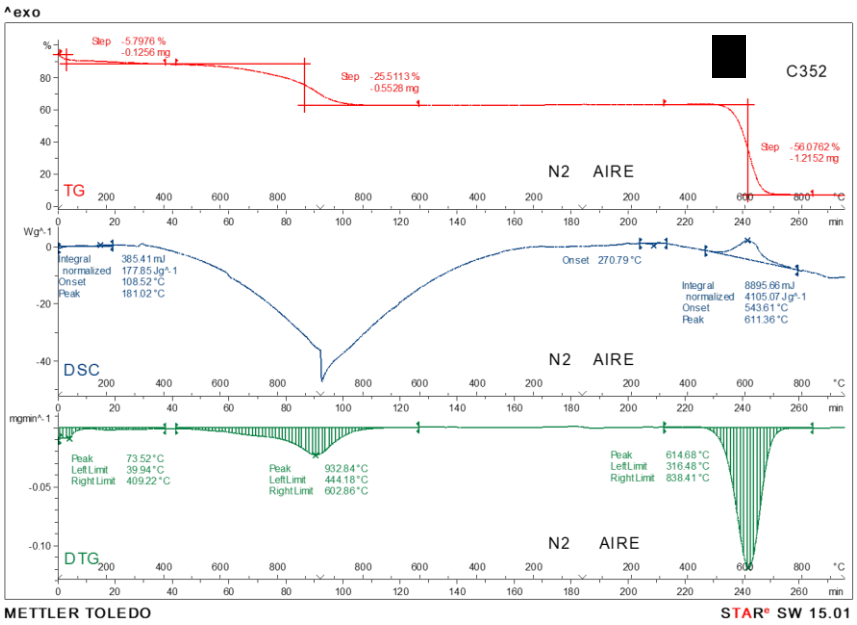
^exo
Step -5.7976 %
-0.1256 mg
Step -25.5113 %
-0.5528 mg
Step -56.0762 %
-1.2152 mg
C352
N2 AIRE
TG
Wg^-1
Integral 385.41 mJ
normalized 177.85 Jg^-1
Onset 108.52 °C
Peak 181.02 °C
Onset 270.79 °C
Integral 8895.66 mJ
normalized 4105.07 Jg^-1
Onset 543.61 °C
Peak 611.36 °C
N2 AIRE
DSC
mgmin^-1
Peak 73.52 °C
LeftLimit 39.94 °C
RightLimit 409.22 °C
Peak 932.84 °C
LeftLimit 444.18 °C
RightLimit 602.86 °C
Peak 614.68 °C
LeftLimit 316.48 °C
RightLimit 838.41 °C
N2 AIRE
DTG
METTLER TOLEDO
STAR° SW 15.01

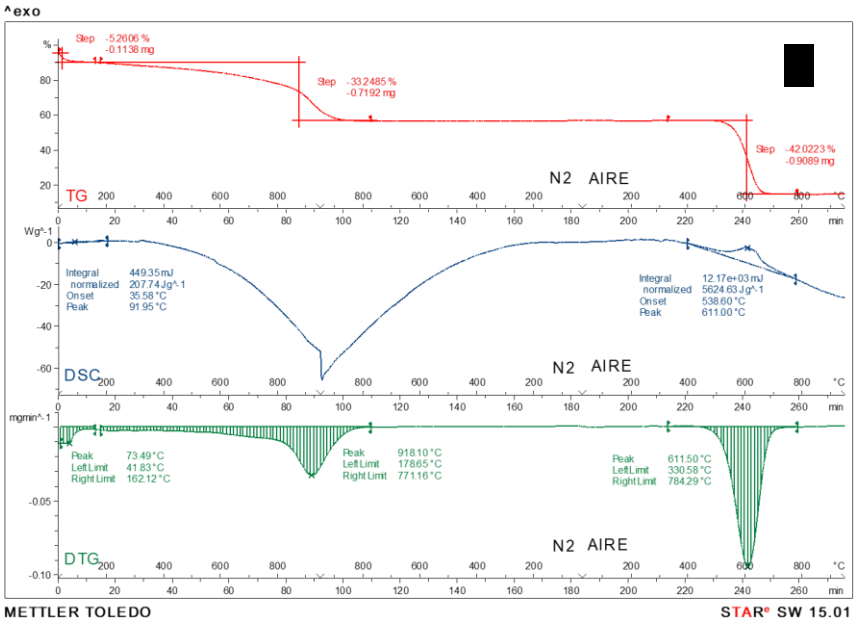

Figure 3.1: TG (red), DSC (blue), and DTG (green) curves of luffa activated carbons samples prepared with different ratios 1, 3 and 5 at 500°C for 2 hours residence time with: (a) LAC1-500-2, (b) LAC3-500-2, and (c) LAC5-500-2.

3.1.3 Morphology and microstructure properties

Figure 3.2 illustrates SEM images of raw Luffa and LACs samples. Figures 3.2(a) and 3.2(b) shows that raw luffa presents a homogeneous appearance, with a rich layer of external lignin around the fibers, as already demonstrated in previous works [218]. Also, the sponge is slightly fibrous with irregular structure and certain cracks and holes. Figures from 3.2(c) to 3.2(k) show the typical morphology of activated carbon [221]. During the carbonization step of Luffa Cylindrica, volatile compounds evaporate leading to the evacuation of new pores and cavities. Phosphoric acid as an activating agent played a major role in developing the porous structure of the activated carbon. It promoted bond cleavage reactions and the formation of crosslinks via processes such as cyclization, and condensation[222]. It also allows the addition or insertion of phosphate groups that drives a process of dilation that, after removal of the acid, leaves the matrix in an expanded state with a well-developed and accessible pore structure [222].The porosity is then developed, and more pores are created due to the activation step with phosphoric acid.

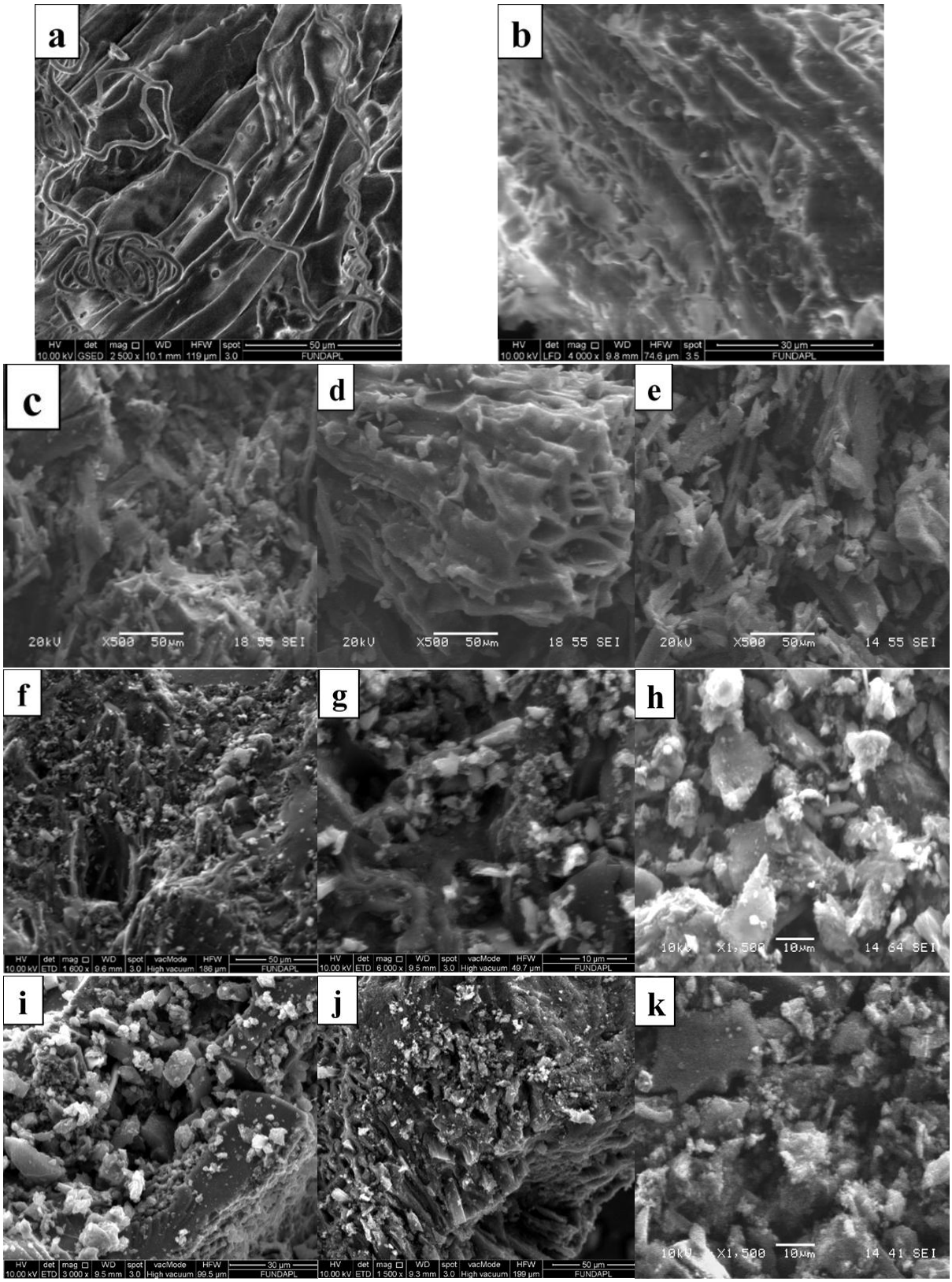

Figure 3.2: Scanning Electron Microscopy images for raw luffa fibers (a, b) and luffa activated carbons prepared with 1, 3, and 5 wt/wt. % impregnation ratios at different temperatures (500, 550, and 700°C) residing for 1 hour with (c) LAC1-500-1, (d) LAC1-550-1, (e) LAC1-700-1, (f) LAC3-500-1, (g) LAC3-550-1, (h) LAC3-700-1, (i) LAC5-500-1, (j) LAC5-550-1, and (k) LAC5-700-1

Furthermore, it seems that an appropriate carbonization temperature could significantly enhance the growth of the porosity and surface area of the activated carbons, while an excessive raise has an opposite effect on the surface area. All the optimized parameters used to produce Luffa activated carbons resulted in porous activated carbons with different accessible and developed pores better than the raw Luffa fibers.

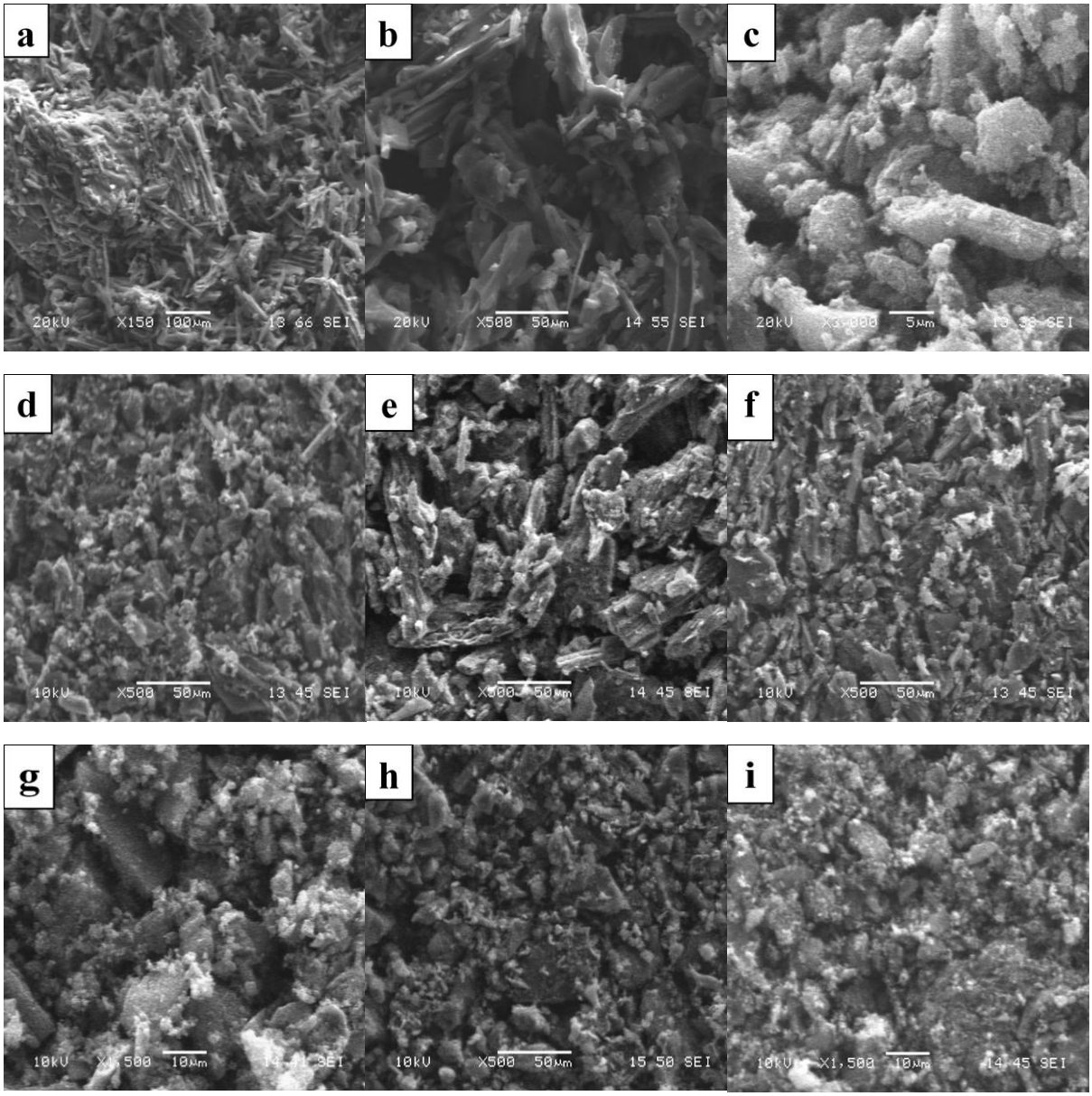

Figure 3.3: Scanning Electron Microscopy images for luffa activated carbons prepared with 1, 3, and 5 wt/wt. % impregnation ratios at different temperatures (500, 550, and 700°C) residing for 2 hours with (a) LAC1-500-2, (b) LAC1-550-2, (c) LAC1-700-2, (d) LAC3-500-2, (e) LAC3-550-2, (f) LAC3-700-2, (g) LAC5-500-2, (h) LAC5-550-2, and (i) LAC5-700-2

3.1.4 Textural properties

Physisorption analysis using the BET model was conducted to unveil the specific surface estimation of the activated carbons, including pore size distribution, and porosity. For ultra-micropores determination, CO_2 adsorption isotherms were applied. Figures 3.4 and 3.5 shows the N_2 adsorption-desorption isotherms of the luffa-activated carbons prepared with chemical activation by phosphoric acid. The adsorption isotherms are of type I and IV according to the IUPAC classification [43]. The samples prepared at different temperatures with H_3PO_4 to luffa mass ratios of 3 and 5 are all of type IV adsorption isotherms with H1 hysteresis loops, indicative of a mesoporous structure.

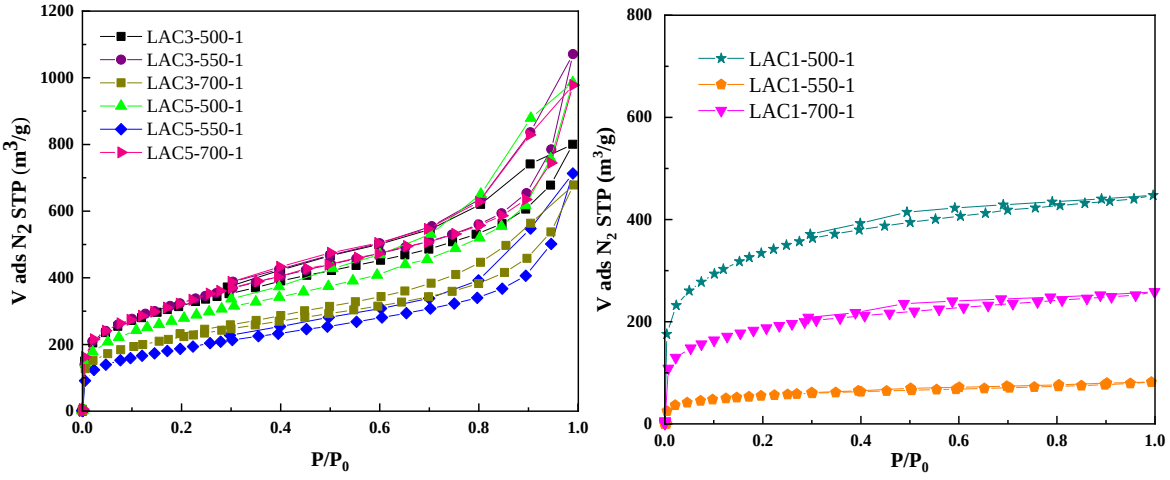

Figure.3.4: N_2 adsorption-desorption isotherms at -196°C of the prepared *Luffa* activated carbons with $H_3PO_4$to luffa mass ratios of 1, 3, and 5 wt/wt. % at different temperatures (500, 550, and 700°C) and 1 hour residence time.

The H_3PO_4 to luffa mass ratio of 1 resulted in samples with adsorption isotherms of reversible type I corresponding to a well-developed microporous structure with a significant contribution of mesoporosity, which depends on both the impregnation ratio and the activation temperature. The isotherm is concave to the P/P_0 axis and the amount adsorbed approaches a limiting uptake governed by the accessible micropore volume [33]. A steep uptake at very low P/P_0 is due to enhanced adsorbent-adsorptive interactions in narrow micropores (see $V_{DR}CO_2$; Table 3.3) resulting in micropore filling at very low P/P_0 characterized by a pore size distributions over a broader range including wider micropores and possibly narrow mesopores (<~ 2.5 nm) [196].

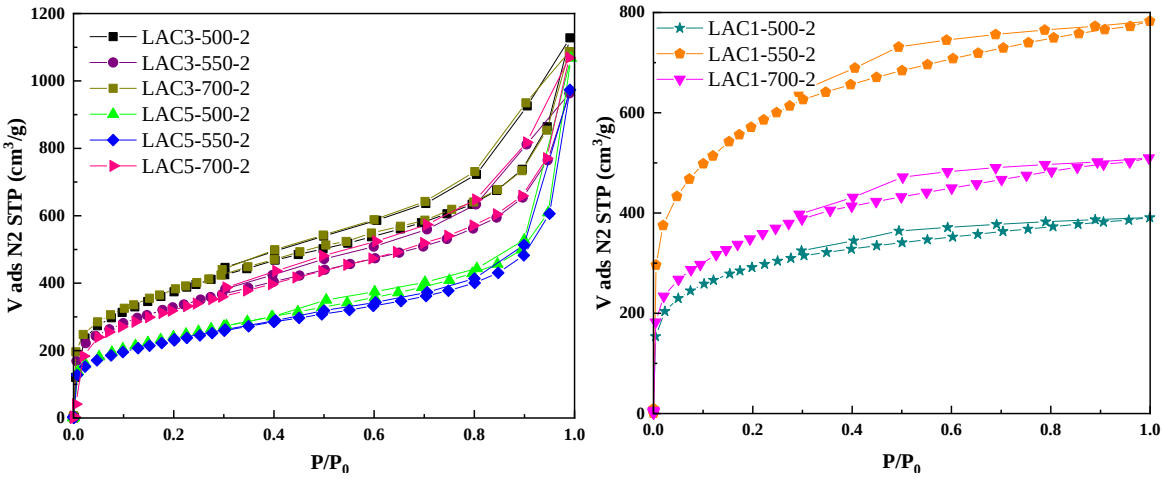

Figure.3.5: N_2 adsorption-desorption isotherms at -196°C of the prepared *Luffa activated* carbons with $H_3PO_4$to luffa mass ratios of 1, 3, and 5 wt/wt. % at different temperatures (500, 550, and 700°C) and 2 hours residence time.

Table 3.3 illustrates the calculated apparent BET surface area, the total micropore volume ($V_{DR}N_2$), an estimation of the mesopore volumes from the N_2 adsorption isotherms (V_{MESO}), the narrow micropore volume ($V_{DR}CO_2$), and the total pore volume (V_{Total}). Given the data in Table 3.1, an important surface area has been developed for all the activated carbons obtained under the different preparation conditions. In addition, according to $V_{DR}N_2$, the developed porosity of the resulting LACs is an important mixture of a micro and mesoporous network system whereas the $V_{DR}CO_2$measured withCO_2 indicates the presence of slightly narrow microporosity in this material [223]**.** Although the difference in the porous volume, the BET surface areas of all the samples were very high, nearly reaching up 1400 m²/g and the porous volume follows an exponential raise with the development of the BET surface area (Figure 3.6)

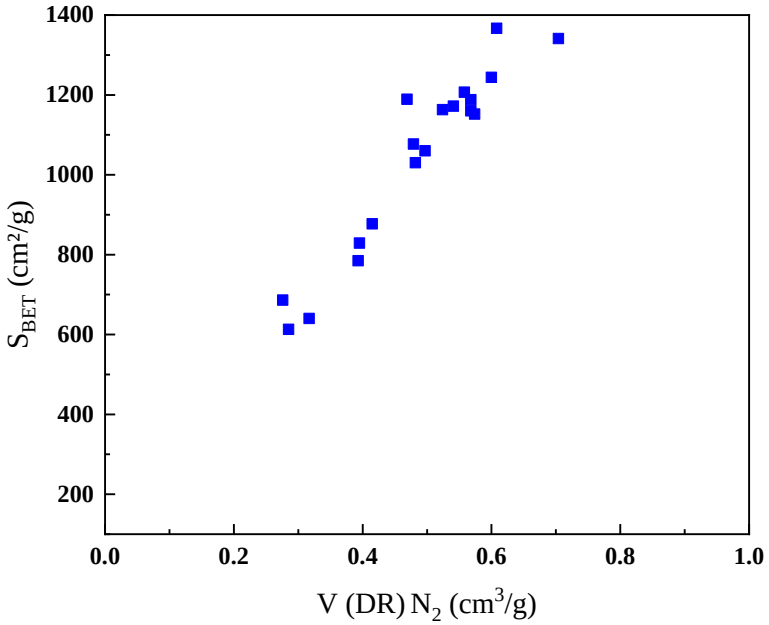

Figure 3.6: S_{BET} values versus total micropore volumes of the prepared *Luffa* activated carbons with impregnation ratios 1, 3, and 5 wt/wt. % at different temperatures and residence times of 1 and 2 hours.

Table 3.3. Textural parameters for the prepared luffa activated carbons (LACs) obtained by N_2 adsorption-desorption at −196 ◦C and CO_2 adsorption at 0° C.

Luffa activated carbons (LACs)	**S_{BET} (m^2/g)**	**V_{DR} (N_2) (cm^3/g)**	**V meso (cm^3/g)**	**$V_{DR}(CO_2)$ (cm^3/g)**	**V_{tot} (cm^3/g)**
Raw Luffa	1.513	0.007	0.001		0.008
LAC1-500-1	1060	0.515	0.01	0.282	0.629
LAC1-500-2	1152	0.453	0.01	0.270	0.985
LAC1-550-1	1091	0.085	0.01	0.042	1.268
LAC1-550-2	993	0.176	0.01	0.146	1.508
LAC1-700-1	640	0.570	0.01	0.176	0.797
LAC1-700-2	1244	0.524	0.01	0.319	1.113
LAC3-500-1	1139	0.485	0.07	0.207	1.238
LAC3-500-2	1371	0.580	0.1	0.224	1.345
LAC3-550-1	1188	0.497	0.08	0.228	1.490
LAC3-550-2	1207	0.487	0.07	0.294	1.298
LAC3-700-1	1189	0.486	0.06	0.176	1.513
LAC3-700-2	1368	0.567	0.04	0.233	1.681
LAC5-500-1	1030	0.424	0.63	0.168	1.525
LAC5-500-2	1077	0.363	0.01	0.193	1.537
LAC5-550-1	686	0.276	0.09	0.162	1.103
LAC5-550-2	1160	0.347	0.08	0.228	1.658
LAC5-700-1	790	0.336	0.06	0.194	1.049
LAC5-700-2	1163	0.524	0.02	0.568	1.153

Figure 3.7 represents the pore size distribution of the LACs determined by applying the two-dimensional non-local density functional theory (2D)-NLDFT for a heterogeneous surface to the nitrogen adsorption data [202]. It can be revealed that samples prepared with

H_3PO_4 to luffa mass ratio of 1 wt/wt.% at different temperatures for 1 and 2 hours residence time present a complex mixture of micro and macroporous structure [224]. On the other hand, samples prepared using H_3PO_4 to luffa mass ratios of 3 and 5 wt/wt.% showed a mesoporous network, with an average pore width of between 2-5 nm. This is in good agreement with the chemical activation effect of phosphoric acid, which expands microporous to mesoporous structures. As a result, it can be depicted that for a desired microporous structure and narrowed pores, the ratio 1 is more suitable. As ratios 3 and 5 are favored for a mesoporous network.

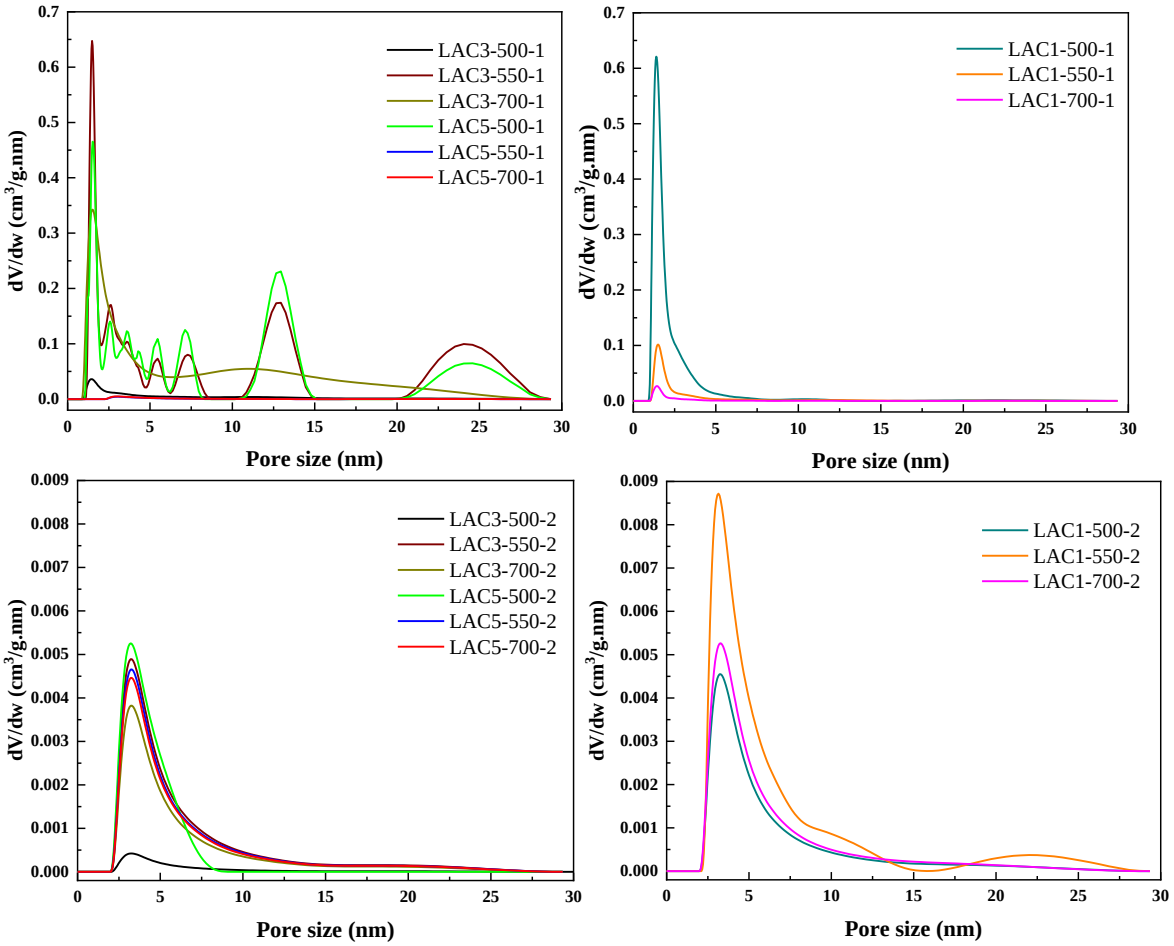

Figure 3.7: Pore size distribution of the prepared *Luffa* activated carbons with impregnation ratios of 1, 3, and 5 wt/wt. % at different temperatures

3.1.5 Effect of the preparation conditions on the specific surface area of LACs samples

The preparation conditions as temperature, activating agent, impregnation ratio, residence time, and even the precursor play a major role in determining the properties and the quality of the produced activated carbon.

3.1.5.1 Effect of temperature

As shown in Figure 3.8, and for one hour heating time, a moderate increase in the activation temperature from 500 to 550 °C significantly increased the surface area and resulted in both micro-mesopores developments (see Table 3.3) for samples prepared with an impregnation ratio of 1 and 3. This may be due to the formation of new pores with the incessant evaporation of the agents resulting from the decomposition of primary compounds of the luffa fibers with increasing temperature. However, the specific surface area decreases with a further increase of temperature (700 °C), which can be attributed to the narrowing effect of the pores or of opening the mesoporosity to macroporosity. Moreover, when the temperature increases, phosphate linkages, such as phosphate and polyphosphate bridges, that connect biopolymer fragments are formed through the combination of phosphoric acid with organic species. Thus, partially hindering the contraction that results in broader porous structures in the activated carbons. Above 550 °C, these bridges become thermally unstable thus their loss produces a contraction in the material, which will result in a decrease in porosity [52,225]. From this point of view, maintaining the activation temperature at around 500 °C leads to better development of the material porosity. Thus, this temperature is considered suitable to obtain optimal properties of the activated carbons as reported by many researchers [89,130,223,226].

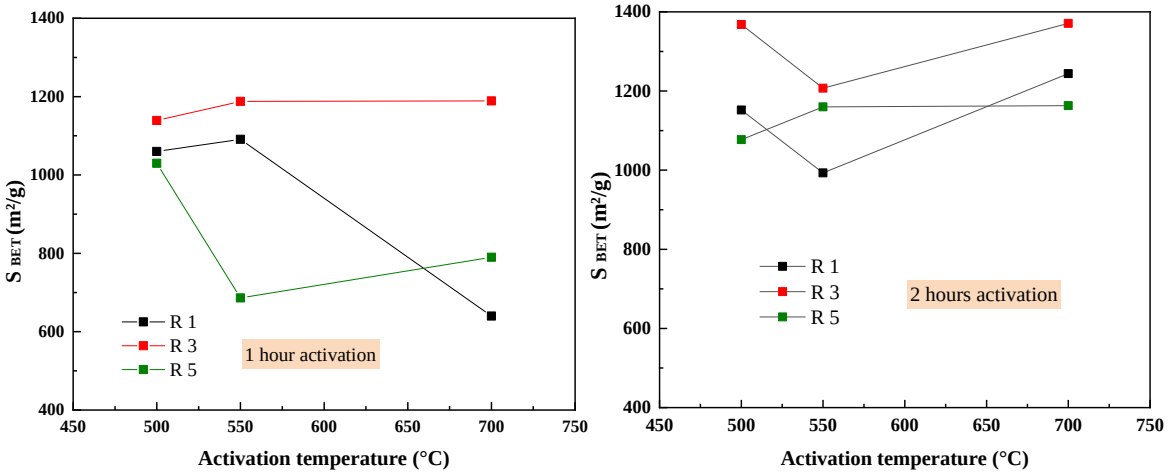

Figure 3.8: Effect of the activation temperature on the specific surface area of the LACs prepared at different impregnation ratios.

On another hand, the specific surface area of the LACs samples prepared with H_3PO_4 to luffa mass ratios of 5 decreased with increasing the temperature to 550°C and then increased when the temperature reached 700°C. In addition to that, and for 2 hours of residence time, the effect on the BET surface area was reversed for this series of samples

compared to those prepared for 1 hour residence time. This is because a longer heating duration led some of the pores to become larger or even collapse, thus contributing to the reduction of the surface area [220].

3.1.5.2 Effect of Impregnation ratio

The impregnation ratio has been identified as one of the most important factors in the chemical activation process of the activated carbons being responsible for the development of its porous texture. The increase of H_3PO_4 to luffa mass ratio from 1 to 3 results in a higher development of the porous structure of the activated carbons, with a significant increase of the surface area and mesoporous volume (see Table 3.2). The growth in porosity was attributed to the release of tars from the cross-linked framework generated by the treatment of phosphoric acid [74,220].

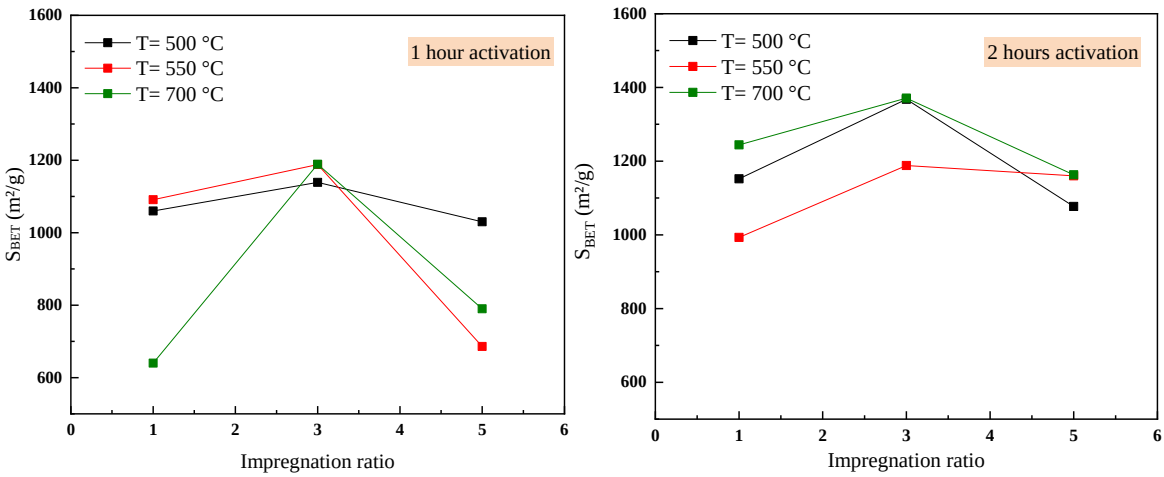

Figure 3.9: Effect of the impregnation ratios on the specific surface area of the LACs prepared at different activating temperatures.

In fact, porosity is generated with phosphoric acid intercalated in the internal structure of the biopolymer material in the form of phosphate and polyphosphate compounds. As the amount of H_3PO_4 used increases, the volume filled by it and various polyphosphates will increase, resulting in a larger porous volume and pore size [227]**.** However, an excess of the amount of the activation agent during the preparation process (in this case 5 times higher than the amount of the precursor) could lead to the destruction of the porosity and thus a decrease in the surface area as illustrated in Figure 3.9.

3.1.5.3 Effect of activating agent

H_3PO_4 acts as a chemical activating agent and plays a major role in developing the porous structure of the activated carbon. It promotes bond cleavage reactions and the

formation of crosslinks via processes such as cyclization, and condensation [76]**.** Once the phosphoric acid is introduced into the carbonaceous matrix of the precursor, it leads to the hydrolysis of the lignocellulosic material with subsequent partial extraction of some components, thus weakening the particle which swells. It also allows the addition or insertion of phosphate groups that drives a process of dilation that, after removal of the acid, leaves the matrix in an expanded state with a well-developed and accessible pore structure [46]**.** Furthermore, by using the H_3PO_4, carbons with highly thermally stable phosphorus surface complexes in the forms of $C{-}O{-}PO_3$ and $C{-}PO_3$ are produced. These P groups confer the carbon with high oxidation resistance, surface acidity, and redox sites which improves activated carbon potential for applications in catalysis [228].

Finally, as reported by Molina-Sabio et al. [229], there is a relation between the volume of micropores and the volume occupied by the acid phase existing at the carbonization temperature. Thus, an extensive washing step to eliminate the polyphosphates entrapped after the carbonization in the final product produces an important porosity.

3.2 METHYLENE BLUE REMOVAL BY ADSORPTION ANDPHOTOCATALYTIC DEGRADATION

3.2.1 Characterization of the hybrid materials

3.2.1.1 Textural properties

Figure 3.10a represents adsorption-desorption isotherms of N_2 at -196 °C of the TiLACx/y samples. According to the IUPAC classification, all the isotherms are type IV with H1 hysteresis loops, indicative of a mesoporous structure [43].

The pore size distribution of the samples depicted in Figure 1b was determined by applying the two-dimensional non-local density functional theory (2D)-NLDFT for a heterogeneous surface to the nitrogen adsorption data. It points out that all samples present a mesoporous structure with an average pore width of 2-5 nm. This is in good agreement with chemical activation by phosphoric acid, which develops microporous to mesoporous structures [230].

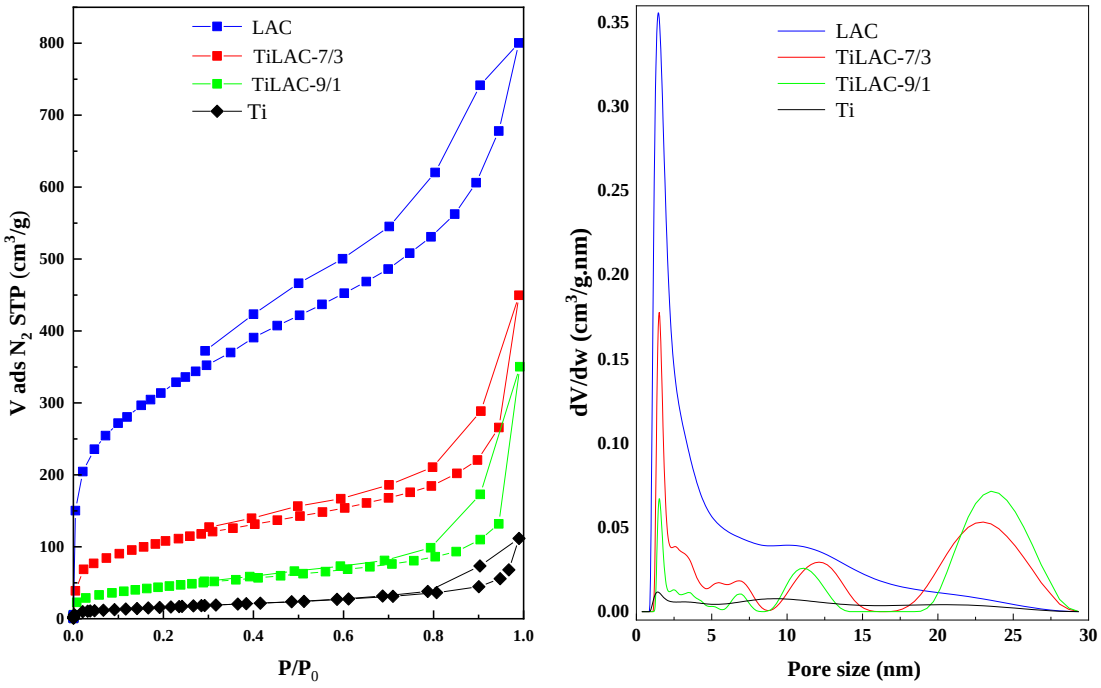

(**1.a**) (**1.b**)

Figure 3.10. (1a) Adsorption-desorption isotherms of N_2 at -196 ºC and (1b) pore size distribution of the prepared luffa activated carbon and TiLAC composites.

Table 3.4 compiles the calculated apparent BET surface area, the total micropore volume ($V_{DR}N_2$), an estimation of the mesopore volumes from the N_2 adsorption isotherms (V_{MESO}), the narrow micropore volume ($V_{DR}CO_2$), and the total pore volume (V_{Total}). According to Table 1, the composite materials present textural properties in agreement with their components proportion. Although their surface area and porosity are lower than those of LAC, they are noticeably higher than those of the commercial benchmark, P25. In addition to the developed volume of mesopores, the samples also have a perceptible micropore structure [231].

Table 3.4. Textural parameters for P25 TiO_2, the prepared luffa activated carbon (LAC) and TiLAC composites, obtained by N_2 adsorption-desorption at -196 ºC and CO_2 adsorption at 0 °C

Sample	S_{BET} ($m^2\ g^{-1}$)	$V_{DR}\ N_2$ ($cm^3\ g^{-1}$)	V_{MESO} ($cm^3\ g^{-1}$)	$V_{DR}\ CO_2$ ($cm^3\ g^{-1}$)	V_{Total} ($cm^3\ g^{-1}$)
Ti (P25)	60	0.02	0.08	0.02	0.10
LAC	1172	0.54	0.64	0.21	1.18
TiLAC-7/3	378	0.16	0.28	0.07	0.43
TiLAC-9/1	161	0.07	0.20	0.03	0.27

3.2.1.2 SEM analysis

Figure 3.11 shows SEM images obtained for TiLACx-y composites. Figures 3.11(a) and 3.11(c) display SEM micrographs for the two prepared composites, from which it can be noticed that both phases are in close contact and TiO_2 is highly dispersed, covering most of the activated carbon surface homogenously. The dispersion of titania particles over the activated carbon is well observed through mapping images obtained by EDS analysis (Figure 3.11(b) and 3.11(d). Note that the blue areas are assigned to Ti particles, while the red and green parts correspond to carbon and oxygen. Furthermore, no agglomeration of Ti particles on the LAC surface was observed.

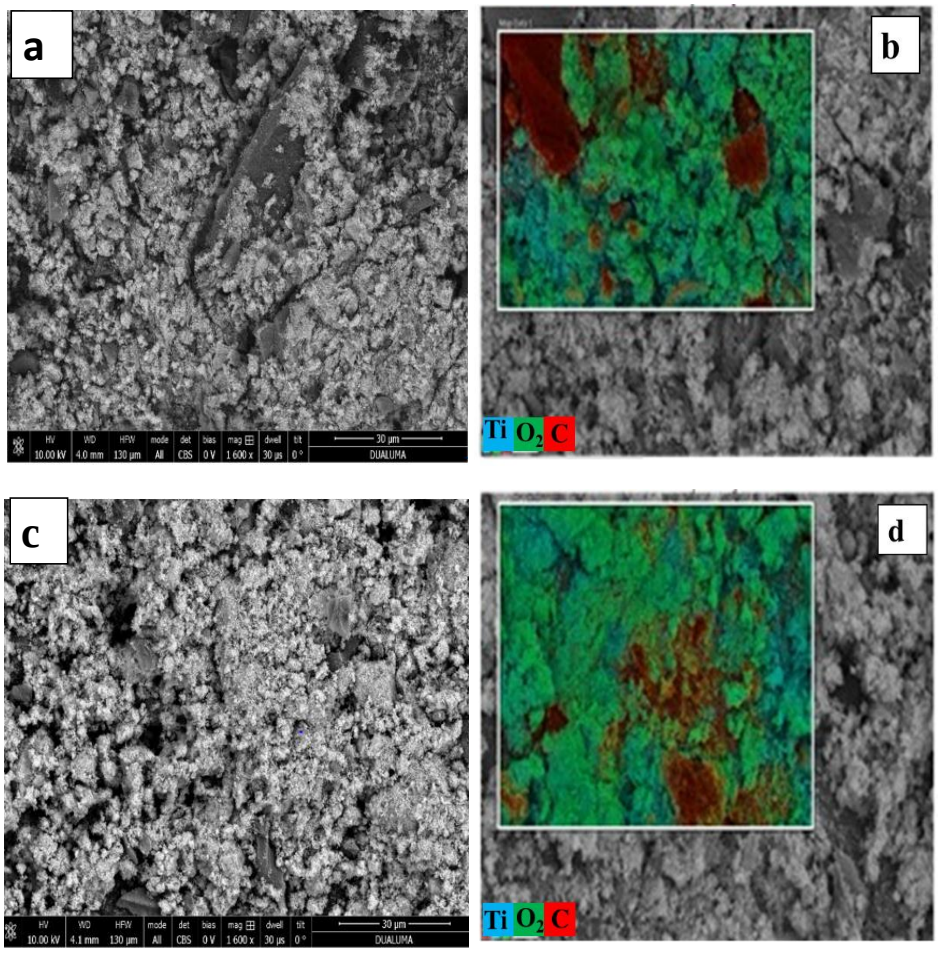

Figure 3.11. Scanning Electron Microscopy (a,c) and mapping images by EDS analysis (b,d) for TiLAC-7/3 and TiLAC-9/1 respectively (with high vacuum mode (pressure range 10^{-2}-10^{-4} Pa), imaging resolution of 1.0 nm for 'a' and 'c' at 10 kV, mode secondary electron image SE, integrated monochromator (UC) and beam deceleration mode. ETD detectors).

3.2.1.3 XRD patterns

Figure 3.12 displays XRD diffractograms for pure and composite samples. The XRD pattern of the LAC sample is characteristic of an amorphous activated carbon [231]**.** Considering the activation temperature (500°C), graphite formation is not expected. Regarding P25, as expected, the characteristic peaks associated to anatase and rutile are observed ((anatase (*) at 2θ = 25.4° (110), 38.1° (004), 48.2° (200), 54.3° (105), 55.3° (211) and 63.1° (204) and rutile (•) at 2θ = 27.2° (110), 35.8° (101) and 40.9° (111)). For the composite materials, the XRD patterns are similar to that of P25 TiO_2, indicating that the incorporation of LAC did not affect the crystallinity of titania.

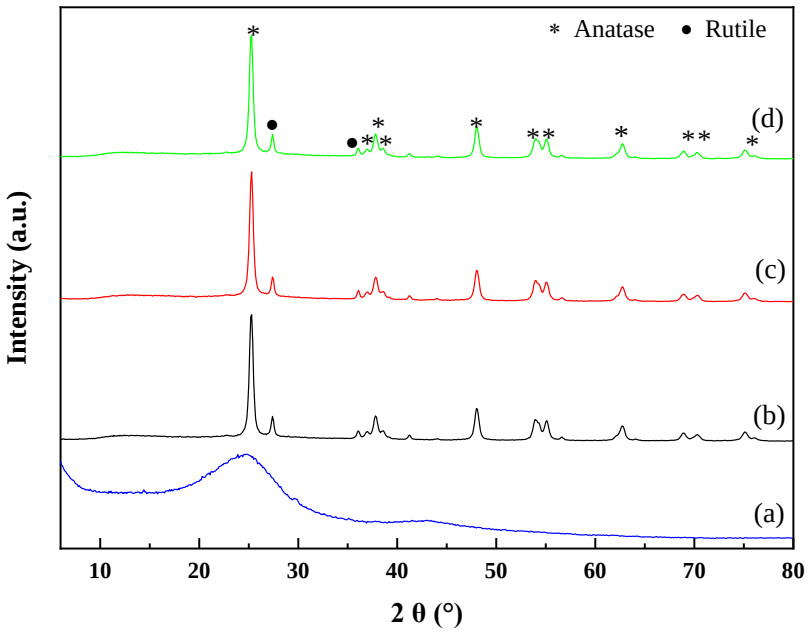

Figure 3.12. X-ray Diffractograms of: (a) LAC, (b) Ti, (c) TiLAC-7/3 and (d) TiLAC-9/1

3.2.1.4 X-ray Photoelectron spectroscopy

XPS measurements were carried out to study the superficial chemical composition of the samples. Figure 3.13 (a) shows C 1*s* spectra for LAC and composite samples.

Considering C 1*s* signal, Ti and LAC samples show three contributions at ca. 284.8, 286.5, 288.5 eV. The main contribution is located at 284.8 eV and assigned to C-C bonds in graphitic carbon and also from the adventitious carbon contamination layer. The other two contributions are due to alcoholic (C-O-H) and carbonyl C=O groups, respectively [232]. Moreover, the LAC sample shows another small contribution at 289.1 eV associated to ester (O-C=O) and CO_3^{2-} groups.

In the case of samples containing both titania and LAC, a new contribution at ca. 283.7 eV appeared. This new contribution is due to the presence of two phases with different conductivity, that is LAC and titania, and is also due to adventitious carbon.

Table 3.5. BE values corresponding to C 1s and O 1s signals (the relative contribution, in %, for the oxygen deconvoluted peaks appears in brackets).

	BE (eV) C 1s signal					**BE (eV) O 1s signal**		
LAC		284.8	286.2	288.2	290.0		531.6 (33.2)	533.4 (66.8)
TiLAC-7/3	283.6	284.8	286.7	288.9		529.7 (82.3)	531.2 (14.0)	532.9 (3.7)
TiLAC-9/1	283.6	284.8	286.5	288.5		529.7 (85.0)	531.2 (12.3)	532.8 (2.7)
Ti		284.9	286.6	288.7		529.7 (57.1)	532.0 (42.9)	

Ti 2*p* core-level spectra for all samples presented two contributions associated with the doublet Ti $2p_{1/2}$ y Ti $2p_{3/2}$, being the latter the most noticeable one at ca. 458.8 eV, which corroborates the presence of Ti^{4+} octahedrally coordinated (see Figure 3.13.b) [14].

Concerning the O 1*s* core-level spectra (Figure 3.13.c), differences between pure samples and composites become more evident. Table 2 includes the corresponding binding energy values. LAC signal presents a major contribution at 533.6 eV, which can be associated with organic C-O bonds in phenolic groups. Also, a second contribution at lower binding energy, ca. 531.5 eV is present, attributable to carboxylate species. On the other hand, in the pure P25 sample, two signals are observed, associated with oxygen in the lattice of TiO_2 (529.3 eV) and a second one at 532.1 eV, assigned to surface Ti-O-H groups. In the case of composites, signals associated to lattice oxygen in TiO_2 and LAC are present.

Due to the low presence of phosphorus on the surface, P 2*p* spectra are quite noisy (Figure 3.13.d). Nonetheless, a contribution located at 133.6 eV associated to pentavalent tetra-coordinated phosphorus (PO_4) as in phosphate and/or polyphosphate compounds as C-O-PO_3, is noticeable, which suggests that P atom is bonded to four oxygen atoms by one double bond and three single bonds, indicating that the P atom in Luffa activated carbon (LAC) is mainly present on the carbon surface by bonding to O atoms resulting from the phosphoric acid (polyphosphate) remaining after the washing step [228,233,234].

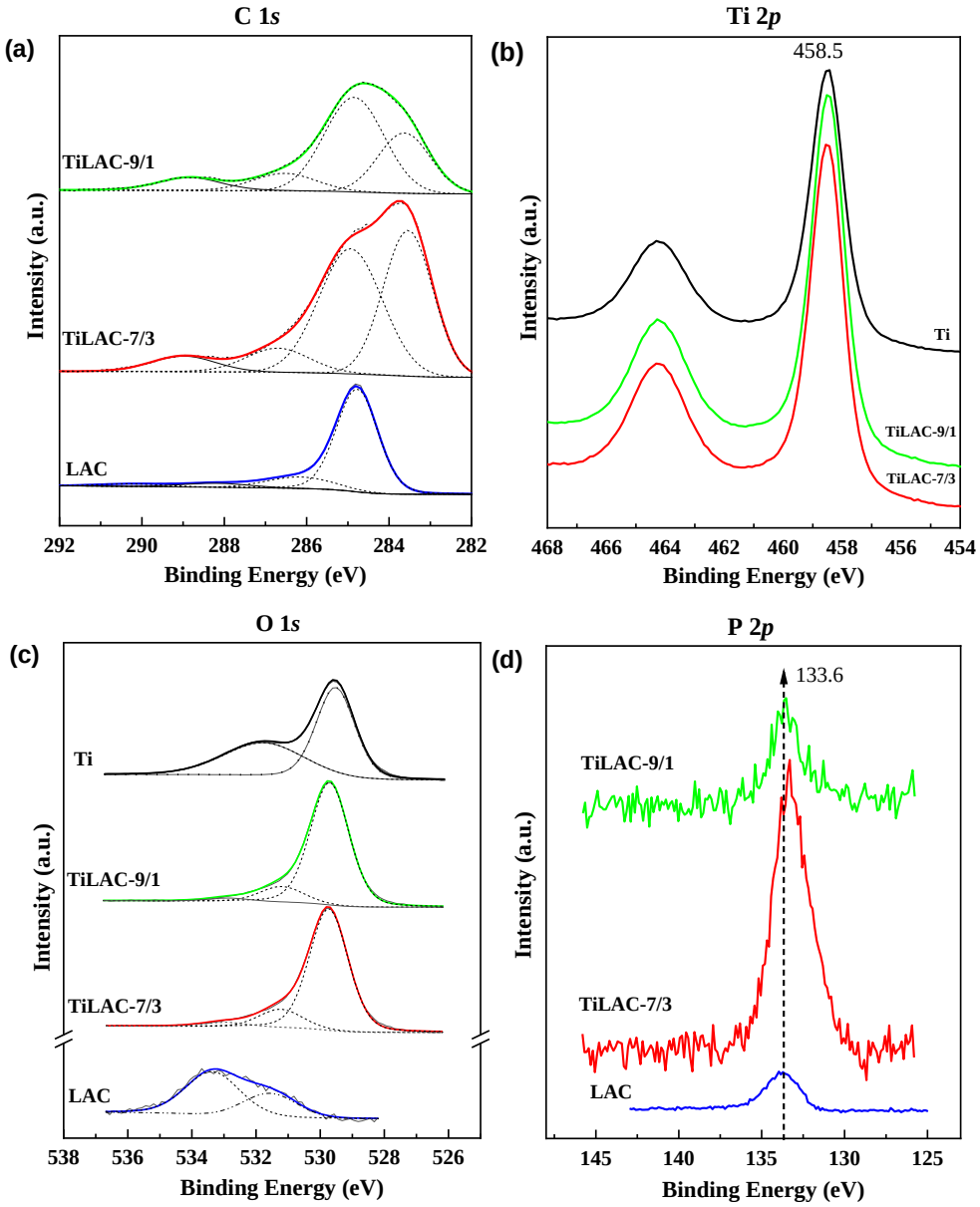

Figure 3.13. Core level spectra for all samples of (a) C 1*s*, (b) Ti 2*p*, (c) O 1*s* and (d) P 2*p*

The atomic surface composition obtained from XPS spectra is displayed in Table 3.6. It can be seen that the atomic composition depends on the content of each material in the sample. A small content of phosphorus has been detected for TiLAC, which can be associated to some traces left behind during the preparation of the LAC activated carbon.

Table 3.6. Atomic surface composition in (%) from XPS spectra

	C (%)	**O (%)**	**P (%)**	**Ti (%)**
LAC	93.25	6.13	0.62	
TiLAC-7/3	38.80	43.02	0.93	17.26
TiLAC-9/1	26.92	51.34	0.37	21.36

3.2.1.5 FTIR spectra analysis

FTIR spectra obtained for P25 and the two TiLAC composites are presented in Figure 3.14. A medium sharp peak at around 3700 cm^{-1} can be ascribed to the stretching vibration of the O-H bond. The absorption bond of water molecules adsorbed from the environment appeared at 1680 cm^{-1} [86].Two bands at the range 2200-2300 are associated to the carbon dioxide vibration band and medium C=C=C stretching band. A strong absorption peak is observed around 850-1200 cm^{-1} and is attributed to the Ti-O-Ti bond [235].The wavelength is slightly shifted to a lower wavenumber after the addition of LAC, indicating that the mass of this molecule is reduced, being the frequency of vibration inversely proportional to the mass of a vibrating molecule [236].

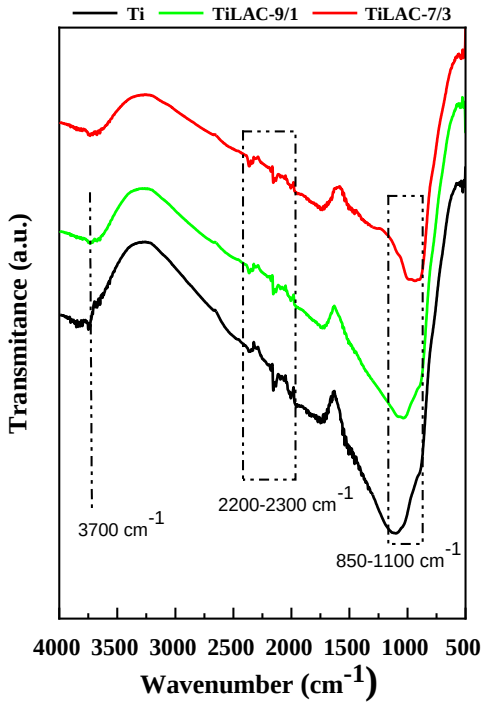

Figure 3.14. FTIR spectra for Ti, TiLAC-7/3, and TiLAC-9/1 samples.

3.2.1.6 UV-vis diffuse reflectance spectroscopy

The photoresponse of the samples was evaluated by UV-vis diffuse reflectance spectroscopy. The DRUV-Vis spectra and Kubelka-Munk function plots of samples Ti, TiLAC-7/3, and TiLAC-9/1 are displayed in Figure 3.15. Sample Ti had the lowest absorption in the UV region (< 400 nm), while the absorption curves of TiLAC samples presented higher absorption in this region, associated with the intrinsic absorption of TiO_2.

The presence of activated carbon in the composites strongly affects light absorption, explaining the high intensity of the absorption behavior of these samples in the same region. The band gap energy, E_g, was determined through the α value (m^{-1}) from a plot of $(\alpha h\nu)^{1/n}$ versus photon energy $(h\nu)$, where h is Planck's constant, ν is the frequency (s^{-1}) and the exponent n is the power factor of the optical transition mode. Note that n depends on the nature of the electronic transitions responsible for the absorption and is equal to 2 for allowed indirect transitions. The intercept of the tangent to the absorption curves was used to estimate the band gap (E_g) values of the samples, that were found to decrease according to the increasing amount of activated carbon content: 3.10, 2.85, and 2.66 eV for samples Ti, TiLAC9/1 and TiLAC7/3 respectively, indicating an enhancement of TiO_2 response in the visible light region [128].

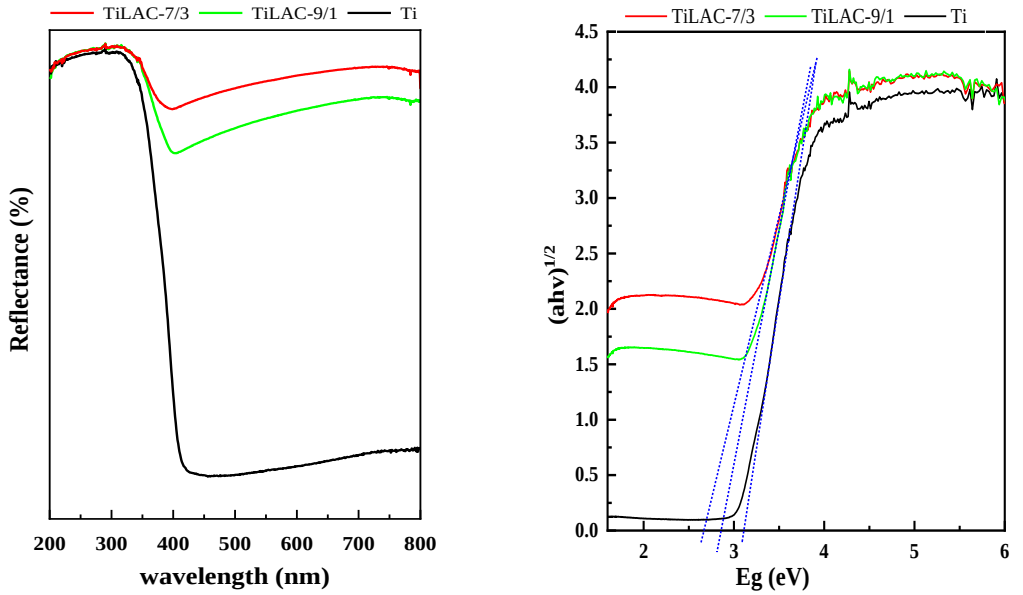

Figure 3.15. (a) UV-visible diffuse reflectance spectra and (b) energy band-gap vs $(ah\upsilon)^{1/2}$ of Ti; TiLAC-7/3 and TiLAC-9/1.

3.2.2 Methylene Blue Removal by Adsorption and Photocatalytic Degradation

The prepared TiLAC composites have been tested in the methylene blue dye (MB) photodegradation under UV light irradiation in an aqueous solution. The MB removal from the solution is likely due to a combined adsorption and photodegradation process. Figure 3.16a shows the variation of C/C_0 versus time in the experiment that includes a previous step of 30 minutes in darkness. During this dark step, LAC sample showed a high adsorption capacity of MB, which was expected according to its developed porosity, while

the pure titania sample, Ti, showed moderate adsorption, of ca. 10% of the MB initial concentration. However, the TiLAC composites showed much higher MB adsorption than pure Ti, 45% and 74% for TiLAC-9/1 and TiLAC-7/3, respectively, which are in agreement with the higher adsorption capacity of the activated carbon (see Table 1). Under UV-irradiation, the MB removal by the Ti sample reached 94% after 2 h. In contrast, using the TiLAC samples, the MB removal is faster and the total disappearance of the dye from the solution occurs within a maximum of 40 min or 60 min, depending on the TiLAC sample (Figure 3.16a). It must be considered that, in this case, the dye removal is the result of a combination of adsorption and photodegradation processes. A high concentration of MB is assumed to occur in the interphase Ti-LAC for the composite materials through adsorption, in contrast to what happens on Ti's surface, the adsorbed MB can then be photo-oxidized, leading simultaneously to LAC regeneration. This enhancement of the dye removal is in accordance with the LAC content in each sample, as the removal is faster for sample TiLAC-7/3 compared to TiLAC-9/1 and pure titania Ti, respectively. These results are in good agreement with those reported in the literature for methylene blue photocatalytic degradation where similar results using a carbonaceous TiO_2 composite material were obtained [31,234,237]. The UV-vis diffuse reflectance analysis shows that the bandgap of the prepared composites is lower than that of titania, which is attributed to the narrowing effect of the addition of LAC, which means an extension of the absorption of TiO_2 to the visible light range [238]. Thus, the prepared AdsCats could be photoactive in the visible light region.

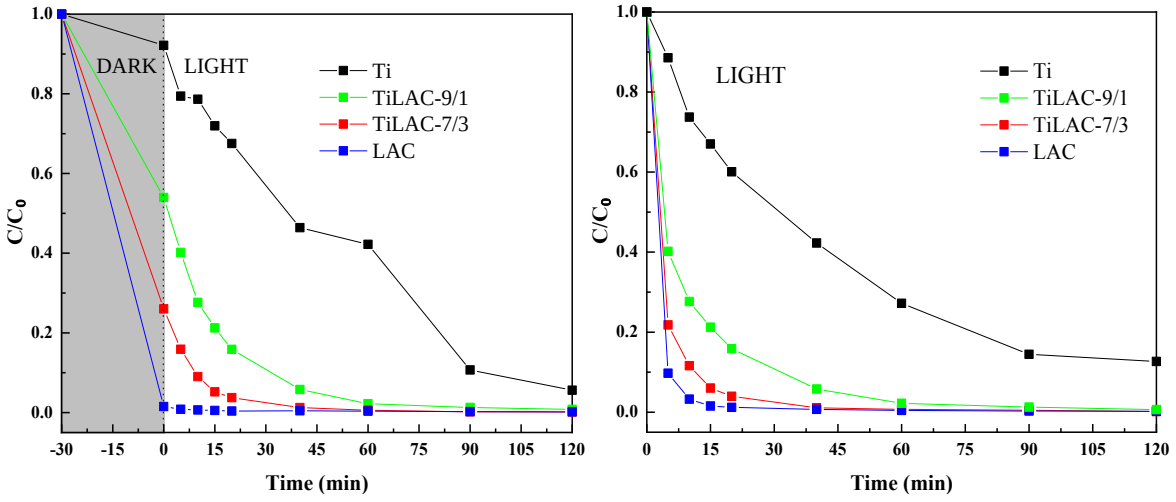

(a) (b)

Figure 3.16. Methylene blue removal on Titania P25 (Ti) and TiLAC based catalysts; (a) under dark and UV-irradiation; (b) under UV-irradiation without the first phase of adsorption equilibrium; with C (MB) = 6.0×10^{-5} M, catalyst dosage = 1.25 $g \cdot L^{-1}$ at 25 °C.

According to the results obtained when the UV lamp is switched on without the previous 30 minutes in darkness (Figure 3.16b), it is assumed that MB removal takes place by simultaneous adsorption and photocatalytic processes. The cationic dye is adsorbed from solution on the LAC porosity and then it reacts with the photoactive sites generated through the excitation of the irradiated titania's nanoparticles, resulting in the total dye elimination after 40 to 60 min UV-irradiation. There are no significant differences between the performance of the catalysts in the two tested scenarios. Thus, the second one, skipping ping the adsorption equilibrium step, is more efficient for direct MB removal from the point of view of saving time and energy. Figure 3.17 shows the experimental MB removal curves obtained for each composite and for its individual components (in the amount in which they are present in the composite) and the calculated MB removal by the composite considering the sum of the contribution of each component. These data suggest a synergetic effect between TiO_2 particles and LAC and, in this sense, the "excess" MB experimental removal with respect to the theoretical one would be related to photodegradation enhanced by the presence of LAC.

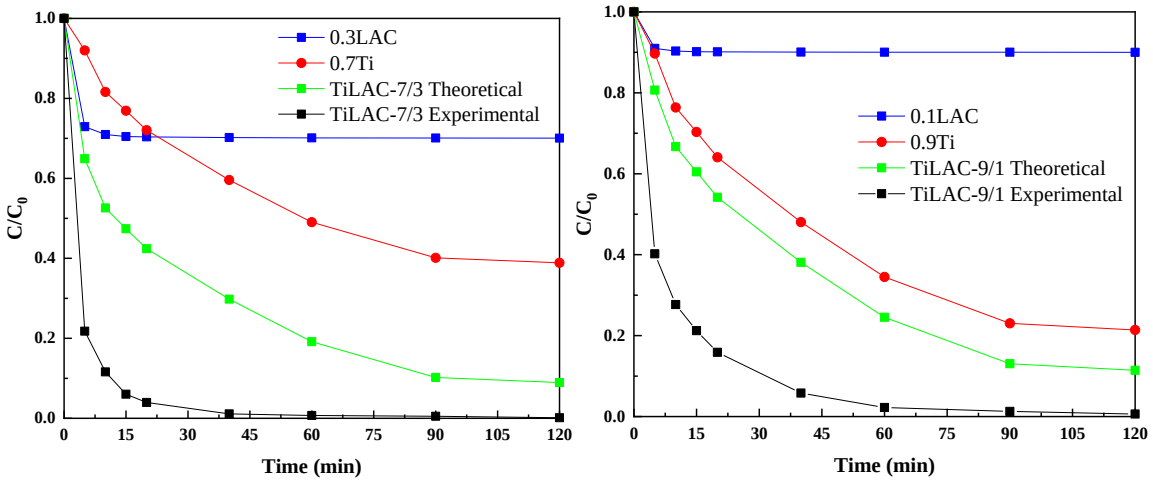

(a) (b)

Figure 3.17. Comparison of the experimental MB removal for (a) TiLAC-7/3 and (b) TiLAC-9/1 with that predicted according to their individual components and contents.

These results are consistent with the constant rates obtained from the kinetics modeling (Table 3.7), showing that the photodegradation of methylene blue by all the studied composites follows the first-order kinetics. The rate constant k was higher for

TiLAC-7/3 and TiLAC-9/1 samples, 0.377 and 0.276 min^{-1} respectively, while the Ti sample yielded the lowest value of 0.182 min^{-1}. It can be noticed that the removal efficiencies, previously shown, are in agreement with the constant rate value and strongly influenced by the content of LAC in each sample, since it seems to ensure a large interfacial surface available between titania particles and the dye molecules, as the BET specific surface areas confirm (see Table 3.3), providing abundant photoreactive sites and a developed porosity that facilitates the transfer of reactants and degraded products. Therefore, it seems that the higher the contact surface between AdsCats particles and MB, the greater the degradation rate.

Table 3.7. The rate constant k values for P25 and the TiLAC composites.

Sample	**k (min^{-1})**
TiLAC-7/3	0.377
TiLAC-9/1	0.276
Ti (P25)	0.182

Additionally, sample TiLAC-9/1 was treated at 250, 300, and 350 °C in a muffle furnace under air in order to investigate the influence of the oxidation state of Ti^{m+} functional species present on the external surface of the composite. The results of the photocatalytic activity experiments are presented in Figure 3.18. It can be observed that, even though no phase transformations were discerned in the three XRD patterns after thermal treatment (see supplementary info 3), some significant changes occurred from a catalytic point of view.

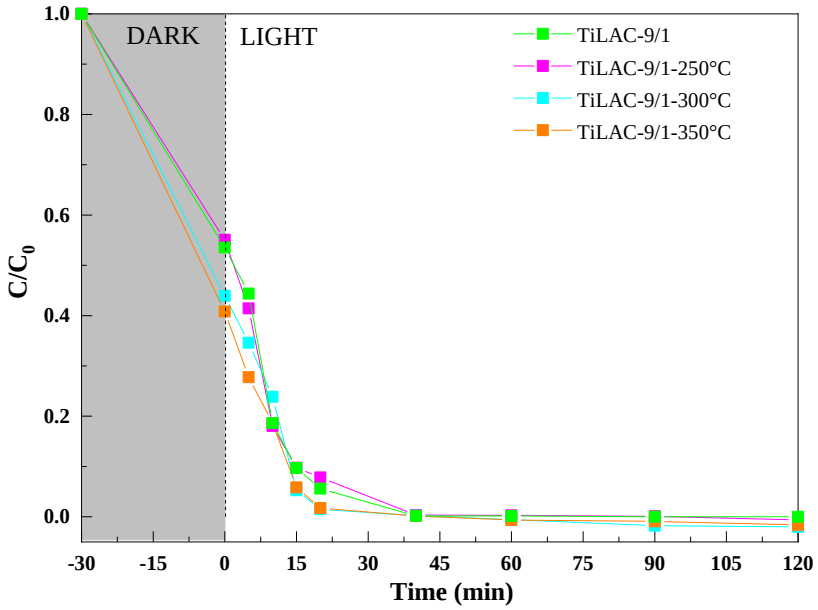

Figure 3.18. Methylene blue removal on TiLAC catalysts, TiLAC-9/1, TiLAC-9/1–250 °C, TiLAC-9/1–300 °C, TiLAC-9/1–350 °C heat-treated at different temperatures under dark and with UV-irradiation.

In particular, the thermal treatment at 250 °C did not have any noticeable effect on the photocatalytic activity, while the activities of the samples treated at 300 and 350 °C are higher as the time required for the extensive MB degradation decreases. This improvement can be related to the enhancement in the crystallinity and the formation of larger crystals of titania particles as a result of the thermal effect in the air on the composite materials at temperatures above 300 °C, rather than the oxidation state [239]. Furthermore, heat treatment allowed the adsorption of more oxygen molecules on the surface of the composite by correlating with Ti^{+4} ions. Thus, the presence of these oxygen molecules helps to trap photoexcited electrons and inhibit their recombination with holes. Hence, as the temperature increases, more superoxide anion radicals O^{2-} are formed and more hydroxyl radicals are stabilized by preventing combination [240], which is in agreement with Figure 11.

3.3 MALACHITE GREEN REMOVAL BY ADSORPTION ANDPHOTOCATALYTIC DEGRADATION UNDER SIMULATED SOLARLIGHT

3.3.1 Characterization of the prepared hybrid

3.3.1.1 X-ray diffraction

XRD analysis has been performed to evaluate the crystallinity of the different samples, and the corresponding patterns are presented in Figure 3.19 The characteristic XRD peaks of the TiO_2 phases were detected at the subsequent 2Θ values [27,128,241], see in brackets the corresponding families of planes.

- Anatase: 25.3° (101); 37.8° (004); 48.0° (200); 54.5° (105); 55° (211); 62.7º (204);70.4º (116); 74.5° (220)
- Rutile: 27.5° (110); 36.1° (101); 41.1° (111); 54.4 (211); 76.5° (202)

According to Figure 3.18, it is worth noting that brookite is not detected in any sample. The anatase crystalline phase is predominantly obtained in all the prepared samples. Samples TP from commercial P25, exhibit the rutile phase in addition to anatase while in sample TSG0 (spectra h), no crystallinity is depicted.

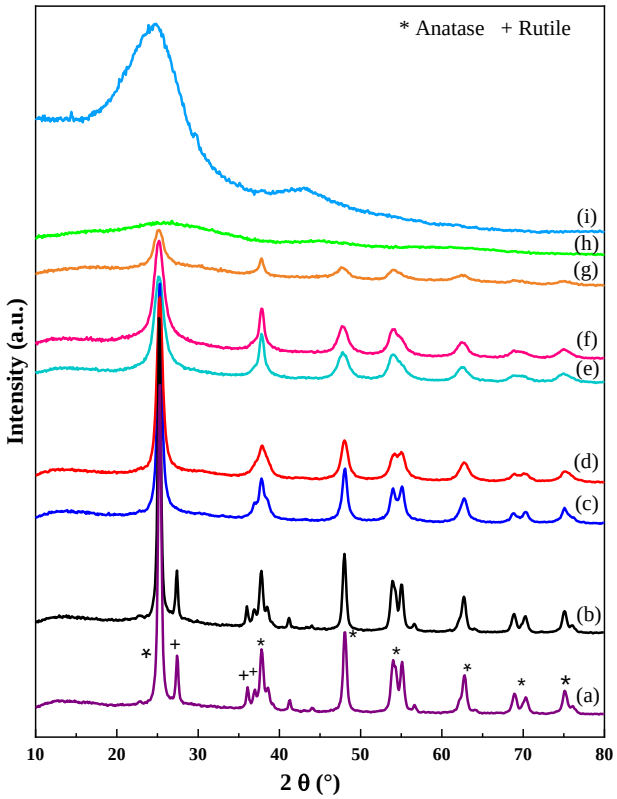

Figure 3.19. XRD patterns for (a) TP, (b) LAC_TP, (c) TSG0-350, (d) LAC_TSG0-350, (e) TSG, (f) LAC-TSG, (g) TSG0, (h) LAC_TSG0 and (i) LAC.

Table 3.8 summarizes the average crystallite sizes of anatase, and rutile expressed in (nm), and the amount (in wt.%) of both crystalline and amorphous TiO_2 in each material.

Table 3.8. Crystalline properties determined from XRD patterns

Samples	Average Crystal Size (nm)		Crystalline TiO_2 (wt.%)		Amorphous TiO_2 (wt.%)
	Anatase	Rutile	Anatase	Rutile	
TP	21	29	73	13	14
TSG	6	--	65	0	35
TSG0	6	--	47	--	53
TSG0-350	13	--	79	0	21
LAC_TP	21	29	63	12	26
LAC_TSG	6	--	53	0	47
LAC_TSG0	--	--	--	0	66
LAC_TSG0-350	10	--	76	0	24

No change in the average crystal size of both crystalline phases in the hybrid sample LAC_TP prepared by the MM method was observed respect to TP (Table 3.8). However, a minor decrease in such crystal sizes was noticed for hybrid samples prepared

by the SG method respect to pure TiO_2 samples. This diminution in the crystallite size could be related to the incorporation of LAC during TiO_2 synthesis by the fact that TiO_2 formation can occur inside the pores of the activated carbon and, thus, it limits its growth.

In sample LAC_TP the crystallinity of TiO_2 is only moderately affected by the introduction of LAC, with a decline of 10% (wt.). The crystallinity of the other hybrids (LAC_TSG, LAC_TSG0-350) is also reduced with the incorporation of LAC. This may be associated with the presence of decomposition products of AC into the crystalline structure of TiO_2. The lowest crystallinity was noticed for sample TSG0, which was completely lost after the incorporation of LAC. The amount of amorphous phase calculated for commercial TP titania is in agreement with data reported in the literature (14%) [242,243], which confirms the validity of the characterization approach. This amorphous phase amount increases in each sample after the incorporation of LAC in the hybrid materials.

3.3.1.2 Textural properties

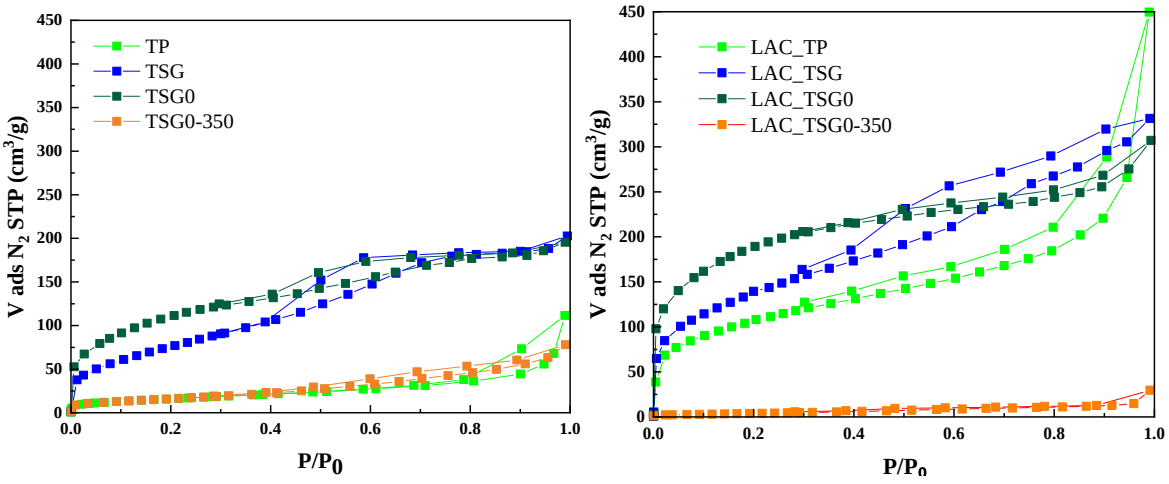

Figure 3.20. N_2 Adsorption-desorption isotherms at -196 °C for the prepared materials.

Adsorption-desorption isotherms of samples TP, LAC_TP, TSG0-350, LAC_TSG0-350, TSG, LAC-TSG, TSG0, LAC_TSG0, and LAC are illustrated in Figure 3.20. They are all of type IV according to the IUPAC classification, corresponding to mesoporous materials [43]. Their mesoporosity is also confirmed by the presence of the hysteresis loops. TP sample exhibits a hysteresis loop type H_3. This type bears a resemblance to the type II isotherm and indicates that the lower limit of the desorption section is located at the cavitation-induced P/P_0 in addition to the presence of some macropores in the pores network. On the other hand, the rest of the samples present a hysteresis loops type H_4

where the adsorption branch is a composite of Types I and II [43] and are generally found with micro-mesoporous carbons as confirming the V_{DR} from CO_2 adsorption (Table 3.9) and pore size distribution graphs (Figure 3.21).

Table 3.9: Textural parameters of the synthesized samples given by N_2 adsorption-desorption at -196°C and CO_2 adsorption at 0°C.

	S_{BET} [m^2g^{-1}]	V_{Total} [cm^3g^{-1}]	$V_{DR}N_2$ [cm^3g^{-1}]	V_{MESO} [cm^3g^{-1}]	$V_{DR}(CO_2)$ [cm^3g^{-1}]
LAC	1139	1.15	0.48	0.66	0.19
TP	60	0.1	0.02	0.08	0.02
LAC_TP	383	0.34	0.16	0.28	0.07
TSG	290	0.31	0.11	0.17	0.05
LAC_TSG	498	0.48	0.21	0.27	0.07
TSG0	395	0.27	0.16	0.11	0.07
LAC_TSG0	623	0.47	0.31	0.12	0.15
TSG0-350	60	0.12	0.02	0.06	0.02
LAC_TSG0-350	16	0.019	0.01	0.01	0.01

The initial monolayer-multilayer adsorption on the mesopore walls at low relative pressure is rapid for LAC, TSG, TSG0, LAC_TSG, and LAC_TSG0, in agreement with the obtained developed surface area and porous volume values presented in (Table 3.9). This indicates that the micropores could rapidly be filled and saturated with MG molecules. An increase in the surface area of samples containing luffa-activated carbon is noticeable, pointing out that the addition of luffa-activated carbon to the TiO_2 particles enhances the surface area of the composites. Whereas a decrease is attributed to the samples prepared by an acid-free sol-gel method that has been undergone a heat treatment (TSG0-350 and LAC_TSG0-350).

A pore size distribution at around a mean value of 3.51 nm for TP and the hybrid materials prepared by acid-free sol-gel method verified the presence of mesopores, while for the other hybrids and LAC, a mixture of micropores with mesopores can be observed (see Figure 3.21). Therefore, with the overage pore diameters range of 1.5-3.6 nm, the malachite green molecules with the size of (1.4 nm × 1.1 nm × 0.5 nm) [244], could easily fit and integrate inside the pores of the prepared materials.

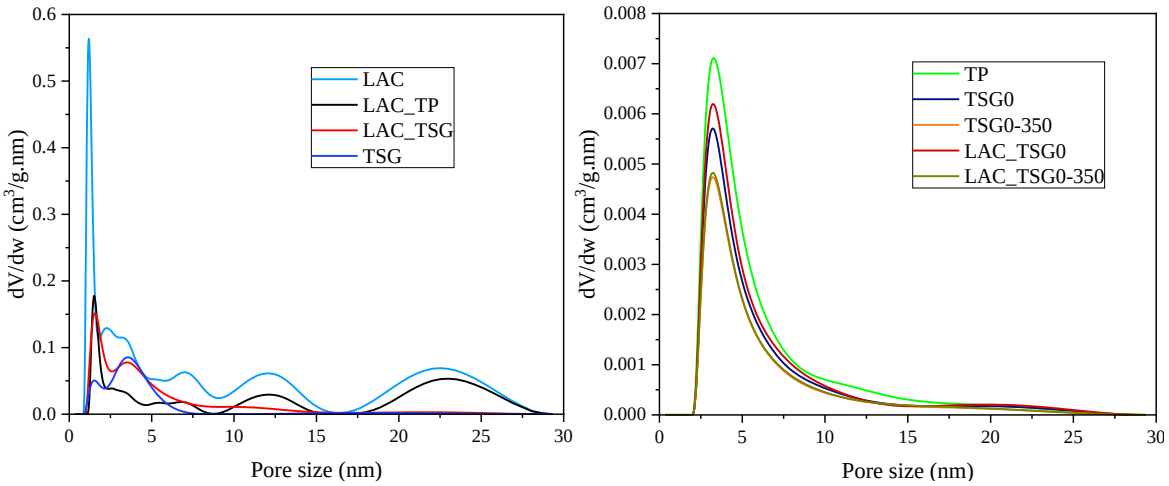

Figure 3.21: Pore size distribution for the prepared materials obtained from adsorption-desorption isotherms data.

3.3.2 Malachite green removal

3.3.2.1 Adsorption test

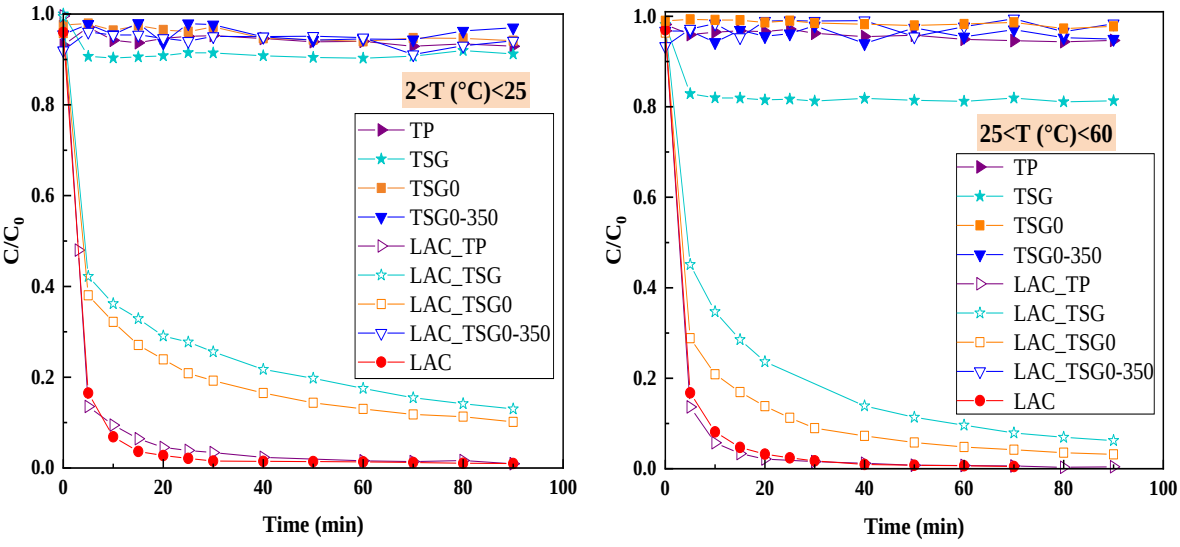

(a) **(b)**

Figure 3.22. Adsorption test of MG for the prepared catalysts under dark and in the following conditions (photocatalyst dosage m=0.125 g, malachite green concentration C_0 (MG) =10 mg/L and volume of (MG) solution = 250 mL, pH=5.76 and at low and moderate temperature)

Figure 3.22 plots the MG adsorption data for the prepared and selected materials at a low temperature 2< T °C< 25 and moderate temperature 25< T °C< 60. At the first regime, MT, the adsorption phenomenon is negligible over most bare titania samples (TP, TSG, TSG0, TSG0-350) and over LAC_TSG0-350. Under LT some adsorption (around 20% MG removal) is observed for the TSG sample.

LAC presents, as expected, an important MG adsorption capacity, which is due to its high surface area of 1139 m²/g and porous texture. Materials containing LAC show a noticeable MG adsorption capacity, except for the LAC_TSG0-350 sample. The negligible adsorption in the LAC_TSG0-350 sample is the consequence of the poor textural properties after the heat treatment performed during the preparation of this sample.

Comparing the adsorption for all the samples in both temperature regimes, the difference in the adsorption capacity is negligible. Adsorption is an exothermic phenomenon, showing better results for lower temperatures. Although the important removal of the dye from the solution, still, and following the UV visible measurements of the absorbance of MG dye after 3 h of the adsorption process, a significant quantity of MG was left behind in the aqueous solution, indicating that MG has not been totally adsorbed/removed by the adsorption process that occurred over the tested sample. Being the adsorption a surface phenomenon, the dyes molecules emigrate and diffuse inside the pores due to diffusion without total elimination and with a possible desorption behavior.

- Removal of MG with LAC

Photodegradation experiments were performed with bare Luffa activated carbon under the same above-mentioned conditions and the results are plotted in Figure 3.23.

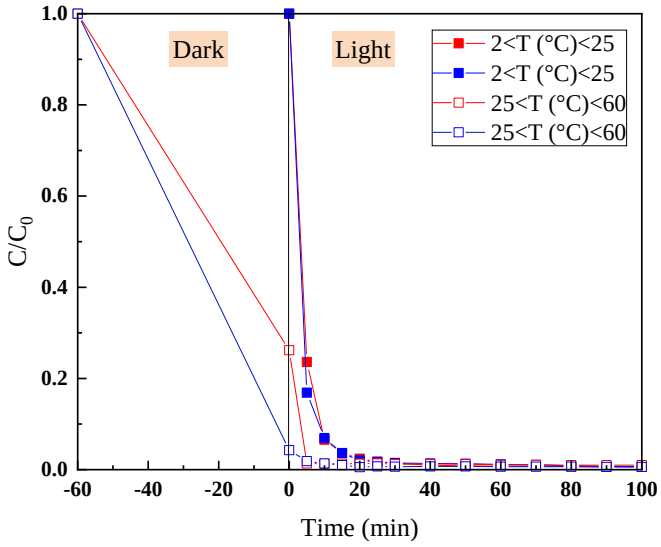

Figure3.23. Photodegradation of MG using Luffa activated carbon sample in absence of Titania particles under the following conditions (photocatalyst dosage m=0.125 g, malachite green concentration C_0 (MG) =10 mg/L and volume of (MG) solution = 250 mL, pH=5.76, at (■) low and (□) moderate temperature)

This experiment was conducted to investigate, on one hand, the MG adsorption over LAC in absence of light and, on the other hand, to inspect if LAC showed any photodegradation activity. As figure 3.23 shows, the removal of MG from the solution over the LAC sample is the same under dark or irradiation. Such removal is due to adsorption phenomena and not to photocatalysis.

3.3.2.2 Photolysis test

Under simulated sunlight irradiation, a photolysis test for malachite green dye solution (in absence of the catalyst) was performed to verify any auto-degradation of the dye. As expected, the malachite green in solution did not degrade in absence of the photocatalyst (see Figure 3.24), which verifies that in visible light MG is stable, and such light irradiation alone is not sufficient so that a photodegradation reaction of the dye would take place.

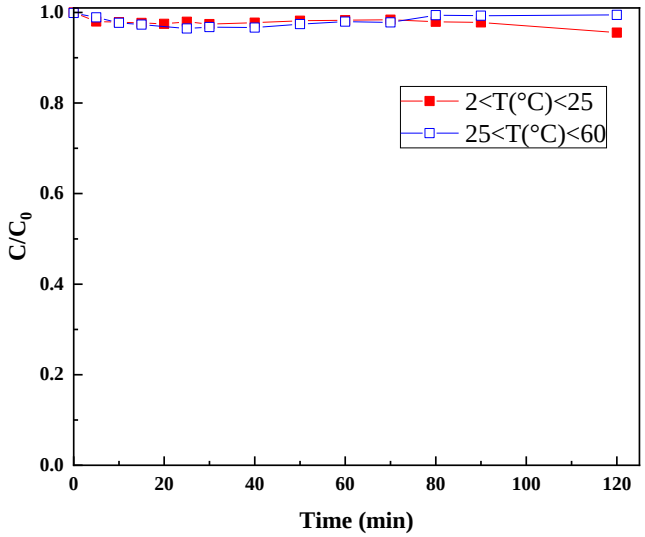

Figure 3.24. Photolysis test of MG under the following conditions (photocatalyst dosage m=0.125 g, malachite green concentration C_0 (MG) =10 mg/L and volume of (MG) solution = 250 mL, pH=5.65, at moderate (■) and low temperature (□))

3.3.2.3 Removal of MG with the TiO_2/LAC photocatalysts

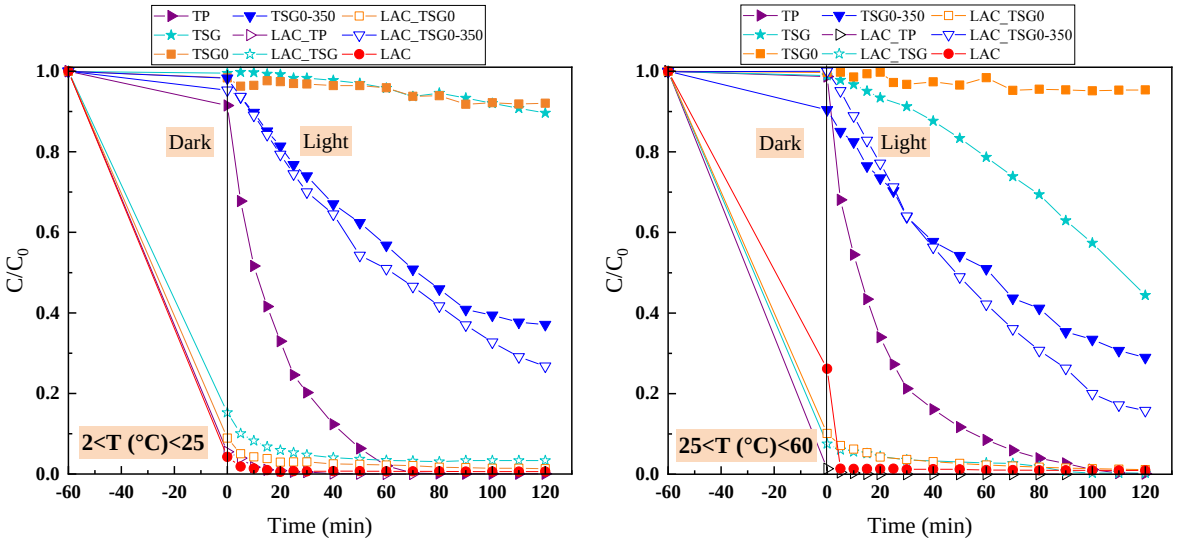

(a) (b)

Figure 3.25. Photodegradation of MG using the prepared photocatalysts materials under dark and simulated solar light irradiation and the following conditions (photocatalyst dosage m=0.125 g, malachite green concentration C_0 (MG) =10 mg/L and volume of (MG) solution = 250 mL, pH=5.76, at low (a) and moderate (b) temperature).

The photodegradation activity of MG dye over the prepared samples expressed by the variation of C/C_0 versus time is compiled in Figures 3.25 and 3.26. Each experiment is performed in two steps. The first step consisted of a 60 min dark period to reach adsorption equilibrium before the irradiation at a low temperature (Figure 3.25.a) and moderate temperature (Figure 3.25.b). From Figure 3.25, it can be concluded that the samples of bare titania showed a moderate adsorption behavior, of around 10% of MG initial concentration, whereas the composites containing LAC, as expected, showed a higher adsorption capacity than bare titania, ranging between 85% and 95% of MG initial concentration. This behavior is expected and attributed to the porous characteristic of activated carbon (see Table 3.9).

Once the effluent solution is exposed to irradiation, photodegradation occurred over most bare titania and LAC-containing samples. TSG0 is not photoactive (for being amorphous, according to the XRD analysis), while the TSG sample presented a moderate activity only at controlled temperature. Forbye, among the bare titania samples, the TP sample showed the best performance with a removal rate of 95% within 60 min of irradiation. Nevertheless, the removal over samples containing LAC is higher than bare

titania samples. It is worth mentioning that the removal, in this case, is a result of both adsorption and photodegradation combined simultaneously, where the adsorption would permit the "fixation" and transfer of MG molecules on the surface of the composites, leading to its degradation once exposed to irradiation, and permitting instance evacuation of the active sites to ensure fast removal of the dye, about 99% within 40 min of irradiation. Last but not the least, controlling the temperature did not highly affect the removal performance showing the same results for the whole studied range of temperature.

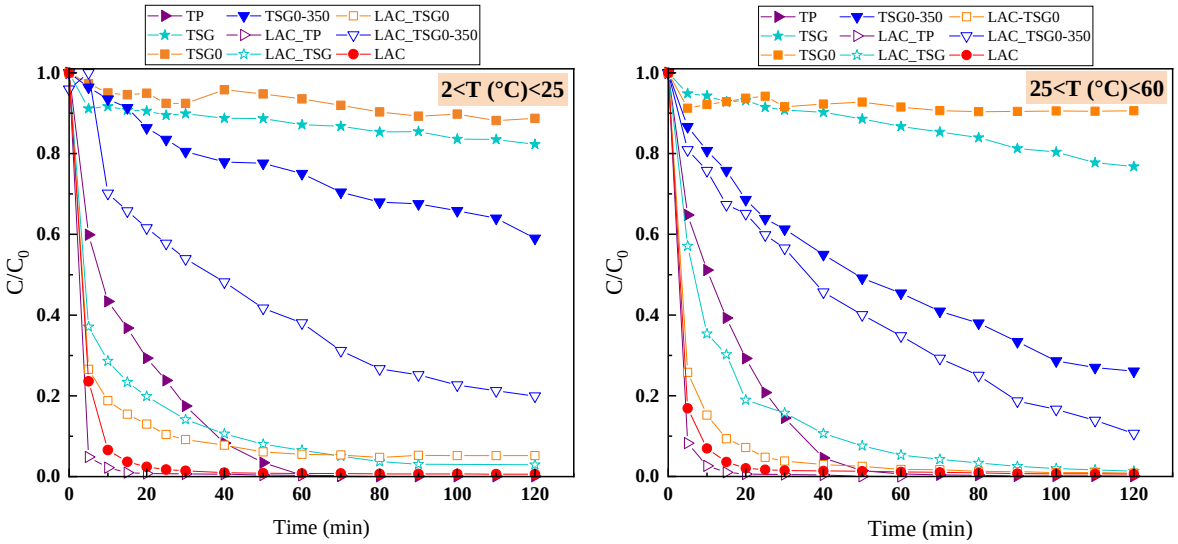

Figure 3.26. Photodegradation activity of MG for the prepared photocatalysts under simulated solar light irradiation and skipping the dark period of adsorption equilibrium under the following conditions (photocatalyst dosage m=0.125 g, malachite green concentration C_0 (MG) =10 mg/L and volume of (MG) solution = 250 mL, pH=5.76, at (a) low and (b) moderate temperature).

The second set of experiments consisted of irradiation with simulated solar light once the materials and MG solution are in contact at a low temperature (Figure 3.26.a) and moderate temperature (Figure 3.26.b). In general, and as in the previous case, controlling the temperature of the reaction medium did not affect the removal performance. MG removal by materials containing luffa activated carbon is more efficient than for any bare TiO_2 sample. Full degradation of the dye is reached after 30 min exposure to the simulated light for samples LAC, LAC_TSG, and LAC_TP, been those more efficient than commercial TP (P25). From the comparison of Figures 3.25 and 3.26, it can be noticed that all the composite materials are photo-catalytically active and follow the same tendency under all the experiment's conditions. As a result, it can be concluded that performing the

direct photodegradation of MG dye without reaching the adsorption equilibrium is better from the point of view of saving time and energy since the same results are obtained.

Table 3.10. The constant rate k values for TP, LAC, and the hybrids for the four different regimes of the photodegradation experiments.

Samples	Constant Rate k (min^{-1})			
	Dark/MT	**Dark/LT**	**Without dark/MT**	**Without dark/LT**
LAC	0.416	0.217	0.5	0.516
TP	0.123	0.121	0.140	0.153
TSG	0.006	3.49×10^{-4}	0.011	0.013
TSG0	0.001	8.96×10^{-4}	0.010	0.009
TSG0-350	0.025	0.021	0.041	0.014
LAC_TP	0.466	0.270	0.684	0.675
LAC_TSG	0.057	0.121	0.081	0.213
LAC_TSG0	0.094	0.124	0.352	0.274
LAC_TSG0-350	0.032	0.019	0.058	0.072

Dark/MT: under dark at moderate temperature
Dark/LT: under dark at low temperature
Without dark/MT: absence of dark at moderate temperature
Without dark/LT: absence of dark at low temperature

Table 3.10 regroups the constant rate obtained from the kinetics modeling for the different photodegradation experiments performed under the two regimes of temperatures. These results showed that the photodegradation of malachite green by all the studied materials follows the first-order kinetics. The rate constant k was higher for the hybrids, with LAC_TP and LAC_TSG0yielding the best value of 0.684 and 0.352 min^{-1} under moderate temperature with skipping the adsorption step. The lowest values of 0.001 and0.006 min^{-1} were attributed to TSG and TSG0 samples that have shown the worst photocatalytic behavior. As it can be seen, the removal efficiencies previously discussed are in agreement with the constant rate value. They are strongly influenced by the addition of LAC in the hybrid samples that provides a high contact surface rich in photoactive sites. In addition, these values confirm that performing the photodegradation experiments directly without reaching the adsorption equilibrium and under moderate temperature yields a better degradation rate.

3.3.2.4 Contribution of each process (adsorption/photodegradation) in MG removal

This section aims to determine if the presence of titania and LAC in the composites presents some synergic effect and/or to compare if the two materials separately have the same photodegradation performance. Thus, in order to understand the relative contribution of each process (adsorption/photodegradation) on MG removal, in this section, the performance of the composites from the point of view of MG removal is compared with the removal that would occur for each component loading separately: a mass of 0.0375 mg for LAC and 0.0875 mg for titania, correspond respectively to 30% LAC and 70% titania content in the composite (the sum of both masses is equal to the composite dosage (0.125 g represents (100 %)). The samples nomenclature is explained in the following Table 3.11, taking the first series presented in figure 3.27.a. as an example:

Table 3.11: signification of the nomenclature of each sample used in the contribution tests

Nomenclatures	Signification and content
TP	100% Titania
LAC	100% LAC
LAC_TP	70% TP+ 30% LAC
TP-70%	70% Titania
LAC-30%	30% LAC

According to Figure 3.27, LAC presents a high removal rate due to the adsorption capacity related to its high surface area. LAC-30% doesn't reach full adsorption/removal capacity, which is expected since the amount is lesser. This means that this fraction of LAC (30%) is not sufficient for the total removal of MG when the adsorption phenomenon occurred. The same behavior is noticed for 70% of bare titania samples, where MG removal is not complete reaching only 85% within 60 min, compared to 98% for the TP sample at 100% loading for the same period.

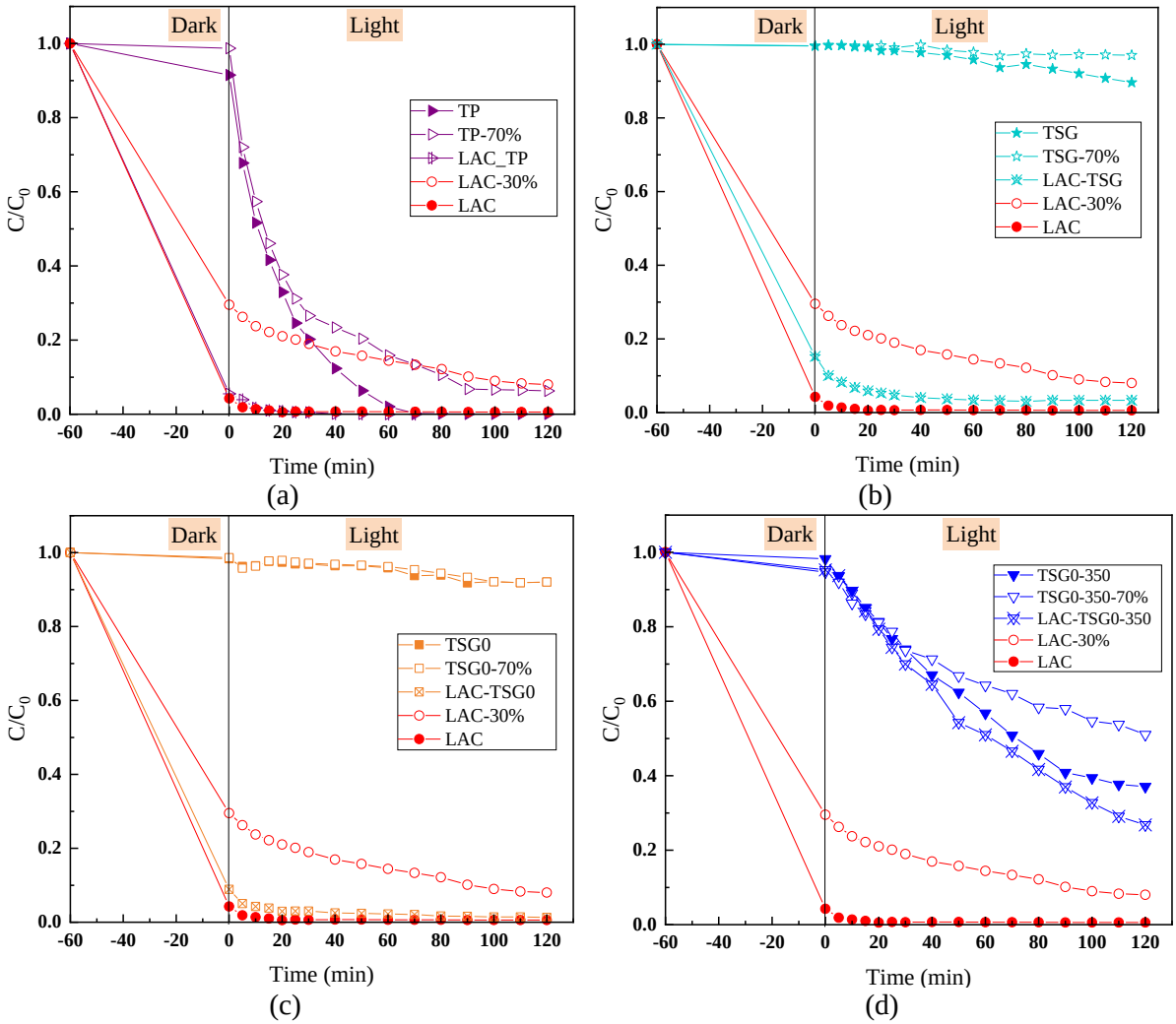

Figure 3.27. Comparison of the photodegradation activity of MG for different mixed and bare Titania samples under the following conditions (malachite green concentration C_0 (MG) =10 mg/L, the volume of (MG) solution = 250 mL, pH=5.76, at moderate temperature). With 70 and 30% correspond respectively to titania and LAC loading in each composite material

On the other hand, it is relevant that composite materials of TiO_2 and LAC samples are more active than both components separated. For example, a substantial enhancement of the photodegradation was observed for the LAC_TSG sample after the incorporation of LAC, from 5% for bare TSG to 98% for the LAC_TSG sample respectively. The above results showed that the mixture Titania/LAC was more efficient for the total removal of the dye, suggesting the presence of a possible synergic effect between the two materials.

3.3.2.5 Photodegradation pathway and interfering agents

Various reactive species, such as OH• radicals, positive holes (h^+), and superoxide anion radicals (O_2•), can participate in the photocatalytic degradation of organic compounds. To evaluate the contribution of the main reactive species and elucidate the photocatalytic mechanism involved in the MG degradation, the photodegradation behavior in the presence of different electron and hole scavengers was studied. The LAC sample, two samples presenting good photodegradation performance TP and LAC_TP, and two with less-moderate activity as TSG0 and LAC_TSG0 were chosen. The corresponding results are presented in, both, Figures 28 and 29 respectively.

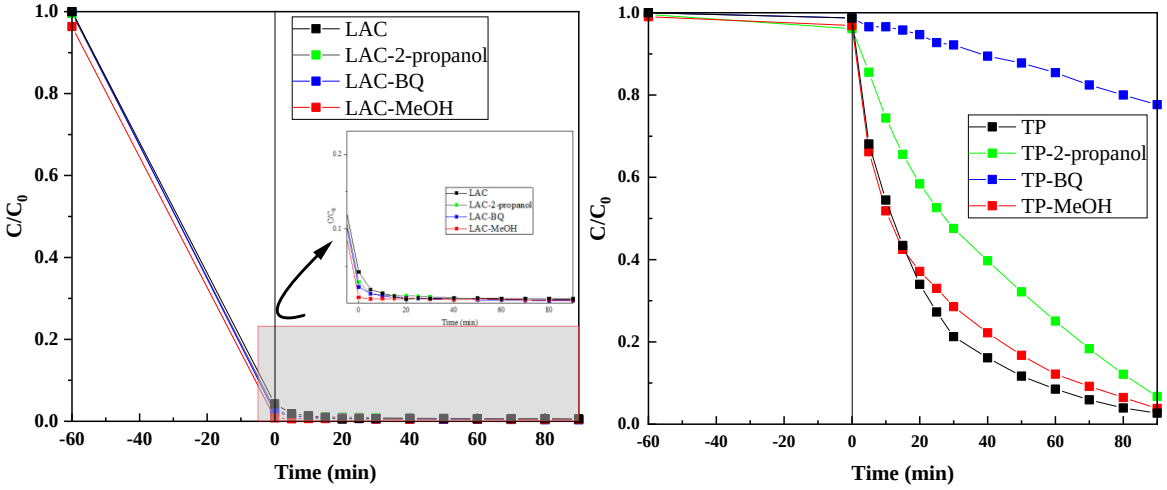

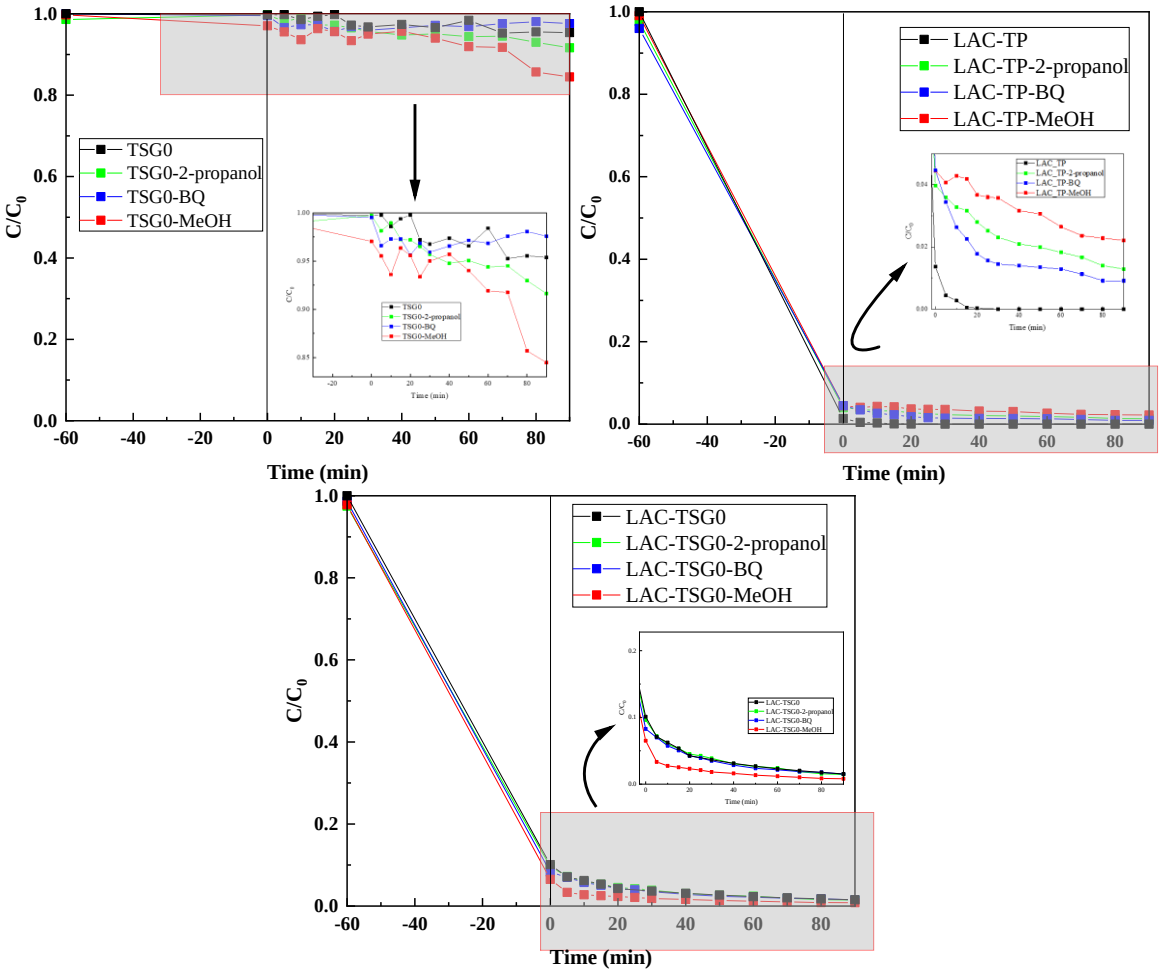

Figure 3.28. Photodegradation behavior of MG dye over LAC, TP, TSG0, LAC_TP, and LAC_TSG0 photocatalysts materials under dark at moderate temperature (25 <T (°C) < 60) in the presence of different scavengers 2-propanol, BQ, and MeOH.

- *Effect of hydroxyl radicals*

generally, when irradiating semiconductors, a positive hole (h^+) is left in the valence band (VB) as a result of electrons (e^-) migration from this last to the conduction band (CB). Thus, hydroxyl radicals could be produced through the oxidation of both water and hydroxyl groups by the holes [170]. Taking the case of TP sample, the addition of 2-propanol as hydroxyl groups scavenger decreased notably the MG photodegradation over this last from 80% to 53% in 30 min. Considering the LAC_TP sample, and that most of the concentration of MG was adsorbed over it, this last evinced a 2% decrease of C/C_0 rate for the same period (30 min) in the presence of 2-propanol compared to its original behavior without scavengers. This indicates that hydroxyl radicals participate in the degradation of MG dye over both samples. On the other hand, the behavior of TSG0 and LAC_TSG0 samples in presence of 2-propanol was different. It can be

noticed that almost no photodegradation of MG has occurred over these samples (Figure 28). This behavior was expected regarding that these samples do not present any crystal phase as confirmed by XRD analysis. However, adsorption of water molecules on the surface of the composite favors hydroxyls radicals generation as reported by Neto et al. [170]. Therefore, and, being MG widely adsorbed on the surface of the composite LAC_TSG0, the production of hydroxyl radicals was reduced as most active sites were previously occupied by MG molecules explaining, furthermore, the minor participation of these radicals on the MG degradation. As no photodegradation activity occurred over the LAC sample, no effect was observed in the presence of the above-discussed hydroxyl scavenger.

- *Effect of superoxide scavengers*

superoxide anions radicals ($\bullet O_2^-$) are considered an active oxidative species able to degrade several organic pollutants. MG dye molecules could be photosensitized to an excited single state (dye*) through irradiation, leading to an injection of electrons on the TiO_2 conduction band. Hence, The reaction of these lasts with molecular oxygen adsorbed on the catalyst surface triggers the formation of superoxide radicals anions and/or hydroperoxide radicals ($HO_2\bullet$) which conduct furthermore to the formation of hydroxyl radicals [170,245]. The contribution of these superoxide radicals was investigated using benzoquinone (BQ) as it has the potential to trap superoxide anions ($\bullet O_2^-$) by an electron transfer mechanism ($BQ+ \bullet O_2 \rightarrow \bullet BQ^- + O_2$). As it can be seen from figure 28, the degradation of MG dye was remarkably inhibited by the presence of benzoquinone ($\bullet O_2^-$ quencher) for TP and LAC_TP samples, suggesting that the superoxide anions radicals are the major contributor instead of hydroxyl radicals OH• for MG degradation over TP sample. On the other hand, no inhibitory effect was depicted for the TSG0, LAC_TSG0, and LAC samples concerning this scavenger, indicating that $\bullet O_2^-$ radicles are not the responsible reactive species for MG degradation over these samples, being the result of LAC expected as no photodegradation took place confirming. These observations suggested that the addition of LAC reduced the formation of these radicals and/or favored their reaction with electrons as mentioned previously, to form hydroxyl radicals OH• which explains their major participation in MG photodegradation for the LAC_TP sample. Also, it is

presumed that the preparation method affects the behavior of the functional species present in the reaction medium illustrated by the notable difference in photodegradation behavior over the two series of samples prepared by mechanical mixing and sol-gel methods.

- *Effect of photogenerated holes (h^+)*

The participation of photogenerated holes (h^+_{vb}) issued from the irradiation of catalyst surface was verified using methanol (MeOH) as a scavenger. As shown in figure 28, photogenerated holes are the predominant active species for MG degradation over the LAC_TP sample more than for the TP sample. The degradation rate was increased for the LAC_TSG0 sample in the presence of the holes scavenger. This increase could be attributed to the fact that the substrate is been reduced more than been oxidized under these conditions [246]. As noticed for the other reactive species, •OH and $•O_2^-$, and as no degradation process has occurred, no crucial role of holes was registered for LAC and TSG0 samples. On contrary, the addition of methanol quencher strongly inhibited the photodegradation rate of MG over TP and LAC_TP samples. The decrease in the degradation rate is a result of the suppressing of the hole-electron recombination effect and the removal of most of the photogenerated holes as the main responsible for the oxidation of the dye molecules, caused by the presence of methanol as a classical h^+ scavenger [247].

Additional tests were performed under the same previous experimental conditions were followed except that the photodegradation was started directly, avoiding the necessary dark period for establishing adsorption-desorption equilibrium.

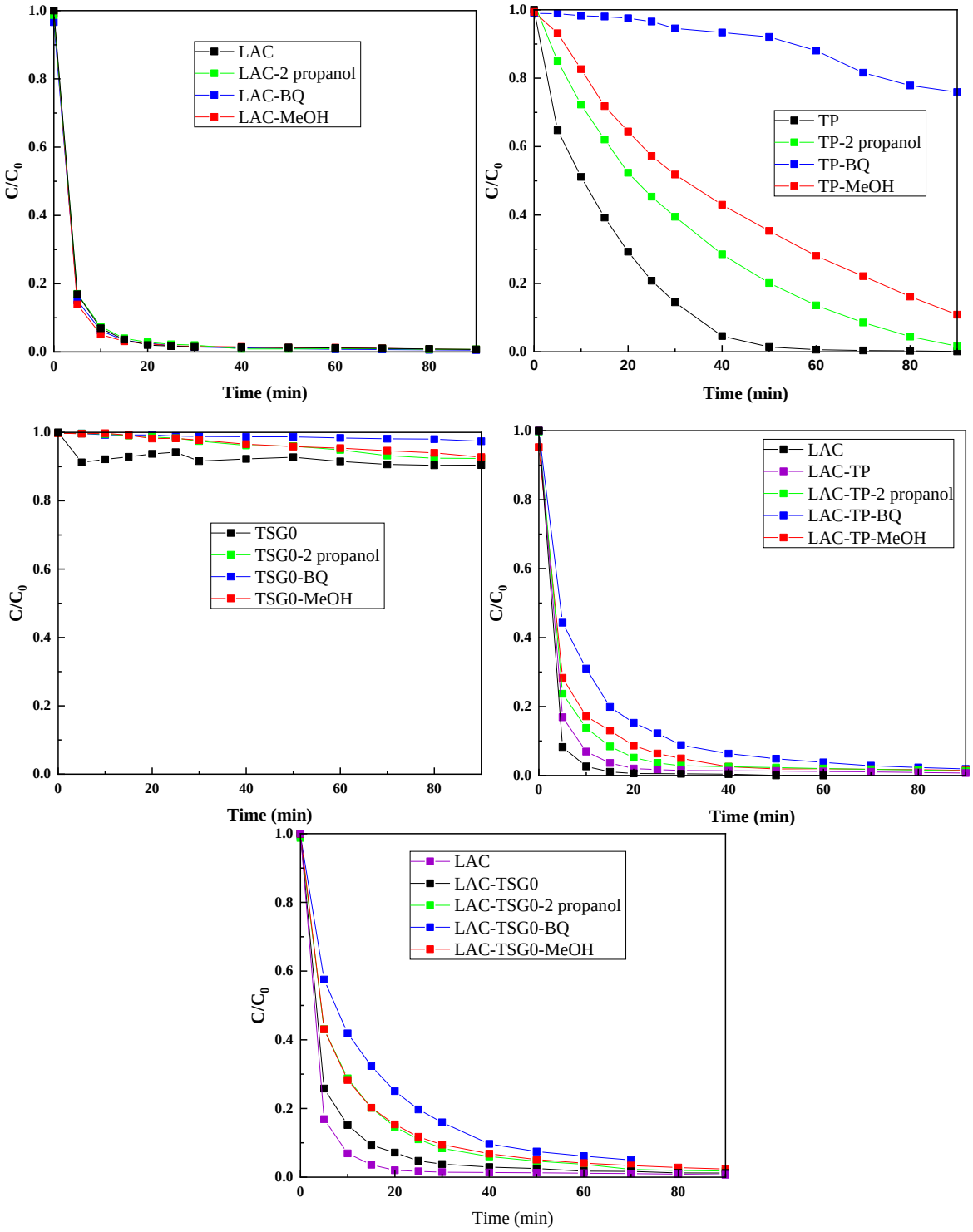

Figure 3.29. Photodegradation of MG over LAC, TP, TSG0, LAC_TP, and LAC_TSG0 photocatalysts materials at moderate temperature (25 <T (°C)< 60) and skipping adsorption equilibrium, in the presence of different scavengers 2-propanol, BQ and MeOH.

The same previous scavengers were used to perform the same experimental tests to investigate the interfering agents participating in the MG degradation, in this case, directly without reaching adsorption equilibrium. This time the pathway trend for all the samples

was clear. Concerning LAC sample, and as previously discussed, the three scavengers did not have any inhibitory effect on the LAC sample, confirming the domination role of adsorption with no photoactivity behavior for this sample. As it can be clearly observed in figure 29, the degradation rate for TP, LAC_TP, and LAC_TSG0 was strongly inhibited by the presence of benzoquinone indicating that superoxide radicals $\bullet O_2^-$ are highly involved in the MG photodegradation, followed by moderate participation of photogenerated holes h^+, while hydroxyl radicals •OH presented the lowest contribution. Hence, the trending of the reactive species contribution to MG photodegradation is in the order $\bullet O_2^- > h^+ > \bullet OH$. Consequently, the scavengers indicated that the charge carrier recombination can be efficiently suppressed, and helped endorse that the photodegradation of MG was an oxidative process.

GENERAL CONCLUSIONS AND FUTURE PERSPECTIVES

GENERAL CONCLUSION AND FUTURE PERSPECTIVES

As the valorization of widely abundant lignocellulosic material is a current trend. The work in this thesis deeply analyzed the preparation of highly porous activated carbons derived from the lignocellulosicfibers*"Luffa cylindrica"* with different textural properties. Thereafter, their possible use as catalytic support of TiO_2semiconductors, at various rates, for the photodegradation of textile pollutants in the liquid phase under the effect of UV and solar irradiations was investigated**.**

The activated carbons derived from Luffa fibers (LACs) were successfully prepared by chemical activation with phosphoric acid under different preparation conditions. The influence of activating agent (H_3PO_4) to carbon precursor (Luffa) mass ratio (1, 3, and 5) and the activation temperature (500, 550, and700 ºC) on their textural properties has been studied. In this sense, these activated carbons have been thoroughly characterized by different techniques such as BET, SEM, ATG-DSC, CHNO, XPS…etc.

Each studied parameter affects the porosity development of the LACs. Phosphoric acid was responsible for the growth in porosity by favoring the release of tars from the cross-linked framework of the fibers. However, if excessively used, it could lead to the destruction of the textural properties. Also, an appropriate carbonization temperature (500°C) could significantly enhance the growth of the porosity and the surface area, while an excessive raise has the opposite effect. Analyzing all these results emphasized that the use of this acid makes it possible to work at low temperatures with an activation time of 60 minutes only.

The BET Analysis for the activated carbons showed obtaining high surface areasnearly reaching 1400m²/g and a significant mesoporous volume. Whereas, SEM analysis confirmed their porous morphology. These two texturales characteristics give an outline of the obtained activated carbon quality. On the other hand, ATG and CHNO analysis revealed a high carbon content and the presence of oxygen surface groups which was also confirmed by XPS analysis. According to these results, Luffa cylindrica can be promoted to be a good precursor for a highly activated carbon preparation.

The composite materials have been prepared by two different methods. The simple mechanical mixing of TiO_2 and luffa activated carbon and sol-gel methods. The composites showed high specific surface areas related to their LAC content (around 300

m^2/g compared to bare titania 60 m^2/g). TiO_2 particles are well dispersed on the LAC surface, homogenously covering most of its surface as mapping images from SEM analysis revealed. XRD analysis revealed that anatase is the dominant crystalline phase in the photocatalysts containing TiO_2.The presence of oxygen and phosphorus complexes on the LAC carbon confer high oxidation resistance and active sites that lead to improved adsorption and photocatalytic properties. Furthermore, the interface formed between the solid phases due to mixing mechanically titania and LAC favored the interaction pollutant/Photocatalyst.

Regarding the photocatalytic behavior, the samples showed a good performance, leading to the total removal, for both studied dyes, after 30 min of exposure to the irradiation source. The photo-response confirmed that a suitable Eg is obtained for the sample containing 10% LAC (the band gap decreases from 3.10 eV, for pure titania, to 2.66 eV) which is ascribed to the formation of TiO_2-LAC heterojunction. This extension of the catalyst absorption to visible light can enhance the catalytic activity. The studied photocatalysts showed, in fact, a higher degradation rate than the corresponding bare TiO_2 attributed to the presence of LAC. The dyes initially interacted with highly adsorbing LAC and via spillover of the mass through the contact surface, the photoactive titania enabled the photodegradation processes.

To conclude, *luffa cylindrica* appeared to be a suitable precursor for the elaboration of a highly porous activated carbon which proved to be good support with an outstanding contribution for photocatalytic applications in aqueous solution. For further study, it would be enriching to continue this work by a comparative study of the photocatalytic activity on the activated carbons prepared with different ratios to study the effect of the support. In addition, investigating other binary and ternary semiconductors using doping method to decrease the band gap for photodegradation purposes under solar light. Itis also required to test its effectiveness in the photodegradation process of other pollutants (pharmaceuticals and organic solvents) and in the gaseous phase for VOC removal.

SUPPLEMENTARY INFORMATIONS

- 1) Calibration curve of malachite green solution

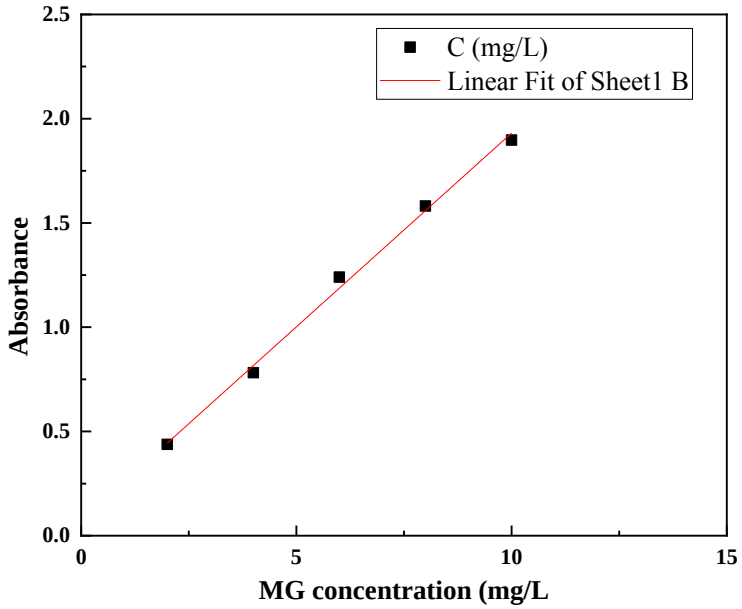

- 2) TG-DTG-DSC curves for activated carbons prepared at different temperatures of activation and impregnation ratios maintained for 2 hours.

(a)

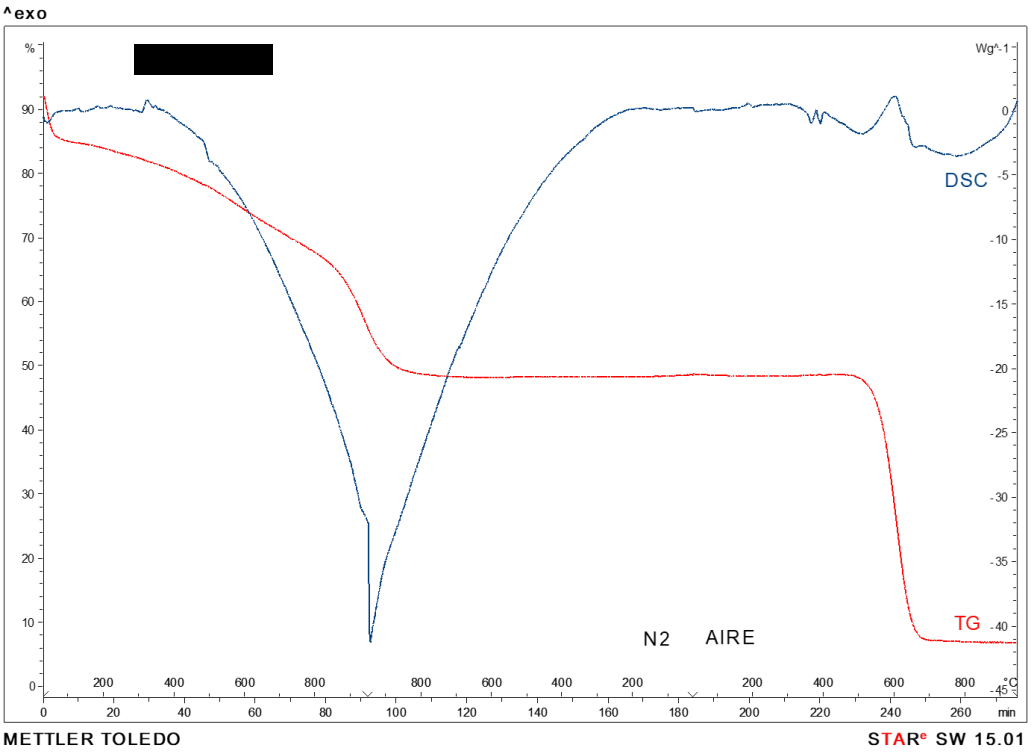

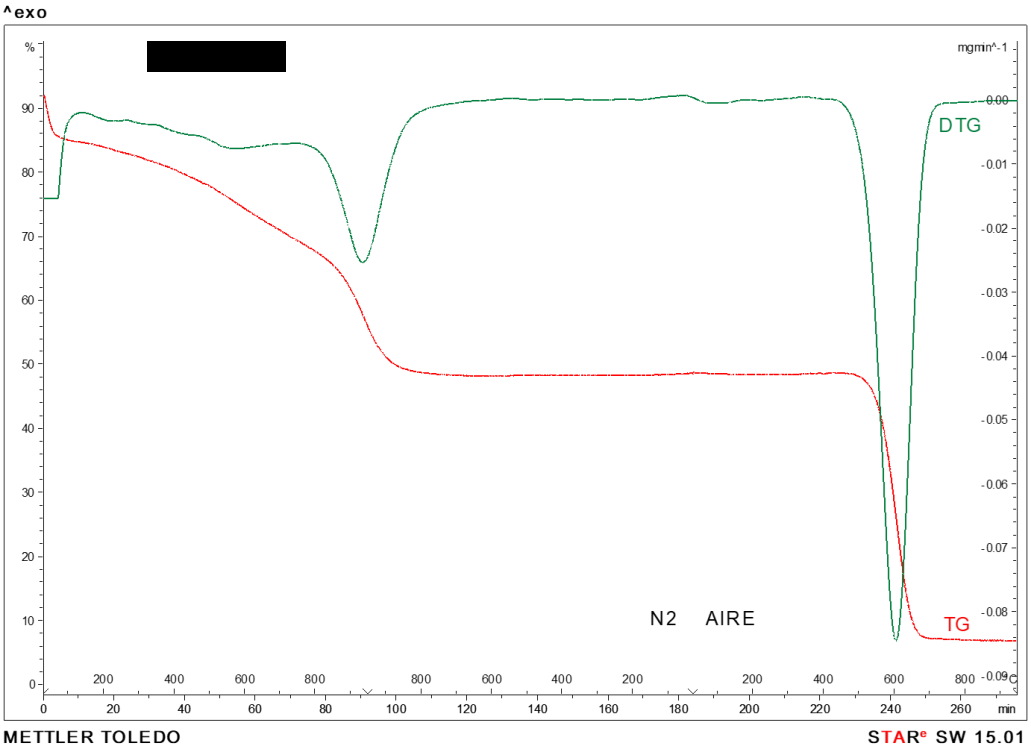
^exo
%
mg/min^-1
DTG
TG
N2 AIRE
METTLER TOLEDO
STARe SW 15.01

(b)

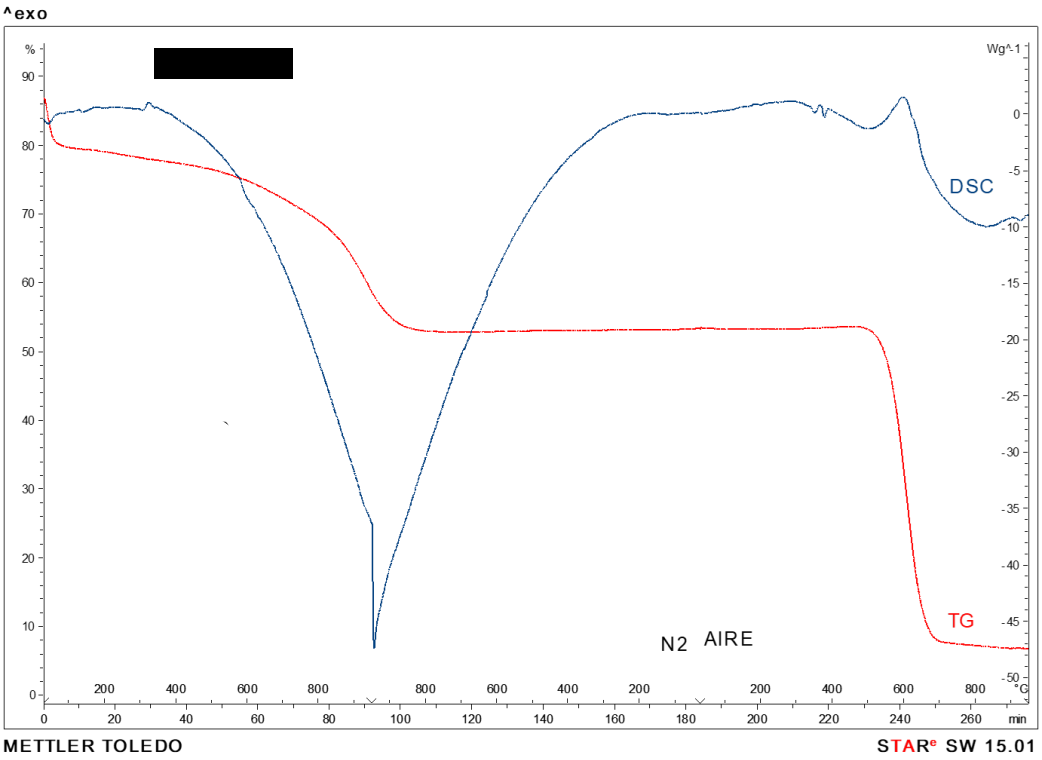
^exo
%
Wg^-1
DSC
TG
N2 AIRE
METTLER TOLEDO
STARe SW 15.01

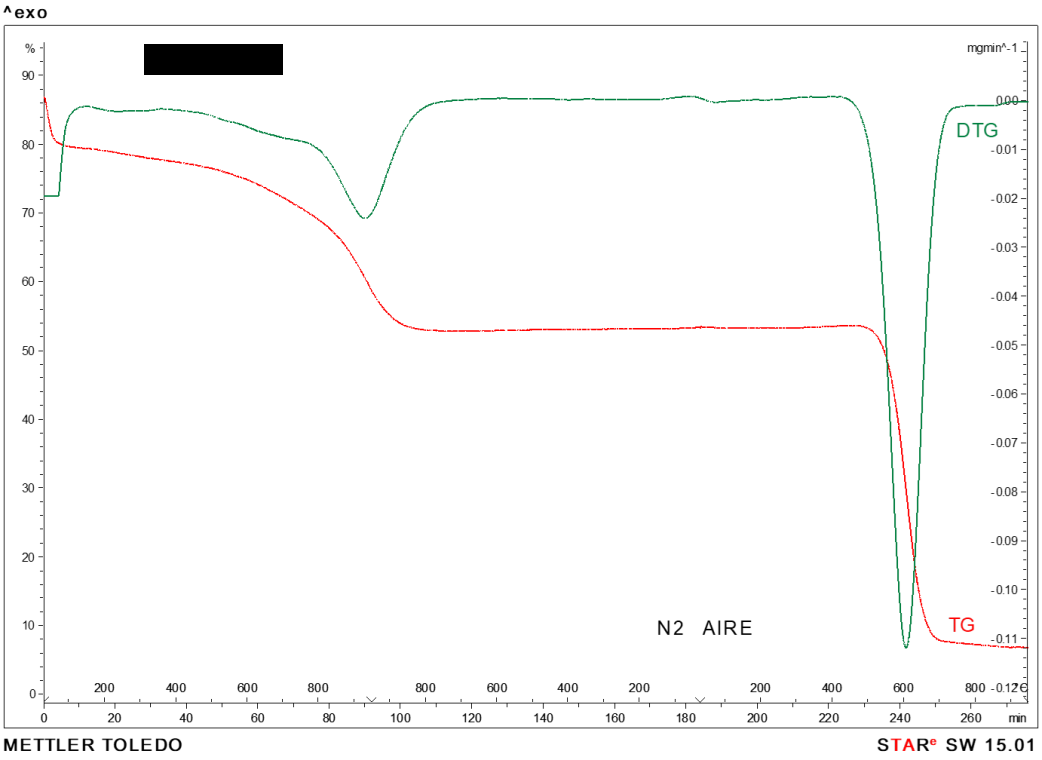

(c)

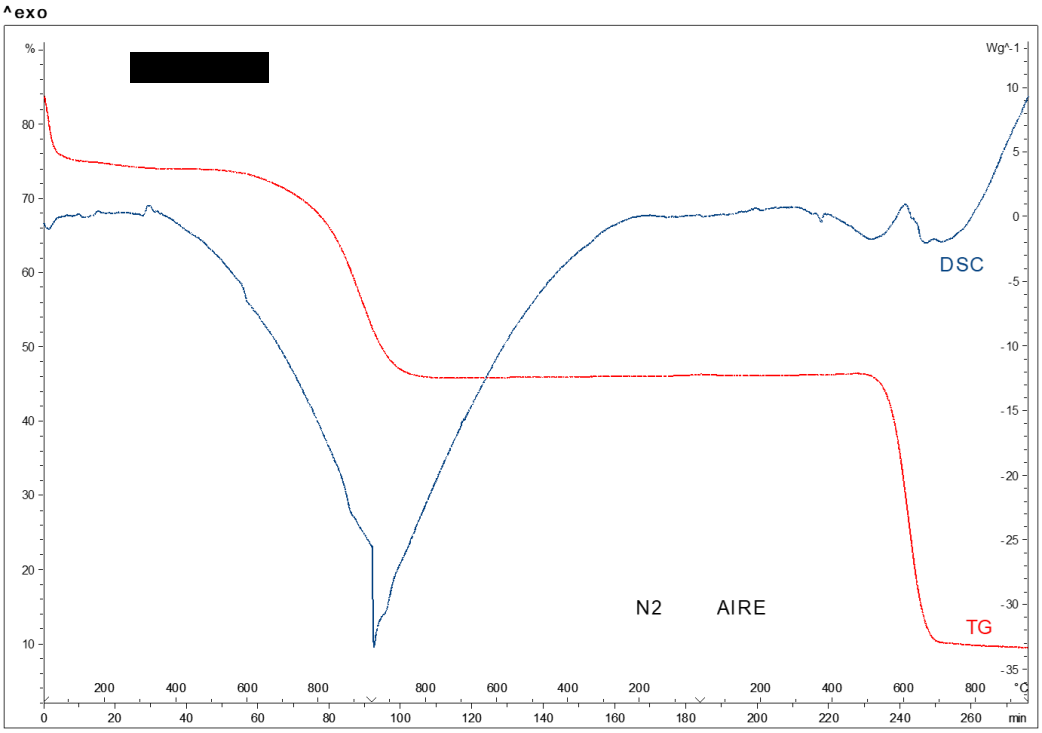
^exo
%
Wg^-1
DSC
N2
AIRE
TG
°C
min
METTLER TOLEDO
STARe SW 15.01

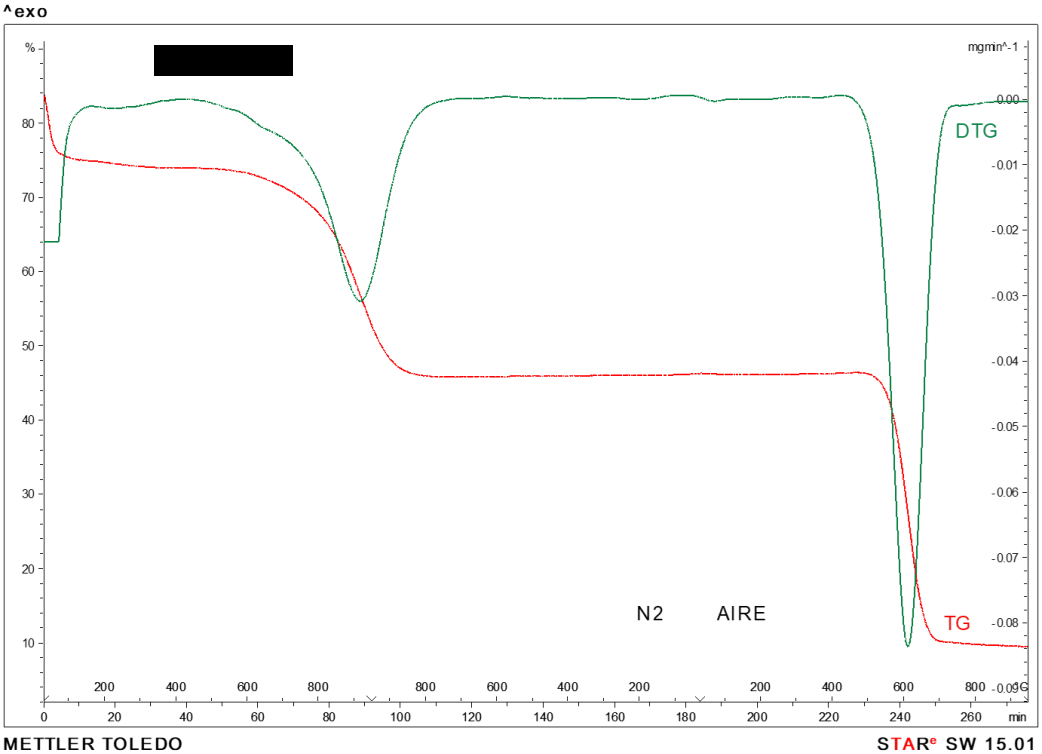
^exo
%
mgmin^-1
DTG
N2
AIRE
TG
min
METTLER TOLEDO
STARe SW 15.01

(d)

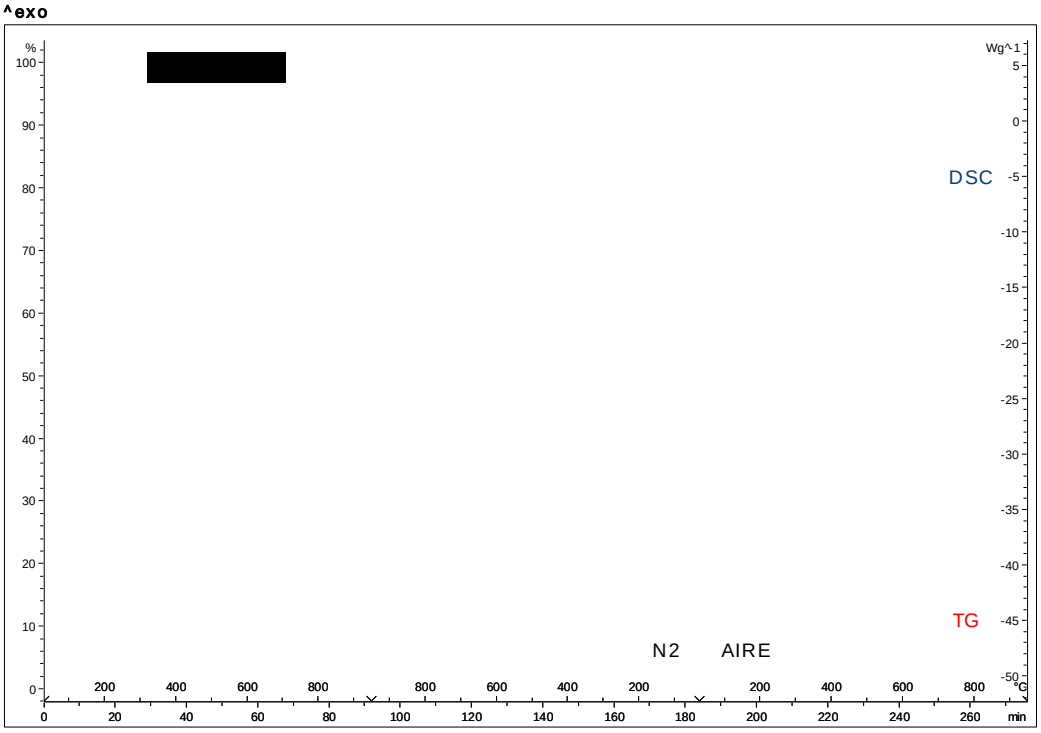
^exo
%
Wg^-1
DSC
TG
N2
AIRE
°C
min
METTLER TOLEDO
STARe SW 15.01

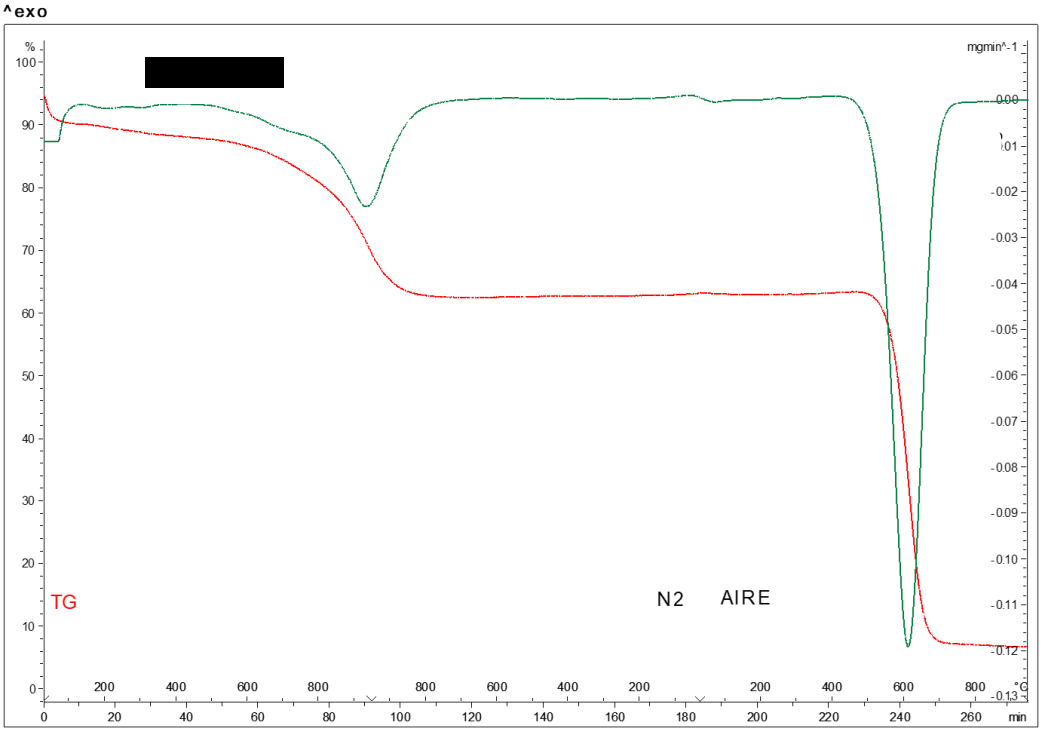
^exo
%
mgmin^-1
TG
N2
AIRE
°C
min
METTLER TOLEDO
STARe SW 15.01

(e)

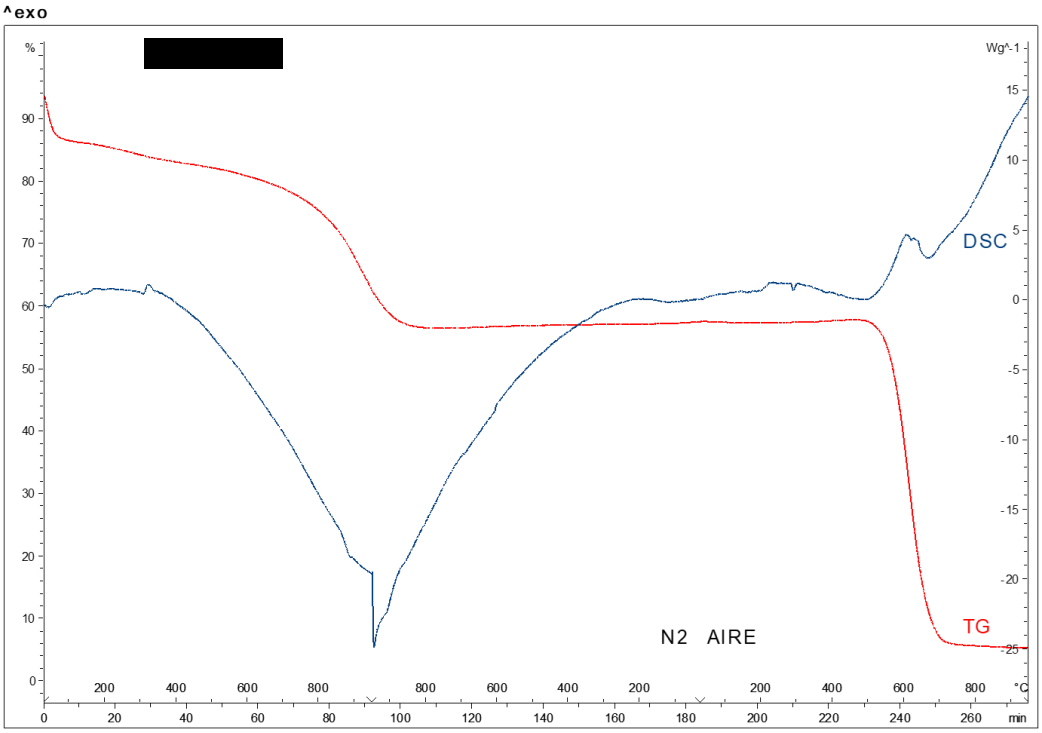
^exo
[redacted]
%
Wg^-1
DSC
TG
N2 AIRE
°C
min
METTLER TOLEDO
STARe SW 15.01

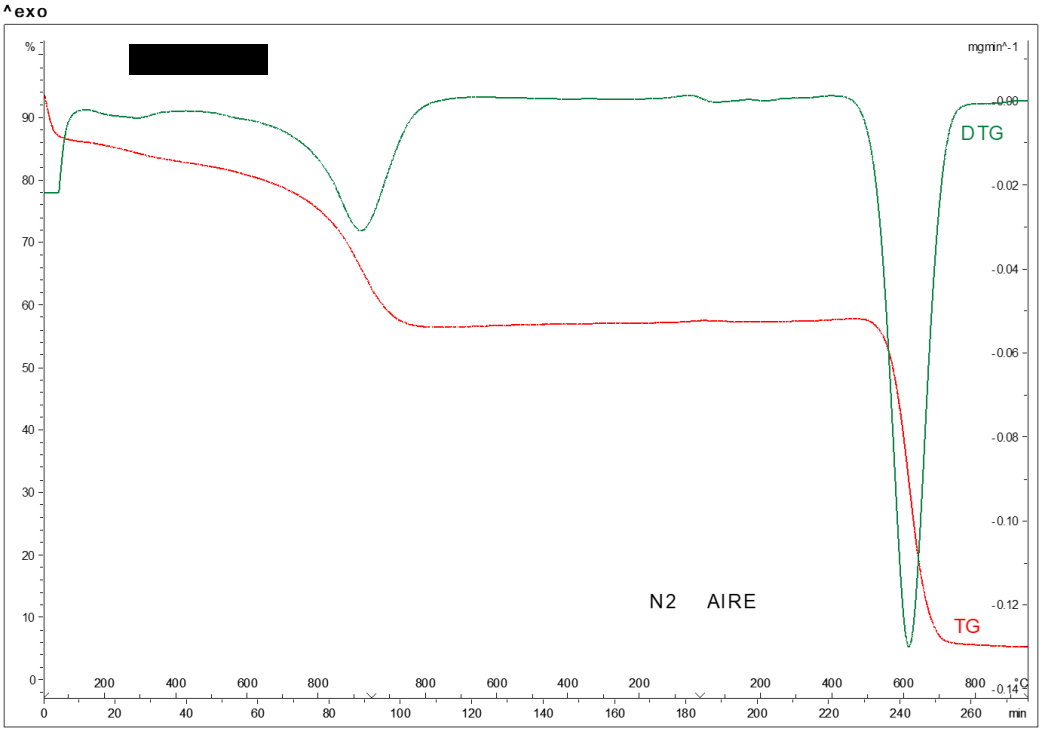
^exo
[redacted]
%
mgmin^-1
DTG
TG
N2 AIRE
°C
min
METTLER TOLEDO
STARe SW 15.01

(f)

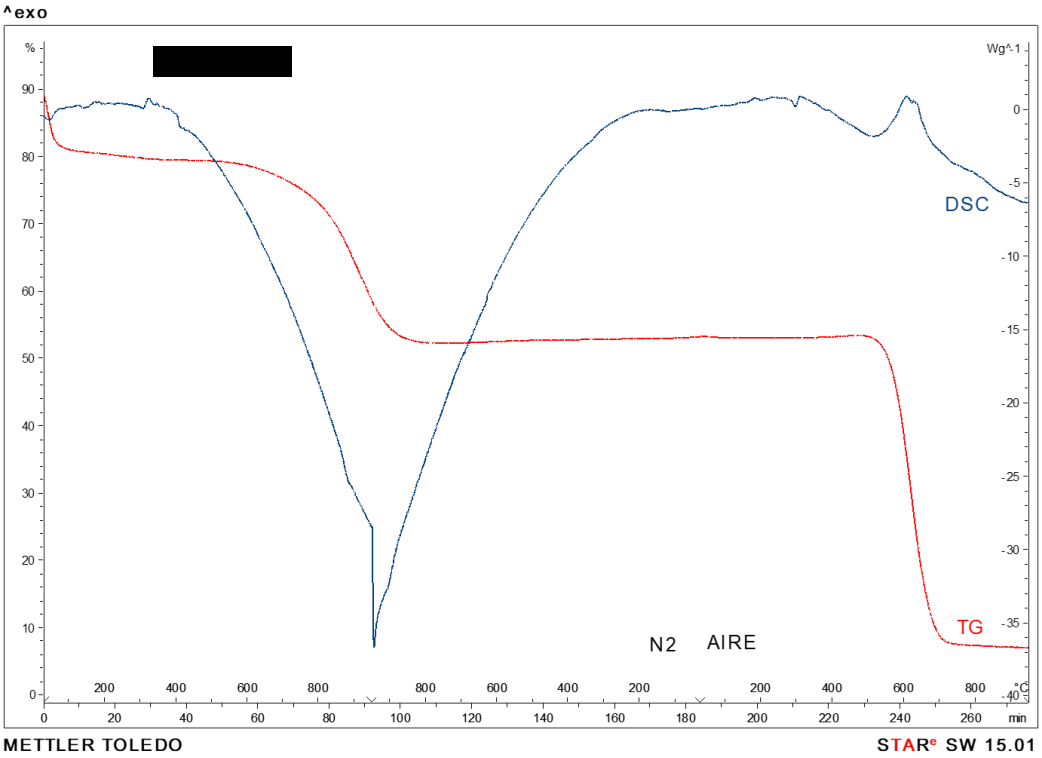
^exo
%
Wg^-1
DSC
TG
N2
AIRE
°C
min
METTLER TOLEDO
STARe SW 15.01

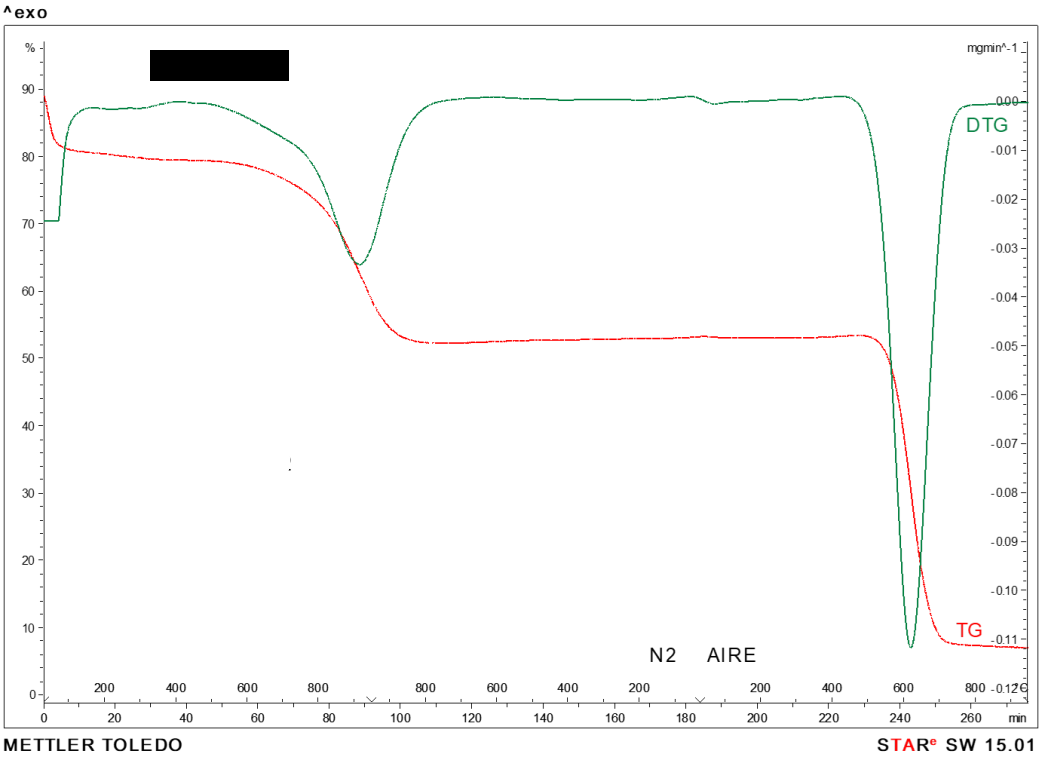
^exo
%
mgmin^-1
DTG
TG
N2
AIRE
°C
min
METTLER TOLEDO
STARe SW 15.01

(g)

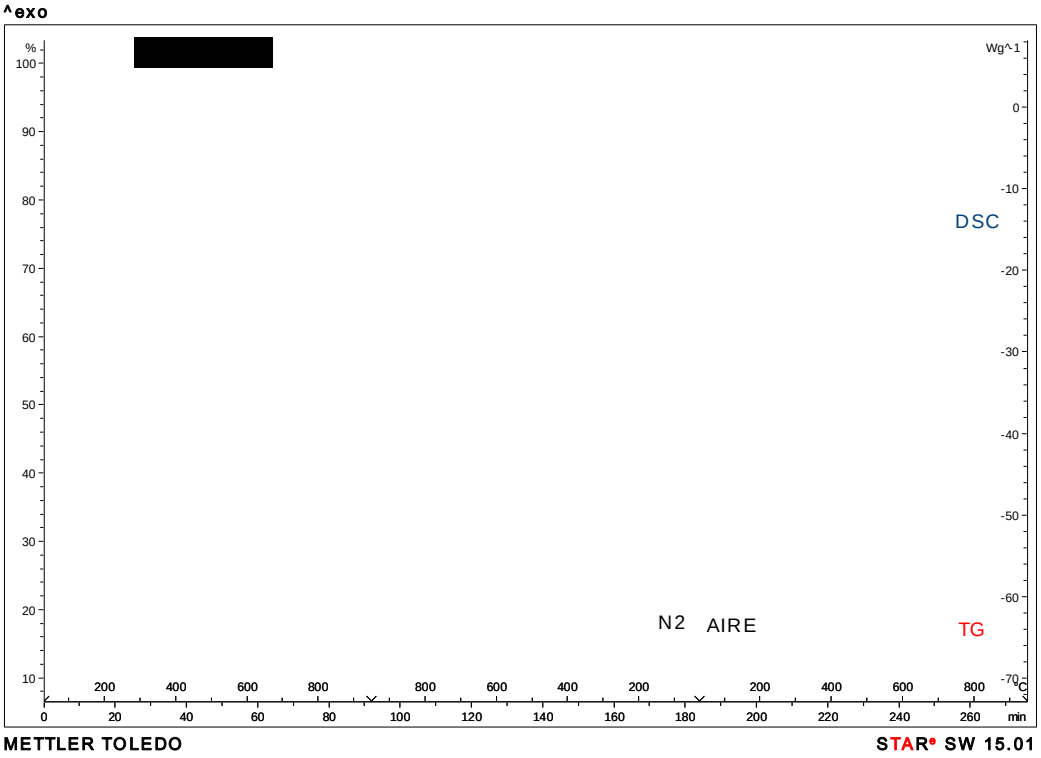
^exo
%
100
90
80
70
60
50
40
30
20
10
Wg^-1
0
-10
-20
-30
-40
-50
-60
-70
DSC
N2 AIRE
TG
200 400 600 800 800 600 400 200 200 400 600 800
°C
0 20 40 60 80 100 120 140 160 180 200 220 240 260
min
METTLER TOLEDO
STARe SW 15.01

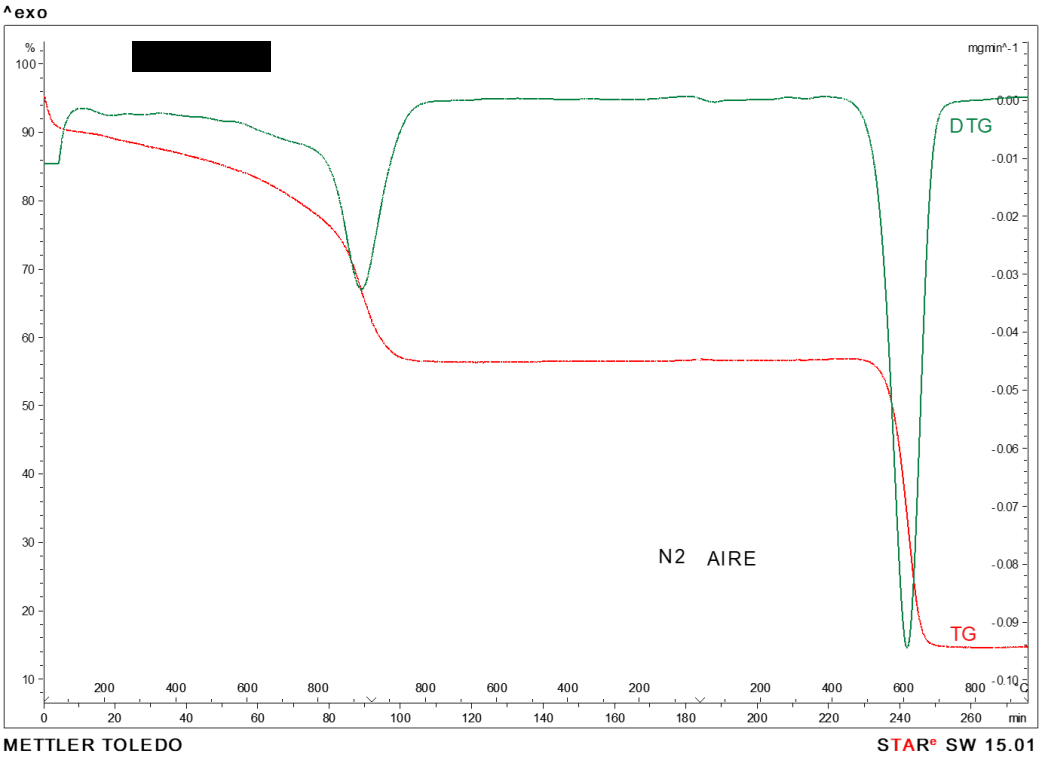
^exo
%
100
90
80
70
60
50
40
30
20
10
mg/min^-1
0.00
-0.01
-0.02
-0.03
-0.04
-0.05
-0.06
-0.07
-0.08
-0.09
-0.10
DTG
N2 AIRE
TG
200 400 600 800 800 600 400 200 200 400 600 800
°C
0 20 40 60 80 100 120 140 160 180 200 220 240 260
min
METTLER TOLEDO
STARe SW 15.01

(h)

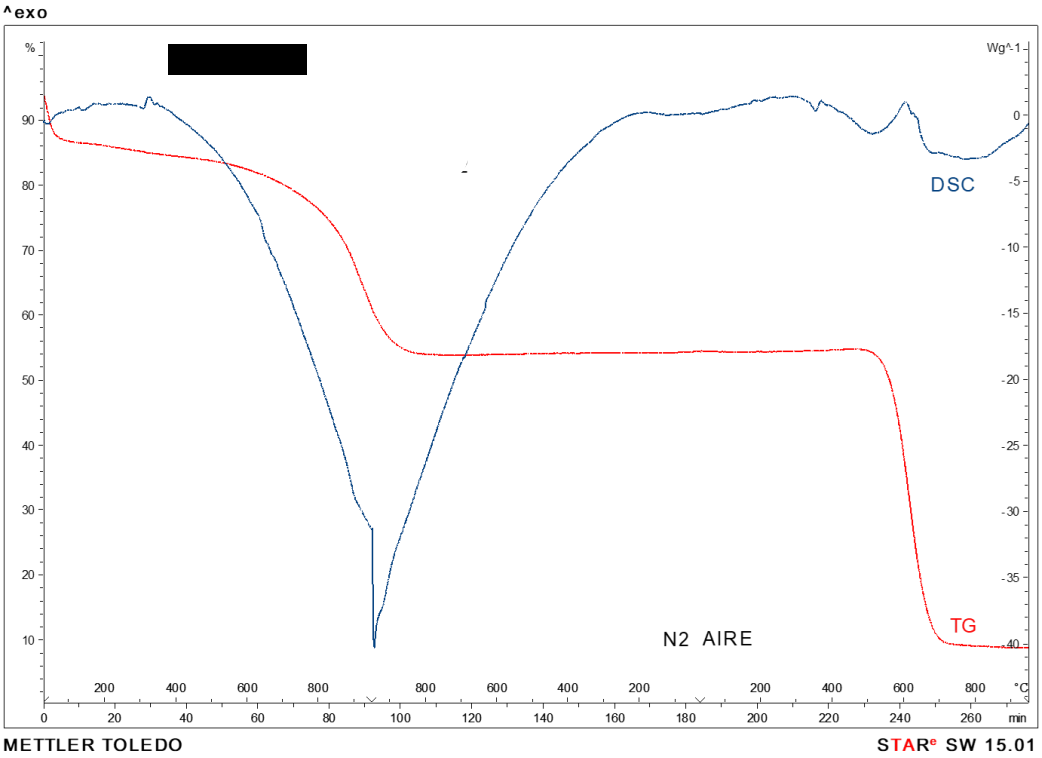
^exo
%
Wg^-1
DSC
TG
N2 AIRE
°C
min
METTLER TOLEDO
STARe SW 15.01

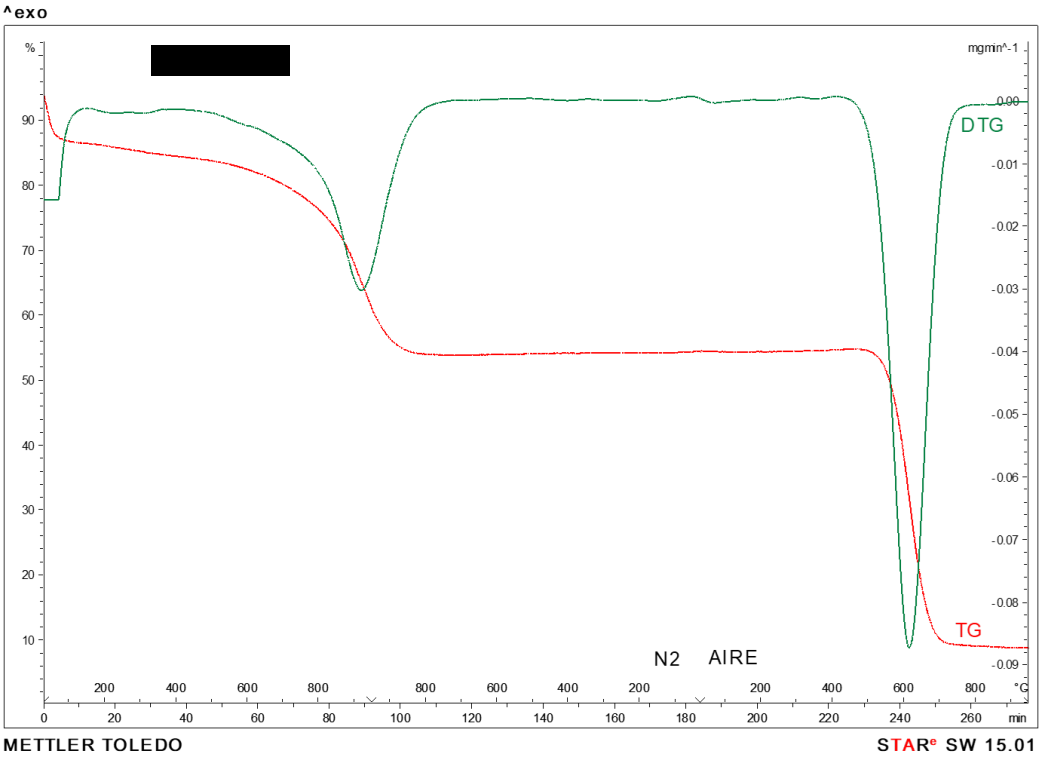
^exo
%
mg/min^-1
DTG
TG
N2 AIRE
°C
min
METTLER TOLEDO
STARe SW 15.01

(i)

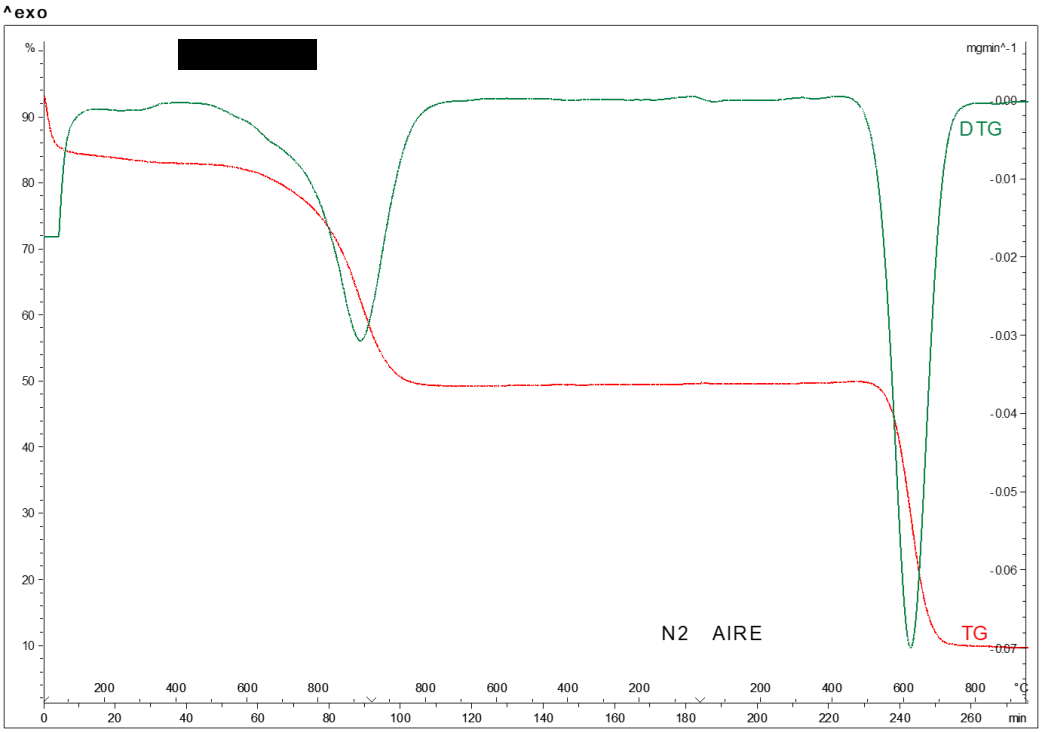
^exo
%
mgmin^-1
DTG
TG
N2 AIRE
°C
min
METTLER TOLEDO
STARe SW 15.01

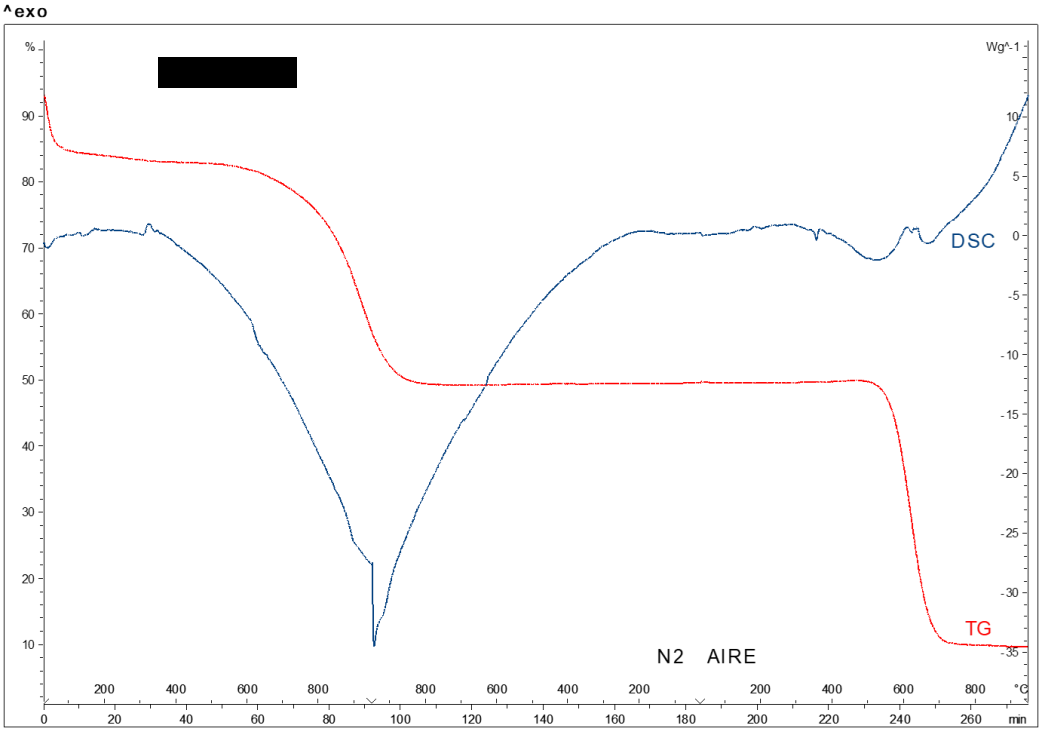
^exo
%
Wg^-1
DSC
TG
N2 AIRE
°C
min
METTLER TOLEDO
STARe SW 15.01

- 2) X-ray diffraction patterns of TiLAC catalysts, (a) TiLAC-9/1–250 °C, (b) TiLAC-9/1–300 °C, and (c) TiLAC-9/1–350 °C heat-treated at different temperatures.

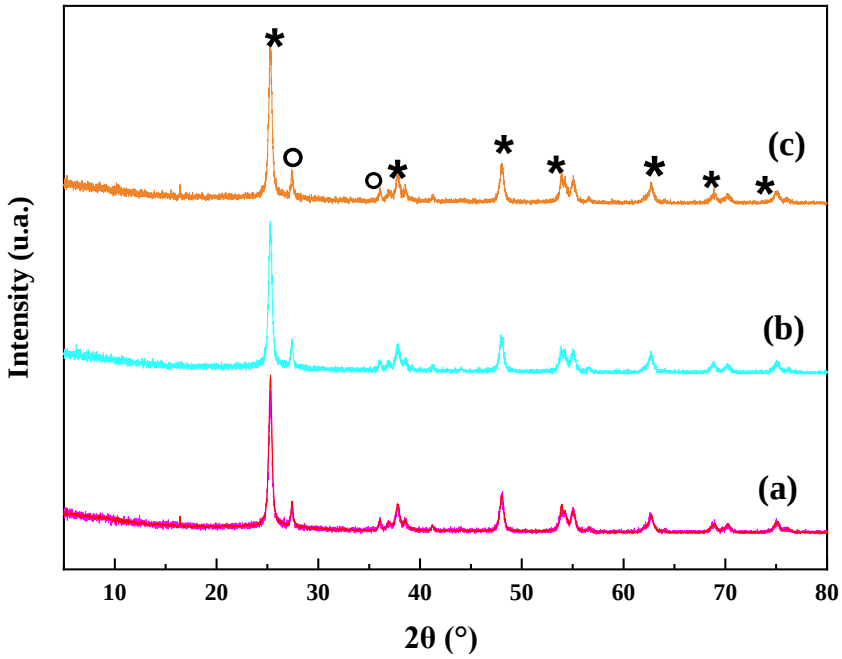

- 4) UV-vis spectrum variation of MG solutions recovered at different times during the photodegradation experiments.

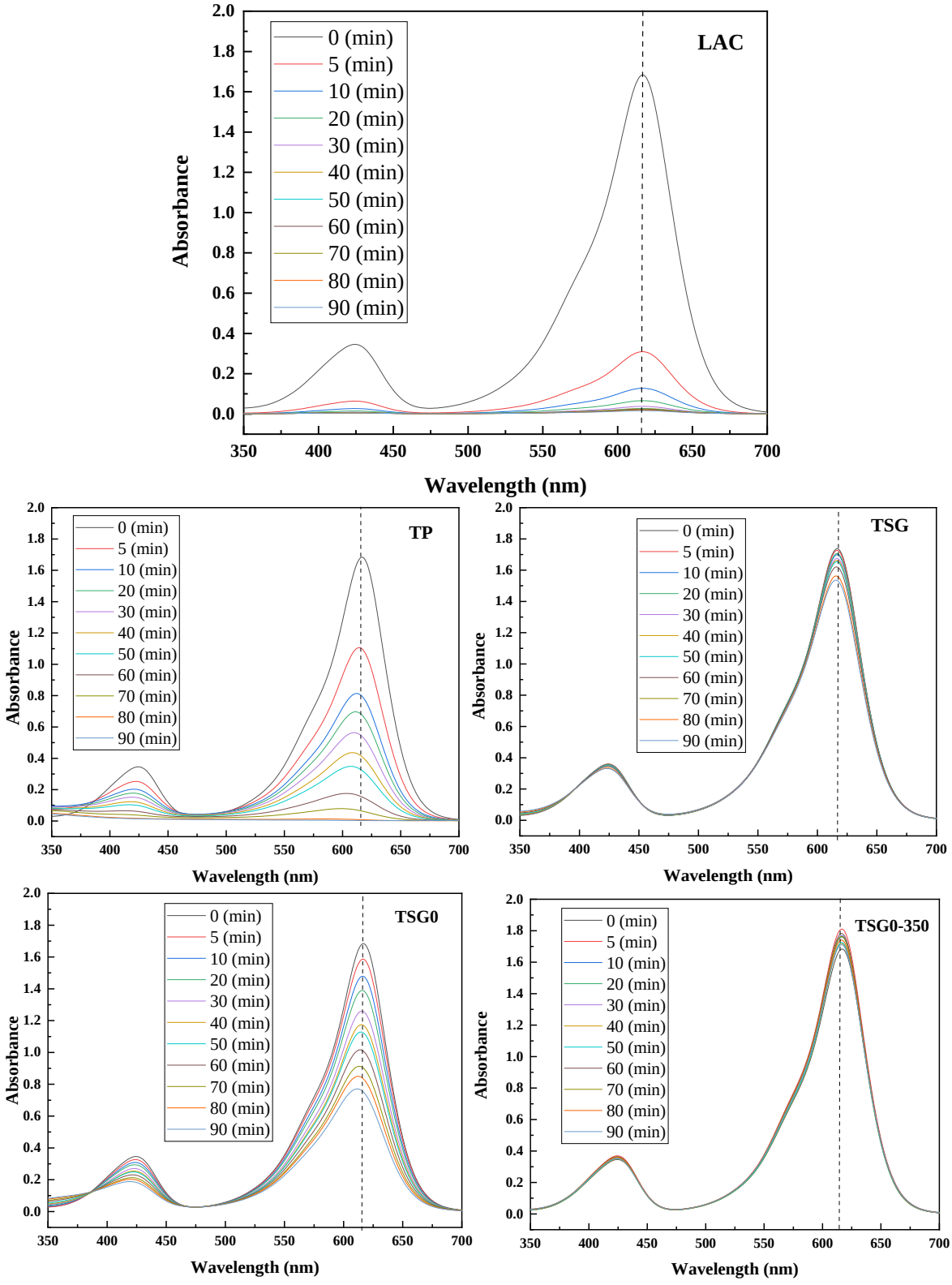

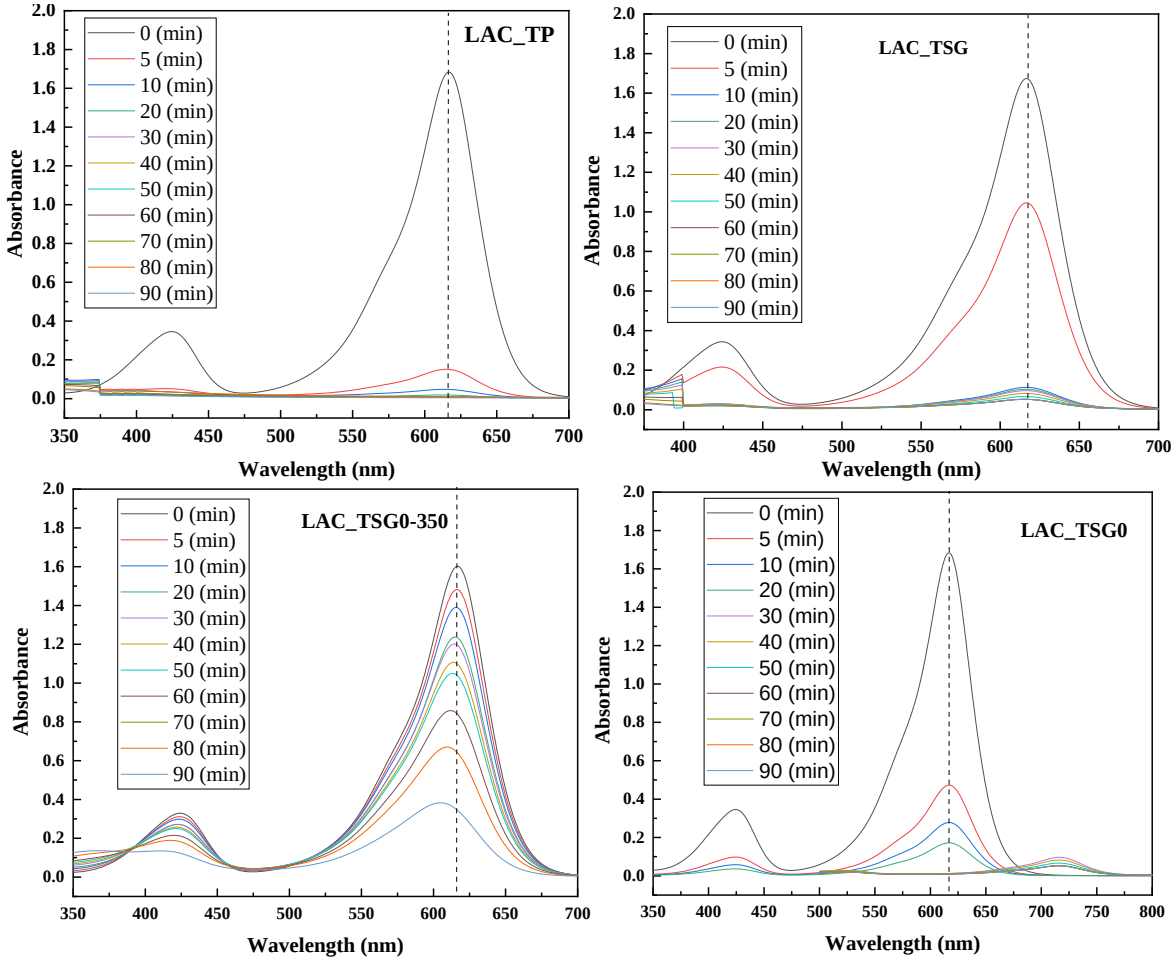
LAC_TP
LAC_TSG
LAC_TSG0-350
LAC_TSG0
0 (min)
5 (min)
10 (min)
20 (min)
30 (min)
40 (min)
50 (min)
60 (min)
70 (min)
80 (min)
90 (min)
Absorbance
Wavelength (nm)

REFERENCES

REFERENCES

[1] F. Joseph, Y.K. Agrawal, D. Rawtani, Behavior of malachite green with different adsorption matrices, Front. Life Sci. 7 (2013) 99–111. https://doi.org/10.1080/21553769.2013.803210.

[2] R. Ahmad, R. Kumar, Adsorption studies of hazardous malachite green onto treated ginger waste, J. Environ. Manage. 91 (2010) 1032–1038. https://doi.org/10.1016/j.jenvman.2009.12.016.

[3] S. Srivastava, R. Sinha, D. Roy, Toxicological effects of malachite green, Aquat. Toxicol. 66 (2004) 319–329. https://doi.org/10.1016/j.aquatox.2003.09.008.

[4] A.A. El-Zahhar, N.S. Awwad, Removal of malachite green dye from aqueous solutions using organically modified hydroxyapatite, J. Environ. Chem. Eng. 4 (2016) 633–638. https://doi.org/10.1016/j.jece.2015.12.014.

[5] C.J. Cooksey, Quirks of dye nomenclature. 6. Malachite green, Biotech. Histochem. 91 (2016) 438–444. https://doi.org/10.1080/10520295.2016.1209787.

[6] T. Velpandian, K. Saha, A.K. Ravi, S.S. Kumari, N.R. Biswas, S. Ghose, Ocular hazards of the colors used during the festival-of-colors (Holi) in India-Malachite green toxicity, J. Hazard. Mater. 139 (2007) 204–208. https://doi.org/10.1016/j.jhazmat.2006.06.046.

[7] O.S. Bello, M.A. Ahmad, B. Semire, Scavenging malachite green dye from aqueous solutions using pomelo (Citrus grandis) peels: kinetic, equilibrium and thermodynamic studies, Desalin. Water Treat. 56 (2015) 521–535. https://doi.org/10.1080/19443994.2014.940387.

[8] Z. Lin, D. Wang, H. Zhang, L. Li, Z. Huang, J. Shen, Y. Lin, Extraction and determination of malachite green from aquatic products based on molecularly imprinted polymers, Sep. Sci. Technol. 51 (2016) 1684–1689. https://doi.org/10.1080/01496395.2016.1175478.

[9] A.K. Das, S. Saha, A. Pal, S.K. Maji, Surfactant-modified alumina: An efficient adsorbent for malachite green removal from water environment, J. Environ. Sci. Heal. - Part A Toxic/Hazardous Subst. Environ. Eng. 44 (2009) 896–905. https://doi.org/10.1080/10934520902958708.

[10] Z.H. Farooqi, H. Sultana, R. Begum, M. Usman, M. Ajmal, J. Nisar, A. Irfan, M. Azam, Catalytic degradation of malachite green using a crosslinked colloidal polymeric system loaded with silver nanoparticles, Int. J. Environ. Anal. Chem. (2020). https://doi.org/10.1080/03067319.2020.1779247.

[11] E.M. Calvo-Muñoz, F.J. García-Mateos, J.M. Rosas, J. Rodríguez-Mirasol, T. Cordero, Biomass waste carbon materials as adsorbents for CO 2 capture under post-combustion conditions, Front. Mater. 3 (2016) 1–14. https://doi.org/10.3389/fmats.2016.00023.

[12] G.J.F. Cruz, M.M. Gómez, J.L. Solis, J. Rimaycuna, R.L. Solis, J.F. Cruz, B.

Rathnayake, R.L. Keiski, Composites of ZnO nanoparticles and biomass based activated carbon: adsorption, photocatalytic and antibacterial capacities, Water Sci. Technol. 2017 (2018) 492–508. https://doi.org/http://dx.doi.org/10.2166/wst.2018.176.

[13] J. Li, Z. Ren, Y. Ren, L. Zhao, S. Wang, J. Yu, Activated carbon with micrometer-scale channels prepared from luffa sponge fibers and their application for supercapacitors, RSC Adv. 4 (2014) 35789–35796. https://doi.org/10.1039/c4ra04073b.

[14] T. XU, X. LIU, Peanut Shell Activated Carbon: Characterization, Surface Modification and Adsorption of Pb2+ from Aqueous Solution, Chinese J. Chem. Eng. 16 (2008) 401–406. https://doi.org/10.1016/S1004-9541(08)60096-8.

[15] A. Bhatnagar, I. Anastopoulos, Adsorptive removal of bisphenol A (BPA) from aqueous solution: A review, Chemosphere. 168 (2017) 885–902. https://doi.org/10.1016/j.chemosphere.2016.10.121.

[16] R.C. Bansal, M. Goyal, Activated carbon adsorption, CRC press, 2005.

[17] V. Hernández, Lignocellulosic Precursors Used in the Synthesis of Activated Carbon - Characterization Techniques and Applications in the Wastewater Treatment, InTech, 2012. https://doi.org/10.5772/3346.

[18] X. Wang, J. Zhou, S. Zhao, X. Chen, Y. Yu, Synergistic effect of adsorption and visible-light photocatalysis for organic pollutant removal over BiVO4/carbon sphere nanocomposites, Appl. Surf. Sci. 453 (2018) 394–404. https://doi.org/https://doi.org/10.1016/j.apsusc.2018.05.073.

[19] J.R. Regalbuto, A scientific method to prepare supported metal catalysts, in: R. Richards (Ed.), Surf. Nanomolecular Catal., CRC Press, 2006: pp. 161–194. https://doi.org/10.1201/9781420015751.

[20] W. Zhang, Y. Huang, P. Liu, Y. Zhao, H. Wu, M. Guan, H. Zhang, TiO2 supported on bamboo charcoal for H2O 2-assisted pollutant degradation under solar light, Mater. Sci. Semicond. Process. 17 (2014) 124–128. https://doi.org/10.1016/j.mssp.2013.08.014.

[21] J.R. Guimarães, M. Guedes Maniero, R. Nogueira de Araújo, A comparative study on the degradation of RB-19 dye in an aqueous medium by advanced oxidation processes, J. Environ. Manage. 110 (2012) 33–39. https://doi.org/10.1016/j.jenvman.2012.05.020.

[22] H. Kisch, Semiconductor Photocatalysis Principles and Applications, Wiley-VCH Verlag GmbH & Co., 2015. http://library1.nida.ac.th/termpaper6/sd/2554/19755.pdf.

[23] P. Bansal, N. Bhullar, D. Sud, Studies on photodegradation of malachite green using TiO2/ZnO photocatalyst, Desalin. Water Treat. 12 (2009) 108–113. https://doi.org/10.5004/dwt.2009.944.

[24] X. Gao, Z. Wang, X. Zhai, F. Fu, W. Li, The synthesize of lanthanide doped

BiVO4 and its enhanced photocatalytic activity, J. Mol. Liq. 211 (2015) 25–30. https://doi.org/10.1016/j.molliq.2015.06.058.

[25] L.S. Reddy, Y.H. Ko, J.S. Yu, Hydrothermal Synthesis and Photocatalytic Property of β-Ga2O3 Nanorods, Nanoscale Res. Lett. 10 (2015). https://doi.org/10.1186/s11671-015-1070-5.

[26] J. Araña, J.M. Doña-Rodríguez, E. Tello Rendón, C. Garriga I Cabo, O. González-Díaz, J.A. Herrera-Melián, J. Pérez-Peña, G. Colón, J.A. Navío, TiO2 activation by using activated carbon as a support: Part I. Surface characterisation and decantability study, Appl. Catal. B Environ. 44 (2003) 161–172. https://doi.org/10.1016/S0926-3373(03)00107-3.

[27] L. Cano-Casanova, A. Amorós-Pérez, M.Á. Lillo-Ródenas, M. del C. Román-Martínez, Effect of the preparation method (sol-gel or hydrothermal) and conditions on the TiO2 properties and activity for propene oxidation, Materials (Basel). 11 (2018). https://doi.org/10.3390/ma11112227.

[28] L.G. Devi, R. Kavitha, Enhanced photocatalytic activity of sulfur doped TiO2 for the decomposition of phenol: A new insight into the bulk and surface modification, Mater. Chem. Phys. 143 (2014) 1300–1308. https://doi.org/10.1016/j.matchemphys.2013.11.038.

[29] M.S. Lucas, P.B. Tavares, J.A. Peres, J.L. Faria, M. Rocha, C. Pereira, C. Freire, Photocatalytic degradation of Reactive Black 5 with TiO2-coated magnetic nanoparticles, Catal. Today. 209 (2013) 116–121. https://doi.org/10.1016/j.cattod.2012.10.024.

[30] Z.A. Che Ramli, N. Asim, W.N.R.W. Isahak, Z. Emdadi, N. Ahmad-Ludin, M.A. Yarmo, K. Sopian, Photocatalytic degradation of methylene blue under UV light irradiation on prepared carbonaceous TiO2, Sci. World J. 2014 (2014) 13–15. https://doi.org/10.1155/2014/415136.

[31] A. Morawski, M. Janus, B. Tryba, M. Toyoda, T. Tsumura, M. Inagaki, Carbon modified TiO_2 photocatalysts for water purification, Polish J. Chem. Technol. 11 (2009) 46–50. https://doi.org/10.2478/v10026-009-0023-0.

[32] A.B. Lavand, M.N. Bhatu, Y.S. Malghe, Visible light photocatalytic degradation of malachite green using modified titania, J. Mater. Res. Technol. 8 (2019) 299–308. https://doi.org/10.1016/j.jmrt.2017.05.019.

[33] J.G. Speight, HANDBOOK OF COAL ANALYSIS, 2nd Editio, John Wiley & Sons, Inc, Hoboken, New Jersey, 2015. https://doi.org/10.1002/9781119037699.

[34] T.J. Bandosz, Activated Carbon Surfaces in Environmental Remediation (Interface Science and Technology), Academic Press, London, UK, 2006.

[35] X. Duan, C. Srinivasakannan, X. Wang, F. Wang, X. Liu, Synthesis of activated carbon fibers from cotton by microwave induced H3PO4 activation, J. Taiwan Inst. Chem. Eng. 70 (2017) 374–381. https://doi.org/10.1016/j.jtice.2016.10.036.

[36] K.Y. Foo, B.H. Hameed, Mesoporous activated carbon from wood sawdust by

K2CO3 activation using microwave heating, Bioresour. Technol. 111 (2012) 425–432. https://doi.org/https://doi.org/10.1016/j.biortech.2012.01.141.

[37] D. Das, D.P. Samal, M. BC, Preparation of Activated Carbon from Green Coconut Shell and its Characterization, J. Chem. Eng. Process Technol. 06 (2015). https://doi.org/10.4172/2157-7048.1000248.

[38] M. Ahmedna, W.E. Marshall, R.M. Rao, Production of granular activated carbons from select agricultural by-products and evaluation of their physical, chemical and adsorption properties, Bioresour. Technol. 71 (2000) 113–123. https://doi.org/10.1016/S0960-8524(99)00070-X.

[39] P.L. Walker, Active carbon. manufacture, properties and applications: M. Smí{\vs}ek and S. Cerný. Elsevier Publishing Company, New York (1970), xii + 479 pp, Carbon N. Y. 9 (1971) 531.

[40] J.W. Hassler, Activated Carbon by Hassler J.W. (z-lib.org).pdf, (1963) 411. 262-278-265-9.

[41] P.T. Moseley, D.A.J. Rand, A. Davidson, B. Monahov, Understanding the functions of carbon in the negative active-mass of the lead–acid battery: A review of progress, J. Energy Storage. 19 (2018) 272–290. https://doi.org/10.1016/j.est.2018.08.003.

[42] J.R. Perrich, Activated Carbon Adsorption for Wastewater Treatment, 2018. https://doi.org/10.1201/9781351069465.

[43] M. Thommes, K. Kaneko, A. V. Neimark, J.P. Olivier, F. Rodriguez-Reinoso, J. Rouquerol, K.S.W. Sing, Physisorption of gases, with special reference to the evaluation of surface area and pore size distribution (IUPAC Technical Report), Pure Appl. Chem. 87 (2015) 1051–1069. https://doi.org/10.1515/pac-2014-1117.

[44] T.J. Kemp, A brief 100 year history of carbon, Sci. Prog. 100 (2017) 293–298. https://doi.org/10.3184/003685017X14994318577435.

[45] M.M. Dubinin, G.M. Plavnik, Microporous structures of carbonaceous adsorbents, Carbon N. Y. 6 (1968) 183–192. https://doi.org/https://doi.org/10.1016/0008-6223(68)90302-3.

[46] B.S. Girgis, S.S. Yunis, A.M. Soliman, Characteristics of activated carbon from peanut hulls in relation to conditions of preparation, Mater. Lett. 57 (2002) 164–172. https://doi.org/10.1016/S0167-577X(02)00724-3.

[47] D.K. Ludlow, Activated Carbon Adsorption By Roop Chand Bansal and Meenakshi Goyal (Panjab University, Chandigarh, India). CRC Press (an imprint of Taylor and Francis Group): Boca Raton, FL. 2005. xxii + 498 pp. $189.95. ISBN 0-8247-5344-5, J. Am. Chem. Soc. 128 (2006) 10630. https://doi.org/10.1021/ja059874h.

[48] S. Lowell, J. Shields, M.A. Thomas, M. Thommes, Characterization of Porous Solids and Powders: Surface Area, Pore Size and Density, in: 2006.

[49] J.M. Valente Nabais, C. Laginhas, M.M.L. Ribeiro Carrott, P.J.M. Carrott, J.E. Crespo Amorós, A. V Nadal Gisbert, Surface and porous characterisation of activated carbons made from a novel biomass precursor, the esparto grass, Appl. Surf. Sci. 265 (2013) 919–924. https://doi.org/10.1016/j.apsusc.2012.11.164.

[50] J.A. Menéndez-Díaz, I. Martín-Gullón, Chapter 1 Types of carbon adsorbents and their production, Interface Sci. Technol. 7 (2006) 1–47. https://doi.org/10.1016/S1573-4285(06)80010-4.

[51] S.S. Xu, S.W. Qiu, Z.Y. Yuan, T.Z. Ren, T.J. Bandosz, Nitrogen-containing activated carbon of improved electrochemical performance derived from cotton stalks using indirect chemical activation, J. Colloid Interface Sci. 540 (2019) 285–294. https://doi.org/10.1016/j.jcis.2019.01.031.

[52] J.M. Rosas, R. Ruiz-Rosas, J. Rodríguez-Mirasol, T. Cordero, Kinetic study of the oxidation resistance of phosphorus-containing activated carbons, Carbon N. Y. 50 (2012) 1523–1537. https://doi.org/10.1016/j.carbon.2011.11.030.

[53] H. Marsh, F. Rodríguez-Reinoso, Characterization of Activated Carbon, in: H. Marsh, F. Rodríguez-Reinoso (Eds.), Act. Carbon, Elsevier Science Ltd, Oxford, 2006: pp. 143–242. https://doi.org/https://doi.org/10.1016/B978-008044463-5/50018-2.

[54] F.J.F.J. García-Mateos, I. Moulefera, J.M.J.M. Rosas, A. Benyoucef, J. Rodríguez-Mirasol, T. Cordero, Alcohol dehydrogenation on kraft Lignin-derived chars with surface basicity, Catalysts. 7 (2017). https://doi.org/10.3390/catal7100308.

[55] P. Serp, J.L. Figueiredo, Carbon materials for catalysis, A JOHN WILEY & SONS, INC., PUBLICATION, 2009.

[56] J.L. Figueiredo, M.F.R. Pereira, M.M.A. Freitas, J.J.M. Órfão, Modification of the surface chemistry of activated carbons, Carbon N. Y. 37 (1999) 1379–1389. https://doi.org/10.1016/S0008-6223(98)00333-9.

[57] A.M. Puziy, O.I. Poddubnaya, A. Martínez-Alonso, F. Suárez-García, J.M.D. Tascón, J.M.D. Tascó, Surface chemistry of phosphorus-containing carbons of lignocellulosic origin, Carbon N. Y. 43 (2005) 2857–2868. https://doi.org/10.1016/j.carbon.2005.06.014.

[58] J.J. Ternero-Hidalgo, J.M. Rosas, J. Palomo, M.J. Valero-Romero, J. Rodríguez-Mirasol, T. Cordero, Functionalization of activated carbons by HNO3 treatment: Influence of phosphorus surface groups, Carbon N. Y. 101 (2016) 409–419. https://doi.org/10.1016/j.carbon.2016.02.015.

[59] I. Velo-Gala, J.J. López-Peñalver, M. Sánchez-Polo, J. Rivera-Utrilla, Surface modifications of activated carbon by gamma irradiation, Carbon N. Y. 67 (2014) 236–249. https://doi.org/10.1016/J.CARBON.2013.09.087.

[60] M. Dusselier, S. Van De Vyver, E.C. Company, L. Peng, ChemInform Abstract : Tailoring Nanohybrids and Nanocomposites for Catalytic Applications Cutting-edge research for a greener sustainable future, (2013).

https://doi.org/10.1039/C3GC37141G.

[61] B. Cagnon, X. Py, A. Guillot, F. Stoeckli, G. Chambat, Contributions of hemicellulose, cellulose and lignin to the mass and the porous properties of chars and steam activated carbons from various lignocellulosic precursors, Bioresour. Technol. 100 (2009) 292–298. https://doi.org/10.1016/j.biortech.2008.06.009.

[62] K. Sun, J. chun Jiang, Preparation and characterization of activated carbon from rubber-seed shell by physical activation with steam, Biomass and Bioenergy. 34 (2010) 539–544. https://doi.org/10.1016/j.biombioe.2009.12.020.

[63] N. Mohamad Nor, L.C. Lau, K.T. Lee, A.R. Mohamed, L. Lee Chung, L. Keat Teong, A. Rahman Mohamed, Synthesis of activated carbon from lignocellulosic biomass and its applications in air pollution control - A review, J. Environ. Chem. Eng. 1 (2013) 658–666. https://doi.org/10.1016/j.jece.2013.09.017.

[64] I. Ghouma, M. Jeguirim, S. Dorge, L. Limousy, C. Matei Ghimbeu, A. Ouederni, Activated carbon prepared by physical activation of olive stones for the removal of NO2 at ambient temperature, Comptes Rendus Chim. 18 (2015) 63–74. https://doi.org/10.1016/j.crci.2014.05.006.

[65] F. Rodríguez-Reinoso, M. Molina-Sabio, Activated carbons from lignocellulosic materials by chemical and/or physical activation: an overview, Carbon N. Y. 30 (1992) 1111–1118. https://doi.org/10.1016/0008-6223(92)90143-K.

[66] A. Ahmadpour, D.D. Do, The preparation of active carbons from coal by chemical and physical activation, Carbon N. Y. 34 (1996) 471–479. https://doi.org/10.1016/0008-6223(95)00204-9.

[67] S. Mopoung, P. Moonsri, W. Palas, S. Khumpai, Characterization and Properties of Activated Carbon Prepared from Tamarind Seeds by KOH Activation for Fe(III) Adsorption from Aqueous Solution, Sci. World J. 2015 (2015). https://doi.org/10.1155/2015/415961.

[68] A.J. Romero-Anaya, A. Molina, P. Garcia, A.A. Ruiz-Colorado, A. Linares-Solano, C. Salinas-Martínez de Lecea, Phosphoric acid activation of recalcitrant biomass originated in ethanol production from banana plants, Biomass and Bioenergy. 35 (2011) 1196–1204. https://doi.org/10.1016/j.biombioe.2010.12.007.

[69] M. Kiliç, E. Apaydin-Varol, A.E. Pütün, Preparation and surface characterization of activated carbons from Euphorbia rigida by chemical activation with ZnCl 2 , K 2 CO 3 , NaOH and H 3 PO 4, Appl. Surf. Sci. 261 (2012) 247–254. https://doi.org/10.1016/j.apsusc.2012.07.155.

[70] M. Molina-Sabio, F. Rodríguez-Reinoso, Role of chemical activation in the development of carbon porosity, Colloids Surfaces A Physicochem. Eng. Asp. 241 (2004) 15–25. https://doi.org/10.1016/j.colsurfa.2004.04.007.

[71] Y. Kan, Q. Yue, D. Li, Y. Wu, B. Gao, Preparation and characterization of activated carbons from waste tea by H3PO4 activation in different atmospheres for oxytetracycline removal, J. Taiwan Inst. Chem. Eng. 71 (2017) 494–500.

https://doi.org/10.1016/j.jtice.2016.12.012.

[72] S.I. Mussatto, M. Fernandes, G.J.M. Rocha, J.J.M. Órfão, J.A. Teixeira, I.C. Roberto, Production, characterization and application of activated carbon from brewer's spent grain lignin, Bioresour. Technol. 101 (2009) 2450–2457. https://doi.org/10.1016/j.biortech.2009.11.025.

[73] J. Xu, L. Chen, H. Qu, Y. Jiao, J. Xie, G. Xing, Preparation and characterization of activated carbon from reedy grass leaves by chemical activation with H 3 PO 4, Appl. Surf. Sci. 320 (2014) 674–680. https://doi.org/10.1016/j.apsusc.2014.08.178.

[74] D. Prahas, Y. Kartika, N. Indraswati, S. Ismadji, Activated carbon from jackfruit peel waste by H3PO4 chemical activation: Pore structure and surface chemistry characterization, Chem. Eng. J. 140 (2008) 32–42. https://doi.org/10.1016/j.cej.2007.08.032.

[75] M. Jagtoyen, F. Derbyshire, Activated carbons from yellow poplar and white oak by H3PO4 activation, Carbon N. Y. 36 (1998) 1085–1097. https://doi.org/10.1016/S0008-6223(98)00082-7.

[76] D.N.S. Hon, N. Shiraishi, Wood and Cellulosic Chemistry, Revised, and Expanded, 2000. https://doi.org/10.1201/9781482269741.

[77] D. Prahas, Y. Kartika, N. Indraswati, S. Ismadji, Activated carbon from jackfruit peel waste by H3PO4 chemical activation: Pore structure and surface chemistry characterization, Chem. Eng. J. 140 (2008) 32–42. https://doi.org/10.1016/j.cej.2007.08.032.

[78] S. Gaspard, N. Passé-Coutrin, A. Durimel, T. Cesaire, V. Jeanne-Rose, CHAPTER 2 Activated Carbon from Biomass for Water Treatment, in: Biomass Sustain. Appl. Pollut. Remediat. Energy, The Royal Society of Chemistry, 2014: pp. 46–105. https://doi.org/10.1039/9781849737142-00046.

[79] M. Molina-Sabio, C. Almansa, F. Rodrıguez-Reinoso, Phosphoric acid activated carbon discs for methane adsorption, Carbon N. Y. 41 (2003) 2113–2119.

[80] M. Jagtoyen, F. Derbyshire, Some considerations of the origins of porosity in carbons from chemically activated wood, Carbon N. Y. 31 (1993) 1185–1192. https://doi.org/https://doi.org/10.1016/0008-6223(93)90071-H.

[81] S.M. Yakout, G. Sharaf El-Deen, Characterization of activated carbon prepared by phosphoric acid activation of olive stones, Arab. J. Chem. 9 (2016) S1155–S1162. https://doi.org/10.1016/j.arabjc.2011.12.002.

[82] M. Black, K.J. Bradford, Green Carbon Materials Advances and Applications, 1999.

[83] N. V. Sych, S.I. Trofymenko, O.I. Poddubnaya, M.M. Tsyba, V.I. Sapsay, D.O. Klymchuk, A.M. Puziy, Porous structure and surface chemistry of phosphoric acid activated carbon from corncob, Appl. Surf. Sci. 261 (2012) 75–82. https://doi.org/10.1016/j.apsusc.2012.07.084.

[84] M. Jagtoyen, J. Groppo, F. Derbyshire, Activated carbons from bituminous coals by reaction with H3PO4: The influence of coal cleaning, Fuel Process. Technol. 34 (1993) 85–96. https://doi.org/10.1016/0378-3820(93)90093-J.

[85] L.M. Moreno, S. Gorinstein, O.J. Medina, J. Palacios, · Efrén, J. Muñoz, Valorization of Garlic Crops Residues as Precursors of Cellulosic Materials, 11 (2020) 4767–4779. https://doi.org/10.1007/s12649-019-00799-3.

[86] N. Madani, N. Bouchenafa-Saib, O. Mohammedi, F.J. Varela-Gandía, D. Cazorla-Amorós, B. Hamada, O. Cherifi, Removal of heavy metal ions by adsorption onto activated carbon prepared from Stipa tenacissima leaves, Desalin. WATER Treat. 64 (2017) 179–188. https://doi.org/10.5004/dwt.2017.20254.

[87] Z. Chennouf-Abdellatif, B. Cheknane, F. Zermane, E.M. Gaigneaux, A.B.H. Sadok, O. Mohammedi, N. Bouchenafa-Saib, Preparation of activated carbon based on synthetic and agricultural wastes : application to the adsorption of methyl orange, Rev. Des Energies Renouvelables. 18 (2015) 575–586.

[88] I. Moulefera, M. Trabelsi, A. Mamun, L. Sabantina, polymers Electrospun Carbon Nanofibers from Biomass and Biomass Blends-Current Trends, Polymers (Basel). 13 (2021). https://doi.org/10.3390/polym13071071.

[89] N. Bouchenafa-Saïb, A. Mekarzia, B. Bouzid, O. Mohammedi, A. Khelifa, K. Benrachedi, N. Belhaneche, Removal of malathion from polluted water by adsorption onto chemically activated carbons produced from coffee grounds, Desalin. Water Treat. 52 (2014) 4920–4927. https://doi.org/10.1080/19443994.2013.808845.

[90] D. Montané, V. Torné-Fernández, V. Fierro, Activated carbons from lignin: Kinetic modeling of the pyrolysis of Kraft lignin activated with phosphoric acid, Chem. Eng. J. 106 (2005) 1–12. https://doi.org/10.1016/j.cej.2004.11.001.

[91] U.S. Energy Information Administration, April 2021 Monthly Energy Review, 2021. https://www.eia.gov/totalenergy/data/monthly/pdf/mer.pdf.

[92] A. Yousuf, F. Sannino, D. Pirozzi, Lignocellulosic biomass to liquid biofuels, Elsevier, 2019. https://doi.org/10.1016/C2017-0-03529-2.

[93] T.E. Rufford, J. Zhu, D. Hulicova-Jurcakova, Green carbon materials: advances and applications, Pan Stanford, 2019.

[94] R.J. Brooker, E.P. Widmaier, L.E. Graham, P.D. Stiling, Membrane structure and transport, Biol. McGraw-Hill, New York. (2008) 85–104.

[95] H. Qi, Nanocellulose-based functional materials, 2017. https://doi.org/10.1007/978-3-319-49592-7_5.

[96] D. Klemm, B. Heublein, H.P. Fink, A. Bohn, Cellulose: Fascinating biopolymer and sustainable raw material, Angew. Chemie - Int. Ed. 44 (2005) 3358–3393. https://doi.org/10.1002/anie.200460587.

[97] V.K. Gupta, S. Agarwal, P. Singh, D. Pathania, Acrylic acid grafted cellulosic Luffa cylindrical fiber for the removal of dye and metal ions, Carbohydr. Polym. 98 (2013) 1214–1221. https://doi.org/10.1016/j.carbpol.2013.07.019.

[98] H. Qi, Platforms for Functionalization of Cellulose, in: Nov. Funct. Mater. Based Cellul., Springer International Publishing, Cham, 2017: pp. 11–23. https://doi.org/10.1007/978-3-319-49592-7_2.

[99] Y. Habibi, L.A. Lucia, O.J. Rojas, CNC - Johnsy - habibi2010 [2].pdf, Chem. Rev. 110 (2010) 3479–3500.

[100] T. Heinze, T. Liebert, Celluloses and Polyoses/Hemicelluloses, Elsevier B.V., 2012. https://doi.org/10.1016/B978-0-444-53349-4.00255-7.

[101] J.-L. Wertz, M. Deleu, S. Coppée, A. Richel, Hemicelluloses and lignin in biorefineries, CRC Press, 2017.

[102] M. Asif, Sustainability of timber, wood and bamboo in construction, Woodhead Publishing Limited, 2009. https://doi.org/10.1533/9781845695842.31.

[103] S. Machmudah, Wahyudiono, H. Kanda, M. Goto, Hydrolysis of Biopolymers in Near-Critical and Subcritical Water, Elsevier Inc., 2017. https://doi.org/10.1016/B978-0-12-809380-1.00003-6.

[104] P. Bajpai, Wood and Fiber Fundamentals, 2018. https://doi.org/10.1016/b978-0-12-814240-0.00002-1.

[105] Forest Products: Biotechnology in Pulp and Paper Processing, (2009) 80–94. https://doi.org/10.1016/B978-012373944-5.00123-1.

[106] P.T. Martone, J.M. Estevez, F. Lu, K. Ruel, M.W. Denny, C. Somerville, J. Ralph, Discovery of Lignin in Seaweed Reveals Convergent Evolution of Cell-Wall Architecture, Curr. Biol. 19 (2009) 169–175. https://doi.org/10.1016/j.cub.2008.12.031.

[107] F.G. Calvo-Flores, Lignin: A Renewable Raw Material, Encycl. Renew. Sustain. Mater. (2020) 102–118. https://doi.org/10.1016/b978-0-12-803581-8.11517-6.

[108] E. Adler, Lignin chemistry—past, present and future, Wood Sci. Technol. 1977 113. 11 (1977) 169–218. https://doi.org/10.1007/BF00365615.

[109] D. Structures, S. Structures, Structure and Characteristics of Lignin, Lignin Chem. Appl. (2019) 25–50. https://doi.org/10.1016/b978-0-12-813941-7.00002-3.

[110] C. Tien, Front Matter, in: E. Inc (Ed.), Introd. to Adsorpt. Anal. Appl., Elsevier, 2019: pp. i–ii. https://doi.org/10.1016/B978-0-12-816446-4.09991-7.

[111] L. Hu, Y. Peng, F. Wu, S. Peng, J. Li, Z. Liu, Tubular activated carbons made from cotton stalk for dynamic adsorption of airborne toluene, J. Taiwan Inst. Chem. Eng. 80 (2017) 399–405. https://doi.org/https://doi.org/10.1016/j.jtice.2017.07.029.

[112] G. Henini, Y. Laidani, F. Souahi, S. Hanini, Study of Static Adsorption System Phenol / Luffa Cylindrica Fiber for Industrial Treatment of Wastewater, Energy Procedia. 18 (2012) 395–403. https://doi.org/http://dx.doi.org/10.1016/j.egypro.2012.05.051.

[113] M.H. Al-Malack, M. Dauda, Competitive adsorption of cadmium and phenol on activated carbon produced from municipal sludge, J. Environ. Chem. Eng. 5 (2017) 2718–2729. https://doi.org/10.1016/j.jece.2017.05.027.

[114] Y.C. Lee, M. Choi, J.W. Yang, H.J. Shin, Removal of malachite green (MG) from aqueous solutions by adsorption, precipitation, and alkaline fading using talc: kinetic, thermodynamic, and column feasibility studies, Desalin. Water Treat. 56 (2015) 1918–1928. https://doi.org/10.1080/19443994.2014.951970.

[115] R. Ahmad, S. Haseeb, Competitive adsorption of Cu2+ and Ni2+ on Luffa acutangula modified Tetraethoxysilane (LAP-TS) from the aqueous solution: Thermodynamic and isotherm studies, Groundw. Sustain. Dev. 1 (2015) 146–154. https://doi.org/https://doi.org/10.1016/j.gsd.2016.03.001.

[116] K. Koehlert, Activated carbon: Fundamentals and new applications, Chem. Eng. (United States). 124 (2017) 32–40.

[117] J. Wei, J. Yang, Z. Wen, J. Dai, Y. Li, B. Yao, Efficient photocatalytic oxidation of methane over β-Ga2O3/activated carbon composites, RSC Adv. 7 (2017) 37508–37521. https://doi.org/10.1039/c7ra05692c.

[118] A.W. Morawski, J. Kapica-Kozar, E. Kusiak-Nejman, A. Wanag, E. Kusiak-Nejman, J. Kapica-Kozar, A.W. Morawski, Photocatalytic performance of thermally prepared TiO2/C photocatalysts under artificial solar light, Micro Nano Lett. 11 (2016) 202–206. https://doi.org/10.1049/mnl.2015.0507.

[119] N. Bouazza, M. Ouzzine, M.A. Lillo-Ródenas, D. Eder, A. Linares-Solano, TiO2 nanotubes and CNT-TiO2 hybrid materials for the photocatalytic oxidation of propene at low concentration, Appl. Catal. B Environ. 92 (2009) 377–383. https://doi.org/10.1016/j.apcatb.2009.08.017.

[120] G. Li Puma, A. Bono, D. Krishnaiah, J.G. Collin, Preparation of titanium dioxide photocatalyst loaded onto activated carbon support using chemical vapor deposition: A review paper, J. Hazard. Mater. 157 (2008) 209–219. https://doi.org/https://doi.org/10.1016/j.jhazmat.2008.01.040.

[121] T. Y. J. Han, M.A. Worsley, T. F. Baumann, Joe H. Satcher Jr., T. Yong-Jin Han, M.A. Worsley, T.F. Baumann, J.H. Satcher, Synthesis of ZnO coated activated carbon aerogel by simple sol-gel route, 2011. https://doi.org/10.1039/C0JM03204B.

[122] C. Belver, J. Bedia, A. Gómez-Avilés, M. Peñas-Garzón, J.J. Rodriguez, Chapter 22 - Semiconductor Photocatalysis for Water Purification, in: S. Thomas, D. Pasquini, S.-Y. Leu, D.A. Gopakumar (Eds.), Nanoscale Mater. Water Purif., Elsevier, 2019: pp. 581–651. https://doi.org/https://doi.org/10.1016/B978-0-12-813926-4.00028-8.

[123] S. Sai Tubtim, Heterogeneous Photocatalysis Using Inorganic Semiconductor Solids, 2554. http://library1.nida.ac.th/termpaper6/sd/2554/19755.pdf.

[124] E. Raymundo-Piñero, D. Cazorla-Amorós, C. Salinas-Martinez De Lecea, A. Linares-Solano, Factors controling the SO2 removal by porous carbons: relevance of the SO2 oxidation step, Carbon N. Y. 38 (2000) 335–344. https://doi.org/10.1016/S0008-6223(99)00109-8.

[125] A. Morawski, M. Janus, B. Tryba, M. Toyoda, T. Tsumura, M. Inagaki, Carbon modified TiO2 photocatalysts for water purification, 11 (2009) 46. https://doi.org/https://doi.org/10.2478/v10026-009-0023-0.

[126] Y. Li, X. Li, J. Li, J. Yin, TiO2-coated active carbon composites with increased photocatalytic activity prepared by a properly controlled sol-gel method, Mater. Lett. 59 (2005) 2659–2663. https://doi.org/10.1016/j.matlet.2005.03.050.

[127] S. Lee, C.Y. Yun, M.S. Hahn, J. Lee, J. Yi, Synthesis and characterization of carbon-doped titania as a visible-light-sensitive photocatalyst, Korean J. Chem. Eng. 25 (2008) 892–896. https://doi.org/10.1007/s11814-008-0147-6.

[128] P. Fu, Y. Luan, X. Dai, Preparation of TiO2 photocatalyst anchored on activated carbon fibers and its photodegradation of methylene blue, China Particuology. 2 (2004) 76–80. https://doi.org/https://doi.org/10.1016/S1672-2515(07)60027-X.

[129] T.J. Bandosz, Surface Chemistry of Carbon Materials, in: Carbon Mater. Catal., John Wiley & Sons, Ltd, 2008: pp. 45–92. https://doi.org/https://doi.org/10.1002/9780470403709.ch2.

[130] N. Bouchenafa-Saïb, P. Grange, P. Verhasselt, F. Addoun, V. Dubois, Effect of oxidant treatment of date pit active carbons used as Pd supports in catalytic hydrogenation of nitrobenzene, Appl. Catal. A Gen. 286 (2005) 167–174. https://doi.org/10.1016/j.apcata.2005.02.022.

[131] Š. Paušová, M. Riva, M. Baudys, J. Krýsa, Z. Barbieriková, V. Brezová, Composite materials based on active carbon/TiO2 for photocatalytic water purification, Catal. Today. 328 (2019) 178–182. https://doi.org/https://doi.org/10.1016/j.cattod.2019.01.010.

[132] K. Woan, G. Pyrgiotakis, W. Sigmund, Photocatalytic carbon-nanotube-Ti02 composites, Adv. Mater. 21 (2009) 2233–2239. https://doi.org/10.1002/adma.200802738.

[133] F. Rodŕíguez-Reinoso, A. Seṕulveda-Escribano, Carbon as Catalyst Support, in: Carbon Mater. Catal., John Wiley & Sons, Ltd, 2008: pp. 131–155. https://doi.org/https://doi.org/10.1002/9780470403709.ch4.

[134] A. Frassoldati, E. Ranzi, Modeling of Thermochemical Conversion of Biomasses, Ref. Modul. Chem. Mol. Sci. Chem. Eng. (2019) 1–10. https://doi.org/10.1016/b978-0-12-409547-2.11625-7.

[135] I. O., E. O., T.O. K. Audu, Application of Luffa Cylindrica in Natural form as Biosorbent to Removal of Divalent Metals from Aqueous Solutions - Kinetic and

Equilibrium Study, Waste Water - Treat. Reutil. 546 (2011). https://doi.org/10.5772/16150.

[136] Y. Laidani, S. Hanini, G. Henini, Study Contribution of the Phenol Adsorption Dynamics of the System Fiber Luffa Cylindrical, Energy Procedia. 18 (2012) 384–394. https://doi.org/http://dx.doi.org/10.1016/j.egypro.2012.05.050.

[137] A. Modi, V. Kumar, Luffa echinata Roxb.-A review on its ethanomedicinal, phytochemical and pharmacological perspective, Asian Pacific J. Trop. Dis. 4 (2014) S7–S12. https://doi.org/10.1016/S2222-1808(14)60409-6.

[138] A.S. Abitogun, A.O. Ashogbon, R.G. Polytechnic, O. State, Nutritional assessment and chemical composition of raw and defatted Luffa cylindrica seed flour, Ethnobot. Leafl. 14 (2010) 225–235. internal-pdf://91.148.80.1/Nutritional Assessment and Chemical Composition of Raw and ...Abitogun and Ashogbon, 2010 (2).pdf.

[139] F.A.S. Dairo, P.A. Aye, T.A. Oluwasola, Some functional properties of loofah gourd (Luffa cylindrica L., M. J. Roem) seed, J. Food, Agric. Environ. 5 (2007) 97–101.

[140] I.O. Mazali, O. Alves, Morphosynthesis: high fidelity inorganic replica of the fibrous network of loofa sponge (Luffa cylindrica), An. Acad. Bras. Cienc. 77 (2005) 25–31. https://doi.org/10.1590/S0001-37652005000100003.

[141] Achigan-Dako, E.G. & N'danikou, S. & Vodouhê, R.S., Luffa cylindrica (L.) M.Roem, Internet] Rec. from PROTA4U. Brink, M. Achigan-Dako, E.G. (Editors). PROTA (Plant Resour. Trop. Africa / Ressources Végétales l'Afrique Trop. Wageningen, Netherlands. (2011).

[142] A. Altınışık, E. Gür, Y. Seki, A natural sorbent, Luffa cylindrica for the removal of a model basic dye, J. Hazard. Mater. 179 (2010) 658–664.

[143] A. Zampieri, G.T.P. Mabande, T. Selvam, W. Schwieger, A. Rudolph, R. Hermann, H. Sieber, P. Greil, Biotemplating of Luffa cylindrica sponges to self-supporting hierarchical zeolite macrostructures for bio-inspired structured catalytic reactors, Mater. Sci. Eng. C. 26 (2006) 130–135. https://doi.org/http://dx.doi.org/10.1016/j.msec.2005.08.036.

[144] Gilberto Siqueira, Julien Bras, A. Dufresne., Luffa cylindrica as alignocellulosic source of fiber, microfibrillated cellulose, and cellulose nanocrystals, Bioresources.Com. V 5 (2010) 727–740.

[145] S. Manikandaselvi, V. Vadivel, P. Brindha, Review on Luffa acutangula L.: Ethnobotany, phytochemistry, nutritional value and pharmacological properties, Int. J. Curr. Pharm. Rev. Res. 7 (2016) 151–155.

[146] K. R, \& Basu, B. D, Indian Medicinal Plants. 8 Vols., International Book Distributors, 1935. https://books.google.dz/books?id=vrxLAAAACAAJ.

[147] S. Jayalakshmi, A. Patra, A.K. Wahi, Cytomorphological Studies on Stem of Luffa echinata Roxb, J. Young Pharm. 2 (2010) 252–254.

https://doi.org/10.4103/0975-1483.66800.

[148] Y. Laidani, S. Hanini, G. Henini, “Valorisation de la Luffa Cylindrica pour les traitements des eaux chargées en cuivre. Etude de la possibilité de sa régeneration par desorption chimique” . , in: Vème Congrès Int. Sur Les Energies Renouvelables l’Environnement, Tunisie, n.d.: pp. 1–8.

[149] Jack Arnott;, Luffa sponge gourd, Univ. Georg. Ft. Val. State Univ. U.S. Dep. Agric. Cties. State Coop. (n.d.).

[150] S. Partap, A. Kumar, N.K. Sharma, K.K. Jha, Luffa Cylindrica: An important medicinal plant, J. Nat. Prod. Plant Resourse. V.2 (2012) 127–134. http://scholarsresearchlibrary.com/archive.html.

[151] A.A. M, K. S, F. M, A. Hemaid, Molecular Phylogenetic Study of Luffa Tuberosa Roxb. (Cucurbitaceae) Based on Internal Transcribed Spacer (Its) Sequences of Nuclear Ribosomal Dna and Its Systematic Implication, Int. J. Bioinforma. Res. 2 (2010) 42–60. https://doi.org/10.9735/0975-3087.2.2.42-60.

[152] O. Innocent, E. Oboh O., O.K.A. Thomas, Application of Luffa Cylindrica in Natural forme as Biosorbent to Removal Divalent Metals from Aqueous Solutions Kinetic and Equilibrium Study, Waste Water-Treatment and Reutilization, InTech. (2011) 196–212.

[153] A. Adewuyi, F.V. Pereira, Underutilized Luffa cylindrica sponge: A local bio-adsorbent for the removal of Pb(II) pollutant from water system, Beni-Suef Univ. J. Basic Appl. Sci. 6 (2017) 118–126. https://doi.org/https://doi.org/10.1016/j.bjbas.2017.02.001.

[154] M.A. Mazmanci, A. Ünyayar, Decolourisation of Reactive Black 5 by Funalia trogii immobilised on Luffa cylindrica sponge, Process Biochem. 40 (2005) 337–342. https://doi.org/http://dx.doi.org/10.1016/j.procbio.2004.01.007.

[155] Y. Tong, S. Zhao, J. Ma, L. Wang, Y. Zhang, Y. Gao, Y.M. Xie, Improving cracking and drying shrinkage properties of cement mortar by adding chemically treated luffa fibres, Constr. Build. Mater. 71 (2014) 327–333. https://doi.org/http://dx.doi.org/10.1016/j.conbuildmat.2014.08.077.

[156] G. Siqueira, J. Bras, N. Follain, S. Belbekhouche, S. Marais, A. Dufresne, Thermal and mechanical properties of bio-nanocomposites reinforced by Luffa cylindrica cellulose nanocrystals, Carbohydr. Polym. 91 (2013) 711–717. https://doi.org/http://dx.doi.org/10.1016/j.carbpol.2012.08.057.

[157] M. Sakthivel, S. Vijayakumar, S. Ramesh, Production and Characterization of Luffa/Coir Reinforced Polypropylene Composite, Procedia Mater. Sci. V.5 (2014) 739–745. https://doi.org/http://dx.doi.org/10.1016/j.mspro.2014.07.323.

[158] T.R. Annunciado, T.H.D. Sydenstricker, S.C. Amico, Experimental investigation of various vegetable fibers as sorbent materials for oil spills, Mar. Pollut. Bull. 50 (2005) 1340–1346. https://doi.org/http://dx.doi.org/10.1016/j.marpolbul.2005.04.043.

[159] J. Zhang, B. Tian, L. Wang, M. Xing, J. Lei, Photocatalysis (Vol. 100), 2018. http://www.springer.com/series/632.

[160] Photocatalysis, IUPAC Compend. Chem. Terminol. 293 (2008) 4580. https://doi.org/10.1351/goldbook.p04580.

[161] W. Cao, Semiconductor Photocatalysis Materials, Mechanisms and Applications, ExLi4EvA, 2016. http://library1.nida.ac.th/termpaper6/sd/2554/19755.pdf.

[162] J.-M. Herrmann, Heterogeneous photocatalysis: fundamentals and applications to the removal of various types of aqueous pollutants, Catal. Today. 53 (1999) 115–129. https://doi.org/https://doi.org/10.1016/S0920-5861(99)00107-8.

[163] S.G. Kumar, L.G. Devi, Review on Modified TiO 2 Photocatalysis under UV/Visible Light: Selected Results and Related Mechanisms on Interfacial Charge Carrier Transfer Dynamics, J. Phys. Chem. A. 115 (n.d.) 13211–13241. https://www.academia.edu/9418976/Review_on_Modified_TiO2_Photocatalysis_under_UV_Visible_Light_Selected_Results_and_Related_Mechanisms_on_Interfacial_Charge_Carrier_Transfer_Dynamics (accessed June 29, 2021).

[164] C. Raviola, S. Protti, Recent Advances on Photocatalysis for Water Detoxification and CO2 Reduction, in: Visible Light. Photocatal., John Wiley & Sons, Ltd, 2018: pp. 27–51. https://doi.org/https://doi.org/10.1002/9783527808175.ch2.

[165] R.A.S.C. Ameta, PHOTOCATALYSIS Principles and Applications, Taylor & Francis Group, LLC, 2017. http://library1.nida.ac.th/termpaper6/sd/2554/19755.pdf.

[166] J.A. Byrne, P.S.M. Dunlop, J.W.J. Hamilton, P. Fernández-Ibáñez, I. Polo-López, P.K. Sharma, A.S.M. Vennard, A review of heterogeneous photocatalysis for water and surface disinfection, Molecules. 20 (2015) 5574–5615. https://doi.org/10.3390/molecules20045574.

[167] R. Pawar, C.S. Lee, Heterogeneous Nanocomposite-Photocatalysis for Water Purification, William Andrew, Bighamton, UNITED STATES, 2015. http://ebookcentral.proquest.com/lib/bibliotecauma-ebooks/detail.action?docID=2033831.

[168] S. Ahmed, M.G. Rasul, W.N. Martens, R. Brown, M.A. Hashib, Advances in heterogeneous photocatalytic degradation of phenols and dyes in wastewater: A review, Water. Air. Soil Pollut. 215 (2011) 3–29. https://doi.org/10.1007/s11270-010-0456-3.

[169] S. Zhu, D. Wang, Photocatalysis: Basic principles, diverse forms of implementations and emerging scientific opportunities, Adv. Energy Mater. 7 (2017) 1–24. https://doi.org/10.1002/aenm.201700841.

[170] J.S.G. Neto, S. Satyro, E.M. Saggioro, M. Dezotti, Investigation of mechanism and kinetics in the TiO2 photocatalytic degradation of Indigo Carmine dye using radical scavengers, Int. J. Environ. Sci. Technol. 18 (2020) 163–172. https://doi.org/10.1007/s13762-020-02842-6.

[171] U.I. Gaya, Principles of Heterogeneous Photocatalysis, in: Heterog. Photocatal. Using Inorg. Semicond. Solids, Springer Netherlands, Dordrecht, 2014: pp. 1–41. https://doi.org/10.1007/978-94-007-7775-0_1.

[172] J. Zhang, B. Tian, L. Wang, M. Xing, J. Lei, Mechanism of Photocatalysis, in: Photocatal. Fundam. Mater. Appl., Springer Singapore, Singapore, 2018: pp. 1–15. https://doi.org/10.1007/978-981-13-2113-9_1.

[173] B. Bajorowicz, M.P. Kobylański, A. Malankowska, P. Mazierski, J. Nadolna, A. Pieczyńska, A. Zaleska-Medynska, Application of metal oxide-based photocatalysis, 2018. https://doi.org/10.1016/B978-0-12-811634-0.00004-4.

[174] Q. Guo, C.Y. Zhou, Z.B. Ma, Z.F. Ren, H.J. Fan, X.M. Yang, Fundamental processes in surface photocatalysis on TiO2, 2016. https://doi.org/10.3866/PKU.WHXB201512081.

[175] D. Spasiano, R. Marotta, S. Malato, P. Fernandez-Ibañez, I. Di Somma, Solar photocatalysis: Materials, reactors, some commercial, and pre-industrialized applications. A comprehensive approach, Appl. Catal. B Environ. 170–171 (2015) 90–123. https://doi.org/10.1016/j.apcatb.2014.12.050.

[176] R. Prabhu, L.A. Lawton, UV LED Sources for Heterogeneous Photocatalysis Metadata of the chapter that will be visualized online, (2014). https://doi.org/10.1007/698.

[177] J. Schneider, M. Matsuoka, M. Takeuchi, J. Zhang, Y. Horiuchi, M. Anpo, D.W. Bahnemann, Understanding TiO2photocatalysis: Mechanisms and materials, Chem. Rev. 114 (2014) 9919–9986. https://doi.org/10.1021/cr5001892.

[178] S. Chakrabarti, Solar Photocatalysis for Environmental Remediation, 2017. https://doi.org/10.1201/9780429058363.

[179] R. Ameta, S.C. Ameta, Photocatalysis: Principles and Applications, Focus Catal. 2016 (2016) 7. https://doi.org/10.1016/j.focat.2016.10.050.

[180] A. Amorós-Pérez, L. Cano-Casanova, A. Castillo-Deltell, M.Á. Lillo-Ródenas, M. del C. Román-Martínez, M.C. Román-Martínez, TiO2 Modification with Transition Metallic Species (Cr, Co, Ni, and Cu) for Photocatalytic Abatement of Acetic Acid in Liquid Phase and Propene in Gas Phase, Materials (Basel). 12 (2018) 40. https://doi.org/10.3390/ma12010040.

[181] J. Ma, C. Wang, H. He, Enhanced photocatalytic oxidation of NO over g-C3N4-TiO2 under UV and visible light, Appl. Catal. B Environ. 184 (2016) 28–34. https://doi.org/10.1016/j.apcatb.2015.11.013.

[182] Y. Kakuma, A.Y. Nosaka, Y. Nosaka, Difference in TiO2 photocatalytic mechanism between rutile and anatase studied by the detection of active oxygen and surface species in water, Phys. Chem. Chem. Phys. 17 (2015) 18691–18698. https://doi.org/10.1039/c5cp02004b.

[183] H. Slimen, A. Houas, J.P. Nogier, Elaboration of stable anatase TiO2 through activated carbon addition with high photocatalytic activity under visible light, J.

Photochem. Photobiol. A Chem. 221 (2011) 13–21. https://doi.org/10.1016/j.jphotochem.2011.04.013.

[184] J. Matos, R. Montaña, E. Rivero, A. Escudero, D. Uzcategui, Influence of anatase and rutile phase in TiO2 upon the photocatalytic degradation of methylene blue under solar irradiation in presence of activated carbon, Water Sci. Technol. 69 (2014) 2184–2190. https://doi.org/http://dx.doi.org/10.2166/wst.2014.127.

[185] R. Vasant Kumar, M. Coto, Visible-Light-Active Photocatalysis: Nanostructured Catalyst Design, Mechanisms, and Applications, in: Visible Light. Photocatal., John Wiley & Sons, Ltd, 2018: pp. 499–526. https://doi.org/https://doi.org/10.1002/9783527808175.ch18.

[186] A.Y. Ahmed, T.A. Kandiel, I. Ivanova, D. Bahnemann, Photocatalytic and photoelectrochemical oxidation mechanisms ofmethanol on TiO 2 in aqueous solution, Appl. Surf. Sci. 319 (2014) 44–49. https://doi.org/10.1016/j.apsusc.2014.07.134.

[187] A. Imanishi, K. Fukui, Atomic-Scale Surface Local Structure of TiO 2 and Its Influence on the Water Photooxidation Process, J. Phys. Chem. Lett. 5 (2014) 2108–2117. https://doi.org/10.1021/jz5004704.

[188] B. Srikanth, R. Goutham, R. Badri Narayan, A. Ramprasath, K.P. Gopinath, A.R. Sankaranarayanan, Recent advancements in supporting materials for immobilised photocatalytic applications in waste water treatment, J. Environ. Manage. 200 (2017) 60–78. https://doi.org/10.1016/j.jenvman.2017.05.063.

[189] A. Amorós-Pérez, L. Cano-Casanova, M.Á. Lillo-Ródenas, M.C. Román-Martínez, Cu/TiO2 photocatalysts for the conversion of acetic acid into biogas and hydrogen, Catal. Today. 287 (2017) 78–84. https://doi.org/10.1016/j.cattod.2016.09.009.

[190] J. Carlos Durán-Valle, Techniques Employed in the Physicochemical Characterization of Activated Carbons, in: G. Bajac (Ed.), Lignocellul. Precursors Used Synth. Act. Carbon - Charact. Tech. Appl. Wastewater Treat., Janeza Trdine 9, 51000 Rijeka, Croatia, 2012. https://doi.org/10.5772/39366.

[191] R.A. Díaz, Thermal Analysis: Fundamentals and Applications to Material Characterization: Proceedings of the International Seminar: Thermal Analysis and Rheology: Ferrol, Spain, 30 Juny-4 July 2003, Universidade da Coruña, Servizo de Publicacións, 2005.

[192] A.J. Romero-Anaya, M.A. Lillo-Ródenas, C. Salinas-Martínez de Lecea, A. Linares-Solano, Hydrothermal and conventional H3PO4 activation of two natural bio-fibers, Carbon N. Y. 50 (2012) 3158–3169. https://doi.org/https://doi.org/10.1016/j.carbon.2011.10.031.

[193] J.I. Goldstein, D.E. Newbury, J.R. Michael, N.W.M. Ritchie, J.H.J. Scott, D.C. Joy, Quantitative Analysis: From k-ratio to Composition, in: J.I. Goldstein, D.E. Newbury, J.R. Michael, N.W.M. Ritchie, J.H.J. Scott, D.C. Joy (Eds.), Scanning Electron Microsc. X-Ray Microanal., Springer New York, New York, NY, 2018: pp. 289–307. https://doi.org/10.1007/978-1-4939-6676-9_19.

[194] J.I. Goldstein, D.E. Newbury, J.R. Michael, N.W.M. Ritchie, J.H.J. Scott, D.C. Joy, Scanning electron microscopy and X-ray microanalysis, Springer, 2017.

[195] K. Akhtar, S.A. Khan, S.B. Khan, A.M. Asiri, Scanning Electron Microscopy: Principle and Applications in Nanomaterials Characterization BT - Handbook of Materials Characterization, in: S.K. Sharma (Ed.), Springer International Publishing, Cham, 2018: pp. 113–145. https://doi.org/10.1007/978-3-319-92955-2_4.

[196] J.B. Condon, Surface Area and Porosity Determinations by Physisorption: Measurement, Classical Theories and Quantum Theory', Elsevier, 2006.

[197] K.S.W. Sing, Reporting physisorption data for gas/solid systems, Pure Appl. Chem. 54 (1982) 2201–2218. https://doi.org/10.1351/pac198254112201.

[198] C. Nguyen, D.D. Do, The Dubinin–Radushkevich equation and the underlying microscopic adsorption description, Carbon N. Y. 39 (2001) 1327–1336. https://doi.org/https://doi.org/10.1016/S0008-6223(00)00265-7.

[199] M. Polanyi, Section III.—Theories of the adsorption of gases. A general survey and some additional remarks. Introductory paper to section III, Trans. Faraday Soc. 28 (1932) 316–333. https://doi.org/10.1039/TF9322800316.

[200] P. Klobes, R.G. Munro, Porosity and specific surface area measurements for solid materials, (2006).

[201] Mm. Dubinin, The potential theory of adsorption of gases and vapors for adsorbents with energetically nonuniform surfaces, Chem. Rev. 60 (1960) 235–241.

[202] J. Jagiello, J.P. Olivier, 2D-NLDFT adsorption models for carbon slit-shaped pores with surface energetical heterogeneity and geometrical corrugation, Carbon N. Y. 55 (2013) 70–80. https://doi.org/10.1016/j.carbon.2012.12.011.

[203] B.D. Cullity, Elements of X-ray Diffraction, Addison-Wesley Publishing, 1956.

[204] C. Suryanarayana, M.G. Norton, X-ray diffraction: a practical approach, Springer Science & Business Media, 2013.

[205] M. Lee, F. Fundamentals, X-Ray Diffraction for Materials Research: From Fundamentals to Applications Myeongkyu Lee, CRC Press, 2017. https://doi.org/10.1557/mrs.2017.22.

[206] H. Jensen, K.D. Joensen, J.E. Jørgensen, J.S. Pedersen, E.G. Søgaard, Characterization of nanosized partly crystalline photocatalysts, J. Nanoparticle Res. 6 (2004) 519–526. https://doi.org/10.1007/s11051-004-1714-3.

[207] J. Torrent, V. Barrón, Diffuse Reflectance Spectroscopy, in: Methods Soil Anal. Part 5—Mineralogical Methods, 2008: pp. 367–385. https://doi.org/https://doi.org/10.2136/sssabookser5.5.c13.

[208] S.K. Sharma, D.S. Verma, L.U. Khan, S. Kumar, S.B. Khan, Handbook of

Materials Characterization, Handb. Mater. Charact. (2018) 1–613. https://doi.org/10.1007/978-3-319-92955-2.

[209] J.F. Watts, J. Wolstenholme, An introduction to surface analysis by XPS and AES, (2003).

[210] J.F. Moulder, W.F. Stickle, P.E. Sobol, K.D. Bomben, Handbook of X-ray photoelectron spectroscopy: a reference book of standard spectra for identification and interpretation of XPS data; Physical Electronics: Eden Prairie, MN, 1995, There Is No Corresp. Rec. This Ref. Sch. (2000).

[211] J.F. James, A Student's Guide to Fourier Transforms: With Applications in Physics and Engineering, A Student's Guid. to Fourier Transform. With Appl. Phys. Eng. Third Ed. 9780521176835 (2011) 1–146. https://doi.org/10.1017/CBO9780511762307.

[212] A. Mills, C. Hill, P.K.J.J. Robertson, Overview of the current ISO tests for photocatalytic materials, J. Photochem. Photobiol. A Chem. 237 (2012) 7–23. https://doi.org/https://doi.org/10.1016/j.jphotochem.2012.02.024.

[213] G. Zaccariello, E. Moretti, L. Storaro, P. Riello, P. Canton, V. Gombac, T. Montini, E. Rodrguez-Castelln, A. Benedetti, TiO 2 mesoporous silica nanocomposites: cooperative effect in the photocatalytic degradation of dyes and drugs, RSC Adv. 4 (2014) 37826–37837. https://doi.org/10.1039/c4ra06767c.

[214] J.K. Ratan, M. Kaur, B. Adiraju, Synthesis of activated carbon from agricultural waste using a simple method: Characterization, parametric and isotherms study, Mater. Today Proc. 5 (2018) 3334–3345. https://doi.org/10.1016/j.matpr.2017.11.576.

[215] A. Kumar, H.M. Jena, High surface area microporous activated carbons prepared from Fox nut (Euryale ferox) shell by zinc chloride activation, Appl. Surf. Sci. 356 (2015) 753–761. https://doi.org/10.1016/J.APSUSC.2015.08.074.

[216] S.N. Guilhen, O. Mašek, N. Ortiz, J.C. Izidoro, D.A. Fungaro, Pyrolytic temperature evaluation of macauba biochar for uranium adsorption from aqueous solutions, Biomass and Bioenergy. 122 (2019) 381–390. https://doi.org/10.1016/j.biombioe.2019.01.008.

[217] W.T. Tsai, S.C. Liu, H.R. Chen, Y.M. Chang, Y.L. Tsai, Textural and chemical properties of swine-manure-derived biochar pertinent to its potential use as a soil amendment, Chemosphere. 89 (2012) 198–203. https://doi.org/10.1016/J.CHEMOSPHERE.2012.05.085.

[218] P. González-García, Activated carbon from lignocellulosics precursors: A review of the synthesis methods, characterization techniques and applications, Renew. Sustain. Energy Rev. 82 (2018) 1393–1414. https://doi.org/https://doi.org/10.1016/j.rser.2017.04.117.

[219] H. Yang, R. Yan, H. Chen, D.H. Lee, C. Zheng, Characteristics of hemicellulose, cellulose and lignin pyrolysis, Fuel. 86 (2007) 1781–1788. https://doi.org/https://doi.org/10.1016/j.fuel.2006.12.013.

[220] T.Y. Jun, S.D. Arumugam, N.H.A. Latip, A.M. Abdullah, P.A. Latif, Effect of activation temperature and heating duration on physical characteristics of activated carbon prepared from agriculture waste, EnvironmentAsia. 3 (2010) 143–148.

[221] S.-S.S. Xu, S.-W.W. Qiu, Z.-Y.Y. Yuan, T.-Z.Z. Ren, T.J. Bandosz, Nitrogen-containing activated carbon of improved electrochemical performance derived from cotton stalks using indirect chemical activation, J. Colloid Interface Sci. 540 (2019) 285–294. https://doi.org/https://doi.org/10.1016/j.jcis.2019.01.031.

[222] I. Moulefera, F.J. García-Mateos, A. Benyoucef, J.M. Rosas, J. Rodríguez-Mirasol, T. Cordero, Effect of Co-solution of Carbon Precursor and Activating Agent on the Textural Properties of Highly Porous Activated Carbon Obtained by Chemical Activation of Lignin With H3PO4, Front. Mater. 7 (2020) 1–14. https://doi.org/10.3389/fmats.2020.00153.

[223] J. Palomo, J.J. Ternero-Hidalgo, J.M. Rosas, J. Rodríguez-Mirasol, T. Cordero, Selective nitrogen functionalization of phosphorus-containing activated carbons, Fuel Process. Technol. 156 (2017) 438–445. https://doi.org/10.1016/j.fuproc.2016.10.006.

[224] K.A. Cychosz, M. Thommes, Progress in the Physisorption Characterization of Nanoporous Gas Storage Materials, Engineering. 4 (2018) 559–566. https://doi.org/10.1016/J.ENG.2018.06.001.

[225] M. Jagtoyen, F. Derbyshire, Activated carbons from yellow poplar and white oak by H3PO4 activation, Carbon N. Y. 36 (1998) 1085–1097. https://doi.org/10.1016/S0008-6223(98)00082-7.

[226] Y. Sun, G. Yang, J. Zhang, Y. Wang, M. Yao, Activated carbon preparation from lignin by H 3PO 4 activation and its application to gas separation, Chem. Eng. Technol. 35 (2012) 309–316. https://doi.org/10.1002/ceat.201100309.

[227] S.M. Yakout, G. Sharaf El-Deen, Characterization of activated carbon prepared by phosphoric acid activation of olive stones, Arab. J. Chem. 9 (2016) S1155–S1162. https://doi.org/10.1016/j.arabjc.2011.12.002.

[228] M.J. Valero-Romero, E.M. Calvo-Muñoz, R. Ruiz-Rosas, J. Rodríguez-Mirasol, T. Cordero, Phosphorus-Containing Mesoporous Carbon Acid Catalyst for Methanol Dehydration to Dimethyl Ether, Ind. Eng. Chem. Res. 58 (2019) 4042–4053. https://doi.org/10.1021/acs.iecr.8b05897.

[229] M.A. Nahil, P.T. Williams, Pore characteristics of activated carbons from the phosphoric acid chemical activation of cotton stalks, Biomass and Bioenergy. 37 (2012) 142–149. https://doi.org/10.1016/j.biombioe.2011.12.019.

[230] I. O., E. O., T.O. K. Audu, Application of Luffa Cylindrica in Natural form as Biosorbent to Removal of Divalent Metals from Aqueous Solutions - Kinetic and Equilibrium Study, Waste Water - Treat. Reutil. (2011). https://doi.org/10.5772/16150.

[231] M. Asiltürk, Ş. Şener, TiO 2-activated carbon photocatalysts: Preparation,

characterization and photocatalytic activities, Chem. Eng. J. 180 (2012) 354–363. https://doi.org/10.1016/j.cej.2011.11.045.

[232] T. Lopez, J.L. Cuevas, L. Ilharco, P. Ramírez, F. Rodríguez-Reinoso, E. Rodríguez-Castellón, XPS characterization and E. Coli DNA degradation using functionalized Cu/TiO2 nanobiocatalysts, Mol. Catal. 449 (2018) 62–71. https://doi.org/10.1016/j.mcat.2018.02.010.

[233] F.J. García-Mateos, R. Berenguer, M.J. Valero-Romero, J. Rodríguez-Mirasol, T. Cordero, Phosphorus functionalization for the rapid preparation of highly nanoporous submicron-diameter carbon fibers by electrospinning of lignin solutions, J. Mater. Chem. A. 6 (2018) 1219–1233. https://doi.org/10.1039/C7TA08788H.

[234] C. Hou, B. Hu, J. Zhu, Photocatalytic degradation of methylene blue over TiO2 pretreated with varying concentrations of NaOH, Catalysts. 8 (2018). https://doi.org/10.3390/catal8120575.

[235] P. Larkin, Infrared and Raman spectroscopy: principles and spectral interpretation, Elsevier, 2017.

[236] L.-L. Qu, N. Wang, Y.-Y. Li, D.-D. Bao, G.-H. Yang, H.-T. Li, Novel titanium dioxide–graphene–activated carbon ternary nanocomposites with enhanced photocatalytic performance in rhodamine B and tetracycline hydrochloride degradation, J. Mater. Sci. 2017 5213. 52 (2017) 8311–8320. https://doi.org/10.1007/S10853-017-1047-0.

[237] B. Xing, C. Shi, C. Zhang, G. Yi, L. Chen, H. Guo, G. Huang, J. Cao, Preparation of TiO2/Activated Carbon Composites for Photocatalytic Degradation of RhB under UV Light Irradiation, J. Nanomater. 2016 (2016). https://doi.org/10.1155/2016/8393648.

[238] Z.A. Ramli, N. Asim, W.N. Isahak, Z. Emdadi, N. Ahmad-Ludin, M.A. Yarmo, K. Sopian, Photocatalytic degradation of methylene blue under UV light irradiation on prepared carbonaceous TiO2, ScientificWorldJournal. 2014 (2014) 415136. https://doi.org/10.1155/2014/415136.

[239] A.H. Mamaghani, F. Haghighat, C.S. Lee, Effect of titanium dioxide properties and support material on photocatalytic oxidation of indoor air pollutants, Build. Environ. 189 (2021) 107518. https://doi.org/10.1016/j.buildenv.2020.107518.

[240] S. J, M. M, T. M, Z. J, H. Y, A. M, B. DW, Understanding TiO2 photocatalysis: mechanisms and materials, Chem. Rev. 114 (2014) 9919–9986. https://doi.org/10.1021/CR5001892.

[241] P. Nitnithiphrut, M. Thabuot, V. Seithtanabutara, Fabrication of Composite Supercapacitor Containing Para Wood-derived Activated Carbon and TiO2, Energy Procedia. 138 (2017) 116–121. https://doi.org/10.1016/j.egypro.2017.10.074.

[242] H. Jensen, A. Soloviev, Z. Li, E.G. Søgaard, XPS and FTIR investigation of the surface properties of different prepared titania nano-powders, Appl. Surf. Sci.

246 239–249.

[243] B. Ohtani, O.O. Prieto-Mahaney, D. Li, R. Abe, What is Degussa (Evonik) P25? Crystalline composition analysis, reconstruction from isolated pure particles and photocatalytic activity test, J. Photochem. Photobiol. A Chem. 216 (2010) 179–182. https://doi.org/10.1016/j.jphotochem.2010.07.024.

[244] Y. Tian, P. Liu, X. Wang, H. Lin, Adsorption of malachite green from aqueous solutions onto ordered mesoporous carbons, Chem. Eng. J. 171 (2011) 1263–1269. https://doi.org/10.1016/j.cej.2011.05.040.

[245] X. Cheng, L. Zu, Y. Jiang, D. Shi, X. Cai, Y. Ni, S. Lin, Y. Qin, A titanium-based photo-Fenton bifunctional catalyst of mp-MXene/TiO2-x nanodots for dramatic enhancement of catalytic efficiency in advanced oxidation processes, Chem. Commun. 54 (2018) 11622–11625. https://doi.org/10.1039/c8cc05866k.

[246] T.M. El-Morsi, W.R. Budakowski, A.S. Abd-El-Aziz, K.J. Friesen, Photocatalytic degradation of 1,10-dichlorodecane in aqueous suspensions of TiO2: A reaction of adsorbed chlorinated alkane with surface hydroxyl radicals, Environ. Sci. Technol. 34 (2000) 1018–1022. https://doi.org/10.1021/es9907360.

[247] T. Tan, D. Beydoun, R. Amal, Effects of organic hole scavengers on the photocatalytic reduction of selenium anions, J. Photochem. Photobiol. A Chem. 159 (2003) 273–280. https://doi.org/10.1016/S1010-6030(03)00171-0.